WROCŁAW UNIVERSITY OF SCIENCE AND TECHNOLOGY

DOCTORAL THESIS

Heterogeneous integration of InAs/InP quantum dots with photonic integrated circuits operating at 1550 nm

Author:
Marek MIKULICZ

Supervisors:
Assoc. Prof. Marcin Syperek,
Dr. Paweł Mrowiński

Wrocław
University
of Science
and Technology

Wrocław, 2025

Abstract

This thesis presents results of heterogeneous integration of InAs/InP semiconductor quantum dots (QDs) with photonic structures (waveguides, photonic crystals, and optical fibers) and their optical characterization for the purpose of quantum information processing realized on-chip. The characterization of devices fabricated using a large-area direct bonding technique allowed proving the successful hybrid integration of the InP and silicon-on-insulator (SOI) platforms, enabling the coupling of single photons emitted by QDs into the interior of the SOI chip. This approach offers a scalable and cost-effective solution for creating dense multi-source on-chip environments within complex quantum photonic circuits. Fabrication and characterization were focused on the telecom C-band for compatibility with fiber networks. Experimentally demonstrated light coupling between the InP and SOI platforms was evidenced by the observation of photons outcoupled at both the InP outcoupler and the cleaved facet of the SOI waveguide with a determined on-chip coupling efficiency of 5.1 % between the QD source and the SOI waveguide, with a high single-photon purity operation at the level of 98 %.

In addition, this thesis presents the development and characterization of an integrated quantum light source for long-haul fiber-optic quantum communication. Designed, fabricated, and optically characterized, a single-photon emitter was based on InAs/InP quantum dots embedded within an InP H1 point defect 2D photonic crystal cavity. For this device, a micro-transfer printing process was developed to transfer the photonic crystal with QDs to standard single-mode fiber. The integrated source was then characterized within a cryocooler at 15 K, demonstrating high-quality single-photon emission with a second-order autocorrelation function with purity of 86 % and stable operation. To validate the system's performance in a realistic setting, an all-fiber optical channel was established between two laboratory nodes. This fabrication and experimental investigation allowed for demonstration of a robust and plug-and-play single-photon source operating in the third telecom window, paving the way for practical and scalable quantum communication networks utilizing fiber-optic infrastructure.

A developed micro-transfer printing process enabled highly accurate, precise, and deterministic transfer of individual InP nanobeams with InAs/InP quantum dots within 1D photonic crystal cavities. With this advanced method, transfer with exceptional control given by sub-100 nm (1-sigma) accuracy and precision was achieved. It allowed the integration of these nanobeams into diverse configurations (also automatically with high throughput) and on various material platforms, including Si, SiN, InP waveguides, and metal contacts. The research presented in this thesis features direct bonding and especially micro-transfer printing as a universal integration technique for the development of quantum photonic integrated circuits.

Streszczenie

Niniejsza rozprawa przedstawia wyniki heterogenicznej integracji kropek kwantowych InAs/InP ze strukturami fotonicznymi takimi jak falowody, kryształy fotoniczne oraz ze światłowodami. Praca prezentuje badania takich zintegrowanych układów w kontekście ich wykorzystania w dziedzinie przetwarzania informacji kwantowej oraz późniejszego wytwarzania takich układów w większej skali. Charakteryzacja urządzeń wytworzonych z wykorzystaniem techniki bezpośredniego łączenia pozwoliła potwierdzić skuteczną integrację platform InP oraz Si, umożliwiając sprzężenie pojedynczych fotonów emitowanych przez kropki kwantowe do wnętrza układu fotonicznego. To podejście oferuje skalowalne rozwiązanie do wytwarzania wielu emiterów na jednym chipie w kontekście realizacji złożonych kwantowych układów logicznych. Proces wytwarzania i charakteryzacja zostały ukierunkowane na pasmo telekomunikacyjne C, aby zapewnić kompatybilność z sieciami światłowodowymi. Eksperymentalnie wykazano sprzężenie światła pomiędzy platformami InP i Si poprzez obserwację fotonów wyemitowanych zarówno z chipu, jak i falowodu Si znajdującego się na krawędzi, uzyskując na chipie wydajność sprzężenia na poziomie 5.1 % pomiędzy źródłem pojedynczych fotonów a falowodem Si, jednocześnie zachowując wysoką czystości emisji pojedynczych fotonów na poziomie 98 %.

Rozprawa przedstawia również opracowanie i charakteryzację zintegrowanego źródła pojedynczych fotonów do komunikacji kwantowej. Zaprojektowany, wytworzony i scharakteryzowany optycznie emiter pojedynczych fotonów bazuję również na kropkach kwantowych InAs osadzonych we wnęce dwuwymiarowego kryształu fotonicznego z InP. W celu integracji tego urządzenia opracowano proces technologiczny z wykorzystaniem druku mikrotransferowego pozwalający na przeniesienie kryształu fotonicznego na standardowy światłowód jednomodowy. Źródło zostało następnie scharakteryzowane w temperaturze 15 K, wykazując emisję pojedynczych fotonów podczas pomiaru autokorelacji drugiego rzędu o czystości na poziome 86 % oraz stabilną emisję. Proces wytwarzania oraz przeprowadzone eksperymenty pozwoliły na demonstrację wysokiego potencjału zastosowania takiego urządzenia jako źródła pojedynczych fotonów pracującego w trzecim oknie telekomunikacyjnym, torując drogę do praktycznych i skalowalnych sieci komunikacji kwantowej wykorzystujących infrastrukturę światłowodową.

Opracowany proces druku mikrotransferowego umożliwił precyzyjne i deterministyczne przenoszenie pojedynczych falowodów InP z kropkami kwantowymi InAs/InP umieszczonymi w jednowymiarowych kryształach fotonicznych. Metoda ta pozwoliła osiągnąć dokładność i precyzję transferu poniżej 100 nm. Umożliwiło to deterministyczną integrację tych struktur z falowodami Si, SiN, InP, oraz kontaktami metalicznymi. Prezentowane w tej rozprawie badania podkreślają znaczenie techniki bezpośredniego łączenia oraz, w szczególności druku mikrotransferowego jako uniwersalnej metody integracji do rozwoju zintegrowanych układów fotoniki kwantowej.

Contents

List of Figures

List of Tables

List of Abbreviations

AFC	Atomic Frequency Comb	**AFM**	Atomic Force Microscopy
AM	Alignment Mark	**AOE**	Advanced Oxide Etch
BB84	Bennett and Brassard QKD protocol	**BCB**	Benzocyclobutene
BHF	Buffered Hydrofluoric Acid	**BOE**	Buffered Oxide Etch
BOX	Buried Oxide	**CAD**	Computer Aided Design
CBG	Circular Bragg Grating	**CCD**	Charge-Coupled Device
CMOS	Complementary metal–oxide–semiconductor	**CNRS**	French National Centre for Scientific Research
CSAR	Chemical Semi Amplified Resist	**CW**	Continuous Wave
CX	Charged Exciton	**DB**	Direct Bonding
DBR	Distributed Bragg Reflector	**DI**	Deionized Water
DOI	Digital Identifier of an Object	**DOS**	Density of States
DTU	Technical University of Denmark	**DVS**	Divinylsiloxane
EIT	Electromagnetically Induced Transparency	**FC**	Fiber coupling, Ferrule Connector
FDTD	Finite-Difference Time-Domain	**FIB**	Focused Ion Beam
FLAME	Fast Ladder Memory	**FSR**	Free Spectral Range
FSS	Fine Structure Splitting	**FWHM**	Full Width at Half Maximum
GUI	Graphical User Interface	**HBT**	Hanbury Brown and Twiss
HMDS	Hexamethyldisilazane	**HOM**	Hong–Ou–Mandel
HSQ	Hydrogen Silsesquioxane	**ICP**	Inductively Coupled Plasma
IPA	Isopropyl Alcohol	**IQPC**	Integrated Quantum Photonic Circuit
IR	Infrared	**KLM**	E. Knill, R. Laflamme and G. J. Milburn protocol
LEDs	Light Emitting Diode	**MBE**	Molecular Beam Epitaxy
MEMS	Microelectromechanical System	**MFD**	Mode Field Diameter
MIR	Mid-infrared	**ML**	Monolayer
MLA	Maskless Aligner	**MOCVD**	Metalorganic Vapour-phase Epitaxy
MOVPE	Metalorganic Vapour-phase Epitaxy	**MTP, µTP**	Micro-transfer Printing
MZI	Mach–Zehnder Interferometer	**NA**	Numerical Aperture
NILT	NIL Technology	**NIR**	Near-infrared
NQP	Nonlinear Quantum Photonics	**NV**	Nitrogen-vacancy
OCT	Optical Coherence Tomography	**ORCA**	Off-resonant Cascaded

			Absorption
PDMS	Polydimethylsiloxane	**PECVD**	Plasma-enhanced Chemical Vapor Deposition
PIC	Photonic Integrated Circuit	**PL**	Photoluminescence
PhC	Photonic Crystal	**PhCC**	Photonic Crystal Cavity
QD	Quantum Dot	**QED**	Quantum Electrodynamics
QKD	Quantum Key Distribution	**QLED**	Quantum Light Emitting Diode
RIE	Reactive Ion Etching	**ROI**	Region of Interest
SEM	Scanning Electron Microscope	**SK**	Stranski-Krastanov
SM	Single-mode	**SMF**	Single-mode Fiber
SNSPD	Superconducting Nanowire Single-Photon Detector	**SOC**	System On Chip
SOI	Silicon On Insulator	**SPAD**	Single Photon Avalanche Diode
SPDC	Spontaneous Parametric Down-Conversion	**SPS**	Single-Photon Source
SSPD	Superconducting Single-Photon Detector	**TCOs**	Transparent Conducting Oxides
TE	Transverse Electric	**TES**	Transition-Edge Sensor
TM	Transverse Magnetic	**TMAH**	Tetramethylammonium Hydroxide
UV	Ultraviolet	**WG**	Waveguide
WL	Wetting Layer	**WUST**	Wrocław University of Science and Technology
X, XX	Exciton, Biexciton	$\mathbf{k_B}$	Boltzmann Constant
µPL	Microphotoluminescence	**qPIC**	Quantum Photonic Integrated Circuit
µTP	Micro-transfer Printing		

Chapter 1

Introduction

1.1 Motivation

Quantum photonic integrated circuits (qPICs) hold significant promise in enabling large-scale fault-tolerant universal quantum computation [1–8]. This is one of the most prominent goals in quantum information processing, where quantum mechanical effects such as superposition [9] and entanglement [10] are used to process information. Given that many natural systems are inherently quantum and involve large Hilbert spaces, a clear application is to attempt to simulate these systems. The limitations of current computers lie in the exponential growth of the number of operations and parameters necessary to process and store the information in the system [11]. By directly mapping the time evolution of a quantum system to the propagation of single photons within qPICs, quantum simulations can be carried out using linear quantum photonics algorithms, requiring many fewer resources compared to classical simulations. qPICs can be used for combinatorial optimization [12] and quantum physics simulations [13]. Currently, compared to modern conventional processors, quantum computers based on superconducting circuits and photons have shown a computational advantage, although they are designed to solve only very specific problems [14]. Photon-based PIC technology can integrate numerous optical components onto compact chips, leveraging the mature photonics manufacturing and fabrication industry [15]. As demonstrated by the Knill-Laflamme-Miliburn [16] (KLM scheme), universal all-optical quantum computing is feasible using a few elements, which are: indistinguishable single-photon sources, linear-optical quantum circuits, and single-photon detectors. Based on that, one key challenge in the development of qPIC is the creation of efficient and integrated single-photon sources [17] with their operation at 1550 nm being beneficial due to the high transmission of signal. However, to leverage quantum information processing within silicon-based PICs, it is essential to incorporate single-photon emitters, likely made from different materials, to address the inherent limitations of the silicon platform in the generation of light [18]. Consequently, considerable effort has been made to effectively integrate direct-bandgap emissive materials with it. Various technological approaches are available for III-V-on-Si integration, including well-established methods like flipping a chip followed by direct or adhesive bonding, as well as emerging techniques

such as direct epitaxial growth or micro-transfer printing (μTP). Quantum emitters such as semiconductor quantum dots (QDs), known for their excellent single-photon properties [19, 20], are one of the proposed quantum emitters that have already been integrated with various photonic circuit platforms [1, 2, 6, 7, 21], showing great promise in this application. When these emitters are embedded in bulk dielectric materials, their emission rates are typically too low for efficient information processing. Certain electromagnetic environments like photonic crystals and cavities can boost these emission rates through Purcell enhancement, and experiments have shown that it is possible to preserve the quality of single-photon sources (SPSs) in such settings, which motivates further engineering of light-matter coupling in a form of photonic crystal cavities (PhCC) with SPS. This thesis directly goes into these integration challenges and provides fabrication solutions and experimental verifications.

1.2 Thesis structure

This work is driven by the goal of integrating quantum emitters with photonic integrated circuits to form a demonstration of applicable qPIC. The dissertation is structured into 6 chapters. The key concepts are introduced in the first chapter. In subsequent chapters, the created fabrication and integration processes are presented along with the experimental results and conclusions derived from this research.

- **Chapter 1 - Introduction**: This chapter begins with the motivation behind the research, potential benefits of developing qPICs for quantum information technologies are highlighted. The research goals and methodologies are stated. The key concepts regarding quantum dots (growth, confinement, and excitonic complexes) are introduced. Essential photonic elements required for qPICs are presented. This chapter also describes the experimental setup configurations used to investigate the samples, including the standard microphotoluminescence experiment, as well as its specific orthogonal configuration and the setup with the all-fiber-coupled detection configuration. Additionally, there is a description of the developed software used for the stabilization of the structures during the photoluminescence experiment.

- **Chapter 2 - Fabrication**: This chapter outlines the workflow developed for the samples' fabrication, as it is described in Sect. 1.3. It also provides an overview of the technology and the equipment used in the process (lithography, characterization, wet and dry etching). Last, a comprehensive description of the newly developed micro-transfer printing technique is given.

- **Chapter 3 - Direct Bonding**: In this chapter, the device design and FDTD simulations are provided. The optical characterization is divided in the section on microphotoluminescence experiments in normal and orthogonal configurations, finalized with single-photon measurements (to assess on-chip single-photon purity).

- **Chapter 4 and 5 - Heterogeneous integration with micro-transfer printing**: These chapters describe the results of the fabrication and the experimental investigation of the heterogeneously integrated InAs/InP QDs PhCCs with fiber, SOI chip, SiN waveguides, and metal contacts using micro-transfer printing. Additionally, this chapter provides an analysis of the micro-transfer printing precision and accuracy.

- **Chapter 6 - Summary and conclusions**: The summary of the key results of this work is presented.

1.3 Investigated samples, contributions, and publications

This thesis presents experimental results for 5 types of structures, all fabricated in the Nanolab facility at the Technical University of Denmark (DTU). All the structures are based on epitaxial InAs QDs embedded in the InP matrix and emitting between 1.5 µm and 1.6 µm photon wavelengths. In all of the cases, the epitaxial quantum dots were fabricated by the team of Dr. Elizaveta Semenova at DTU. The QDs' physical environment (InP) was lithographically defined to form microsized photonic structures: waveguides (referred to as nanobeams), 1D photonic crystal cavities, tapers, H0 and H1 photonic crystal cavities. These nanostructures were hybridized either with Si, SiN, or InP waveguides, and with a single-mode fiber core or metal contacts, using either direct bonding or micro-transfer printing. Chapter 3, describes the fabrication of a sample with heterogeneously integrated InAs/InP QDs with the SOI platform using direct bonding. This structure was fabricated mainly by Dr. Paweł Holewa and Dr. Aurimas Sakans under the supervision of Dr. Elizaveta Semenova and Prof. Kresten Yvind. The spectral characterization of the structure described in Sect. 3.2.1 was performed by the author under the supervision of Dr. Paweł Mrowiński and Prof. Marcin Syperek. During a 6-month internship at DTU, the author developed a micro-transfer printing process flow which was used for the first time at DTU to fabricate the structures described in Chapters 4 and 5. Studies on this type of structure were presented in Chapt. 5. For the samples fabricated by µTP, the target SiN waveguides were provided by Dr. Yi Zheng and the SOI chip with Si waveguides and outcouplers was provided by Prof. Yunhong Ding, both from DTU. The authors' contributions are presented in Tab. 1.1.

Samp. name	Ch.	Fab.[1, 2]	Simulations	Exp.[3]	Manuscript[4]
Direct Bond.	3[5]	Dr. P. Holewa Dr. A. Sakanas	Dr. P. Mrowiński	Author	Author
Fiber	4[6]	Author	Author	Author	Author
SOI	5.1	Author[7]	Not included	Author	-
SiN	5.2	Author[8]	Not included	Author	-
Met. Contacts	5.3	Author	-	Author	-

TABLE 1.1: Authors contributions.

[1] Fabrication was done under supervision of Dr. Elizaveta Semenova and Prof. Kresten Yvind.
[2] InP wafers with QDs were grown by Dr. Paweł Holewa and he performed an e-beam lithography process steps.
[3] Experiments were done under Dr. Paweł Mrowiński and Assoc. Prof. Marcin Syperek's supervision.
[4] Author of the first version of the manuscript.
[5] Work in this chapter was published in Optics Express [22].
[6] Work in this chapter is available on ArXiv [23].
[7] SOI chip with outcouplers was provided by Prof. Yunhong Ding.
[8] SiN chip with waveguides was provided by Dr. Yi Zheng.

Publications

Certain results and figures shown in this work have been previously published in the following publications:

1. **Marek Burakowski**[9], Paweł Holewa, Paweł Mrowiński, Aurimas Sakanas, Anna J. Musiał, Grzegorz Sęk, Kresten Yvind, Elizaveta S. Semenova, Marcin G. Syperek, *Heterogeneous integration of single InAs/InP quantum dots with the SOI chip using direct bonding*. **Optics Express**, Volume **32**, 2024. doi.org/10.1364/OE.515223 - **Editor's Pick**.

2. **Marek G. Mikulicz**, Paweł Mrowiński, Paweł Holewa, Kresten Yvind, Marcin Syperek, Elizaveta Semenova, *InAs/InP quantum dot based C-Band all-fiber plug-and-play triggered single-photon source integrated using micro-transfer printing*. **ArXiv**, 2024, ArXiv:2411.16490 - In the process of reviewing in the journal: Physical Review Applied

3. **Marek G. Mikulicz**, *microStabilize: In-plane microstructure stabilization in optical microscopy via normalized correlation coefficient matching method*. **SoftwareX**, Volume **29**, 2025. doi.org/10.1016/j.softx.2025.102065.

The following papers were published during the PhD but are not included in this thesis:

1. Paweł Holewa, Daniel A. Vajner, Emilia Zięba-Ostój, Maja Wasiluk, Benedek Gaál, Aurimas Sakanas, **Marek Burakowski**, Paweł Mrowiński, Bartosz Krajnik, Meng Xiong, Kresten Yvind, Niels Gregersen, Anna J. Musiał, Alexander Huck, Tobias Heindel, Marcin G. Syperek, Elizaveta S. Semenova, *High-throughput quantum photonic devices emitting indistinguishable photons in the telecom C-band*. **Nature Communications**, Volume **15**, 2024. https://doi.org/10.1038/s41467-024-47551-7.

2. Maciej Jaworski, Paweł Mrowiński, **Marek G. Mikulicz**, Paweł Holewa, Laura Zeidler, Marcin Syperek, Elizaveta Semenova, and Grzegorz Sęk, *Xenon plasma-focused ion beam milling for fabrication of high-purity, bright single-photon sources operating in the C-band*, **Optics Express**, Volume **32**, 2024. https://doi.org/10.1364/OE.534313.

3. **Marek Burakowski**, Paweł Mrowiński, Michał Gawełczyk, Johann P. Reithmaier, Sven Höfling, Grzegorz Sęk, *Diamagnetic coefficients and g-factors of InAs/InGaAlAs quantum dashes emitting at telecom wavelengths*, **Journal of Applied Physics**, Volume **132**, 2022. https://doi.org/10.1063/5.0101345.

4. Paweł J. Podemski, Michał Gawełczyk, Paweł D. Wyborski, Hanna Salamon, **Marek Burakowski**, Anna J. Musiał, Johann P. Reithmaier, Mohamed Benyoucef, Grzegorz Sęk, *Spin memory effect in charged single telecom quantum dots*, **Optics Express**, Volume **29**, 2021. https://doi.org/10.1364/OE.438708.

[9] Author's family name

5. Wojciech Rudno-Rudziński, **Marek Burakowski**, Johann P. Reithmaier, Anna J. Musiał, Mohamed Benyoucef, *Magneto-optical characterization of trions in symmetric InP-based quantum dots for quantum communication applications*, **Materials**, Volume **14**, 2021. https://dx.doi.org/10.3390/ma14040942.

6. Paweł Holewa*, **Marek Burakowski***, Anna J. Musiał, Nicole Srocka, David Quandt, André Strittmatter, Sven Rodt, Stephan Reitzenstein, Grzegorz Sęk, *Thermal stability of emission from single InGaAs/GaAs quantum dots at the telecom O-band*. **Scientific Reports**, Volume **10**, 2020. https://doi.org/10.1038/s41598-020-78462-4 - *Equal contribution.

Additionally, the research presented in this thesis was recognized with the Max Born Scholarship of the President of Wrocław (2024) and a distinction in the Leonard Sosnowski Prize (2023) awarded to the author.

1.4 Research goals and methodology

Research goals

- Demonstrating the feasibility of direct bonding for the integration process of InAs/InP QDs and SOI platforms, enabling efficient coupling of single photons generated by QDs into the silicon photonic chip. Next, characterization of the performance of the integrated device, including demonstration of light coupling between InP and SOI platforms, measurement of single-photon emission characteristics (e.g., single photon generation purity), and evaluation of photon coupling efficiency into the Si waveguide.

- Developing the InAs/InP QD-based, fiber-integrated single-photon source structure coupled to photonic crystal cavities, including design, fabrication, and characterization. The structure with InAs/InP quantum dots is integrated by micro-transfer printing with a single-mode optical fiber. Subsequently, testing the device's applicability to long-haul quantum communication by establishing a stable, all-fiber quantum link between two laboratory nodes.

- Developing the process for micro-transfer printing of micrometer-sized waveguides with InAs/InP QDs to various photonics material platforms (SOI, SiN, InP, metal contacts) with defined microstructures (waveguides, gratings, edge outcouplers), as well as characterization in terms of accuracy and precision of the transfer and its impact on the spectral and electrical response of the devices.

Methodology

Research methodology can be divided into device fabrication, integration, and characterization in a cleanroom, optical characterization in spectroscopy laboratories,

and numerical simulations in commercially available software (Ansys Lumerical). A description of each technique is given in the first two chapters, including:

- Device fabrication, characterization and integration - numerous fabrication methods available in a cleanroom environment were utilized, including techniques such as: optical and electron beam lithography (to define the InP waveguides, cavities and other nanometer-precise components), wet and dry etching, SEM and AFM characterization, direct bonding (for high yield fabrication), micro-transfer printing (allowing a pick-and-place deterministic integration).

- Optical characterization - multiple spectroscopy techniques were used to characterize optical properties of the devices, these techniques include: high spectral and spatial resolution microphotoluminescence, polarization and time resolved photoluminescence measurements (second-order autocorrelation and photoluminescence decay), also in all-fiber setup and orthogonal configuration. These experiments are conducted to estimate the light coupling efficiency between different hybridized platforms, a QD single-photon emission purity, and overall performance of the integrated system.

- Numerical simulations and modeling - 3D finite-difference time-domain simulations allowed to optimize cavity designs to match the target C-Band window and predict coupling efficiencies for various components (hybrid waveguides and couplers) in photonic integrated circuits.

Overall, as presented in subsequent chapters, these techniques allowed for the fabrication and characterization of devices presented in this thesis. High variance of the design and materials in the fabricated devices, spanning from the millimeter scale integration with Si waveguides to sub 100 nm precise deterministic transfer, shows high versatility of these techniques for fabricating various structures for quantum photonic integrated circuits. Spectroscopy measurements allowed to provide pivotal information about the on-chip photons in photonic integrated circuits, with the information on the single-photon emission purity, identification of excitonic complexes being the source of single photons, long-term signal stability throughout the laboratory nodes, and on-chip coupling efficiency being crucial for their further development.

1.5 Quantum dots

The growth of semiconductor quantum dots (also known as zero-dimensional semiconductor nanostructures) has been the subject of numerous studies since the 1990s. Because of their extremely small size in the range of nanometers (for epitaxially grown, typically lens-shaped QDs with a small height in the range of a few nanometers and a larger diameter of tens of nanometers), they confine charge carriers in all three dimensions. Over the past three decades, self-assembled semiconductor QDs have attracted significant interest both due to interesting fundamental physics and due to their application potential (Nobel Prize in Chemistry in 2023). For instance, QD lasers can offer several benefits, including a temperature-insensitive threshold current, a lower threshold current density compared to quantum well lasers, high differential gain, and a broad modulation bandwidth [24, 25]. Furthermore, QD infrared photodetectors are expected to exhibit high responsivity and detectivity, effectively respond to normally incident infrared light, and can function in a wider temperature range [26, 27]. QDs also hold great promise for the development of other advanced devices such as optical and electronic memories, triggered single-photon sources, entangled photon-pair sources, optically triggered single-electron sources, and all-optical quantum gates [28–32]. Their application is also found in commercially available devices such as large-area QLED TVs [33], in the automobile industry [34], and in the sector of wearable electronics [35]. For novel physics, QDs coupled to photonic cavities are used to study quantum cavity electrodynamics [36, 37] (for more details see Sect. 1.5.6.1), interaction with the nuclear spin reservoir [38, 39], and coupled QD systems [40–42].

1.5.1 Quantum dot growth

Quantum dots can be fabricated through various growth techniques, including colloidal synthesis, the sol-gel process, and epitaxial methods such as molecular beam epitaxy (MBE) or metalorganic chemical vapour deposition (MOCVD). Typically, high-quality semiconductor QDs are grown using MBE (with ultrapure materials used in effusion cells) and MOCVD. To confine the carriers in three dimensions, the QD material is surrounded by the larger bandgap matrix material. Typically, quantum dots are grown using the Stranski-Krastanow (SK) growth mode, [43–45], growth modes are visualized in Fig. 1.1 . QDs are formed through coherent heteroepitaxy involving two materials with a lattice mismatch. Initially, as a result of the substrate's higher surface energy, the deposited material forms a pseudomorphic (2D) wetting layer (WL) over the first few monolayers (ML). However, the lattice mismatch induces compressive strain and a build-up of elastic energy within the epitaxial layer. Once the WL exceeds a certain thickness, known as the critical thickness, a spontaneous transition from 2D to 3D growth mode occurs, leading to the formation of QDs. This model suggests that the transition rate from the WL to

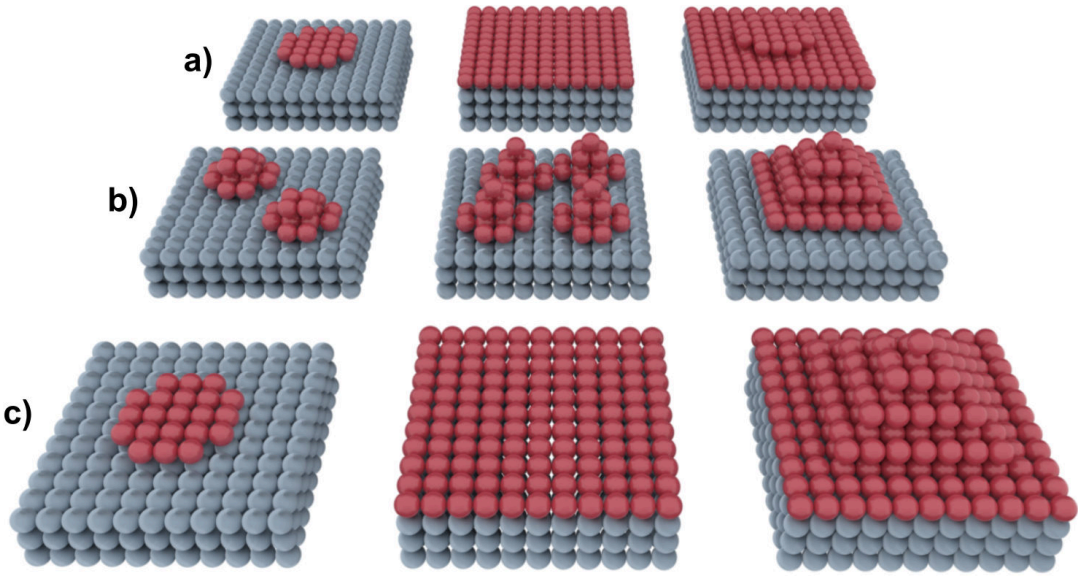

FIGURE 1.1: Visualization of the three distinct growth modes: a) Frank–Van der Merwe, b) Volmer–Weber, and c) Stranski–Krastanov. Overlayer atoms (red) and substrate atoms (blue) are depicted.

QDs increases as the WL thickness and associated strain accumulate. This acceleration continues until the WL consumption rate balances the material supply from the growth precursors. Then these QDs, in the form of typically flat, lens-shaped atomic islands, are capped to protect the QD crystal structure and their surface from oxidation and the adverse influence of surface states. As an alternative, epitaxial QDs can also be formed in the droplet epitaxy process [46], where the deposition of metal nanodroplets [47] (e.g. from Ga or Al) on the surface creates nanoholes under certain conditions that can later be filled with a QD material. Since this approach is not stress-driven, it can lead to the formation of QDs with higher in-plane symmetry, desired, e.g. for the generation of entangled photon pairs.

1.5.2 Quantum confinement

The de Broglie wavelength (λ_D) serves as an approximate measure of the spatial extent or "size" of a particle in terms of its quantum wave properties. For an electron in a semiconductor, it is on the order of a few tens of nanometers, which is about two orders higher than the distance between the nearest-neighbor atoms. It can be approximated by:

$$\lambda_D \sim \frac{h}{\sqrt{m_e^* k_B T}} \tag{1.1}$$

where h is Planck's constant, m_e^* is the effective mass of the electron, k_B is the Boltzmann constant, and T is the temperature. If the dimensions of the structure are reduced to the order of λ_D then the motion of a carrier is confined.

The behavior of electrons in large-scale semiconductor crystals is described using the Schrödinger equation, which connects the crystal lattice potential to the electron's energy by the equation:

$$\left[\frac{\mathbf{p}^2}{2m_0} + V(\mathbf{r})\right]\Psi = \left[-\frac{\hbar^2}{2m_0}\Delta + V(\mathbf{r})\right]\Psi \\ H\Psi = E\Psi \tag{1.2}$$

The momentum operator is defined as $\mathbf{p} = -i\hbar\nabla$, $\mathbf{r}$ represents the position vector, m_0 denotes the mass of a free electron, and $V(\mathbf{r})$ corresponds to the periodic potential of the crystal lattice. Bloch's theorem states that the solutions to the Schrödinger equation within a crystalline structure take the form of Bloch waves, which can be expressed as:

$$\Psi = e^{ik\cdot\mathbf{r}}u_k(\mathbf{r}) \tag{1.3}$$

The wave vector of the electron, $\mathbf{k}$, and the Bloch function, u_k, which exhibits the spatial periodicity of the crystal lattice, define Bloch waves. These waves are expressed as the product of a plane wave, $e^{i\mathbf{k}\cdot\mathbf{r}}$, and the periodic Bloch function $u_k(\mathbf{r})$, capturing both the atomic and macroscopic characteristics of the wavefunction within a crystal. The Schrödinger equation solutions can be derived straightforwardly under the assumption of periodic lattice potentials, as modeled by the Kronig-Penney approach. These solutions establish a relationship between the energy eigenvalue and the magnitude of the $\mathbf{k}$-vector via the effective mass in the crystal, m^*, following a parabolic expression.

$$E = \frac{\hbar^2\mathbf{k}^2}{2m^*} \tag{1.4}$$

The application of Born-von Kármán periodic boundary conditions defines the allowed $\mathbf{k}$-vector values within a macroscopic crystal. These values are specified for each spatial dimension L_i and where n_i are integers as follows:

$$k_i = \pm n_i\frac{2\pi}{L_i} \tag{1.5}$$

Aforementioned confinement reduces the density of states $D(E)$ and this analysis directly pictures the allowed energy-dependent density of states based on the dimensionality of quantum confinement presented in Fig 1.2 which depicts how the $D(E)$ changes with the reducing dimensionality of the structure going through the bulk material with the density of states taking the form of a square root of E and the quantum well, where $D(E)$ takes the form of "steps" (Fig. 1.2 - purple line). The energy position of the "steps" can be engineered by adjusting the thickness of the well. Further reducing dimensions in two directions leads to the formation of a quantum wire, and in all three dimensions - a QD. In the latter case, the carriers' movement is effectively frozen. This system is referred to as 0D. As seen in Fig. 1.2 (black line), for the QD, the density of states is discretized, taking the form of the Dirac function,

which is similar to what is observed in atoms. Therefore, QDs, albeit consisting of a few thousand atoms, are sometimes called by a simplifying analogy "artificial atoms" because they exhibit the same density of states as an atom, but their properties can be engineered. Most importantly, their emission energy can be controlled with size. As a drawback, the electrons in QDs undergo coupling with their crystalline environment. This coupling can involve lattice phonons or electrostatic interactions between the electrons of a QD and those of the surrounding crystal (Auger effect at high carrier concentration, N-body effect, and Coulomb interactions between charge carriers). This QD interaction with its environment leads to a significant broadening of the photoluminescence peaks Fig. 1.2 (dotted line). At elevated temperatures, the spectral lines broaden, reaching several meV at room temperature. This substantial homogeneous broadening observed at room temperature is one of a key distinctions between QDs and atoms.

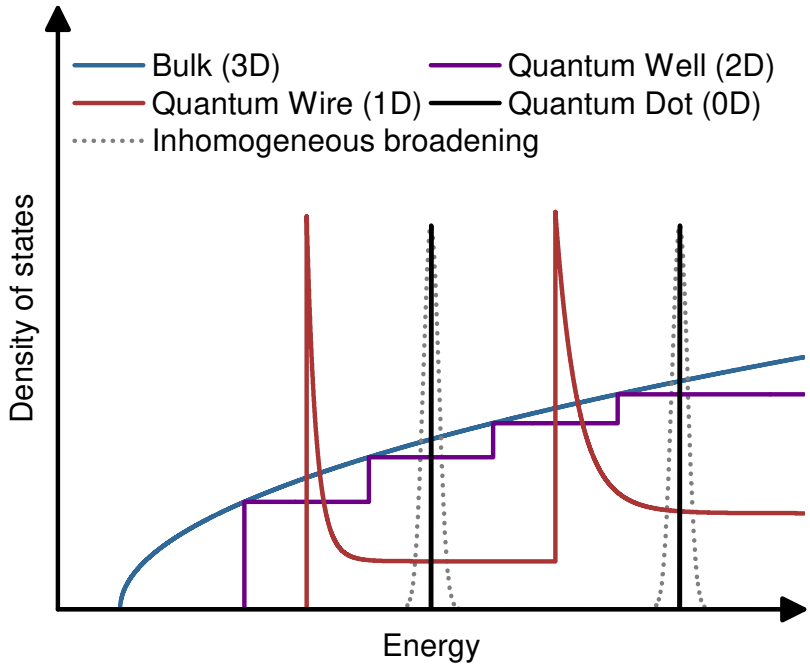

FIGURE 1.2: Density of states as a function of energy for various dimensional systems, including bulk (3D), quantum wells (2D), quantum wires (1D), and quantum dots (0D), with dotted line accounting for inhomogeneous broadening effects illustrated for actual quantum dot structures.

1.5.3 InAs Quantum Dots

At the beginning of QD research, less attention has been placed on InAs QDs grown on InP substrates [48–50], where InAs QDs were fabricated first on a GaAs substrate, with a change in their applicability to telecom wavelengths due to the development of metamorphic buffer layers [51, 52]. InAs QDs on GaAs typically emit wavelengths shorter than 1200 nm, generally centered around 900 nm, primarily due to compressive strain that results in a noticeable blue-shift compared to the bulk emission of

InAs (although their emission wavelength can successfully be shifted toward 1550 nm [53]). InAs QDs in the InP matrix can emit over a broader range of 1200-2300 nm. This makes InAs/InP QDs naturally more suitable for optoelectronic devices operating in the 1300-1550 nm range, crucial for long-distance optical fiber communication systems using single-mode silica fiber with zero chromatic dispersion at 1310 nm and minimal attenuation at 1550 nm (see also Sect. 1.6.3). Not mentioning low attenuation in PIC based on Si and SiN, such wavelengths are also beneficial for biological imaging systems [54] where optoelectronic devices using InAs/InP QDs can be applied in optical coherence tomography (OCT), offering high-resolution images of biological tissues, and are valuable in fields such as ophthalmology, neurology, and endoscopy [55]. Extending the emission wavelength to 2300 nm makes these QDs useful for environmental monitoring and remote sensing of gases. Overall, the capability to grow and adjust the emission wavelength of InAs/InP QDs holds significant technological importance. Strong carrier binding in InAs/InP QDs supports room-temperature applications, with significant hole confinement energy (around 400 meV), suggesting potential use in memory devices [56]. Among III-V materials, InAs exhibits high electron mobility [57]. The effective masses of electrons and holes in these QDs are reduced compared to those in GaAs [58], leading to larger energy-level separation, reducing excited-state populations, and the system, in turn, requires a higher phonon energy to promote a carrier to a higher level. InAs/InP QDs are expected to show single-photon operation at elevated temperatures [59, 60]. Atomistic calculations reveal (Tab. 1.2) that s-p level spacings are:

s-p level spacing	**InAs/InP QD**	**InAs/GaAs QD**
Electron	50-70 meV	70-80 meV
Hole	20-30 meV	10-20 meV

TABLE 1.2: Comparison of s-p level spacing for electrons and holes in InAs/InP and InAs/GaAs quantum dots (after Ref. [61]).

Table 1.3 summarizes the key physical parameters of GaAs, InAs, and InP, which are critical for modeling and understanding their suitability in optoelectronic applications.

Parameter	Symbol	Units	GaAs	InAs	InP
Effective heavy hole mass	m^*_{hh}	m_0	0.41	0.39	0.44
Effective light hole mass	m^*_{lh}	m_0	0.071	0.028	0.10
Effective electron mass	m^*_e	m_0	0.068	0.025	0.091
Bandgap energy	$E_g(\Gamma)$	eV	1.424	0.354	1.342
Lattice constant	a	nm	0.565325	0.60583	0.58697
Static dielectric constant	ϵ_r	-	13.1	14.6	12.4
Effective Bohr radius	a^*_B	nm	10.2	30.9	7.2
Rydberg constant	R^*	meV	4.6	1.5	6.7

TABLE 1.3: Key parameters for GaAs, InAs, and InP at T=300 K (after Ref. [62]).

InAs/InP Groups

The reference map in Fig. 1.3, based on the bibliographic data generated through the OpenAlex API via VOSviewer, shows the academic landscape in the development of InAs/InP QD-based single-photon devices in 2024. By analyzing co-authorship between organizations with a minimum document threshold of 10, the map highlights significant collaborations, particularly the position of WUST showing its research network with the Technical University of Denmark (DTU) and German universities (University of Kassel, Würzburg, and Berlin).

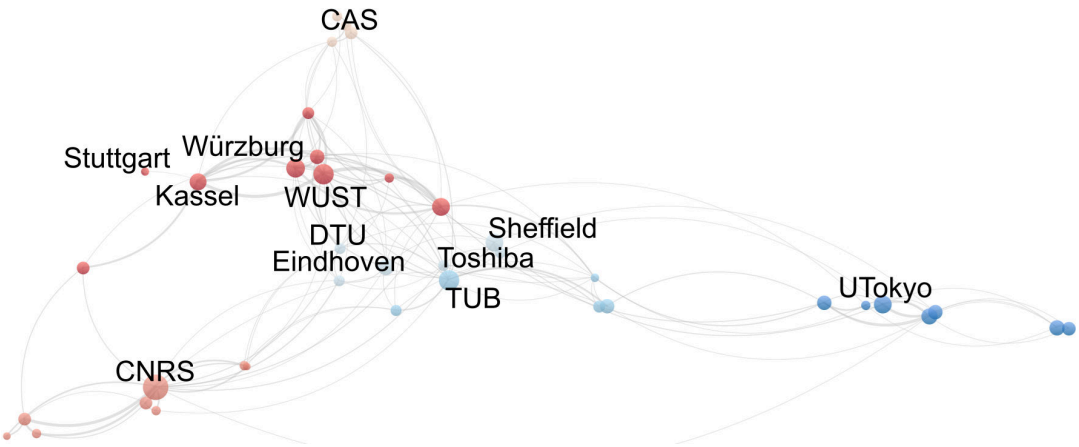

FIGURE 1.3: Co-authorship landscape of the development of InAs/InP QD-based single-photon devices in 2024 highlighting position of WUST, DTU, TUB, Kassel, Würzburg, Stuttgart, Sheffield, Toshiba, Stuttgart, Eindhoven, CNRS, and UTokyo.

1.5.4 Excitonic complexes in QDs

To set up the discussion relevant to subsequent chapters, it is crucial to introduce and analyze the fundamental excitations confined to quantum dots. The most basic excitation is the neutral exciton, formed by the Coulomb attraction between an electron and a hole. In most semiconductors, the relatively large dielectric constants

(e.g., the static dielectric constant for InAs is 14.6) lead to significant screening of the Coulomb interaction. Consequently, the exciton radius in bulk materials becomes several times larger than the lattice spacing, giving rise to what is known as a Wannier-Mott exciton.

The Coulomb-bound electron-hole pair in such systems can be described using a hydrogen-like Hamiltonian:

$$\hat{H} = -\frac{\hbar^2}{2m_h}\nabla_h^2 - \frac{\hbar^2}{2m_e}\nabla_e^2 - \frac{e^2}{\varepsilon|\mathbf{r}_e - \mathbf{r}_h|} \tag{1.6}$$

where m_e and m_h are the effective masses of the electron and the hole, and ϵ is the dielectric constant. This model, while useful for introductory purposes, is highly simplified. It neglects essential factors such as the shape of the confining potential, strain effects, and exchange correlation. These factors significantly influence the exciton's energy and behavior, necessitating more advanced theoretical models [63]. When the dimensions of a quantum dot approach the Bohr radius of the bulk exciton (discussed in the quantum confinement section), the exciton energy levels shift upward due to the increasing confinement energy. In the extreme case of small quantum dots, the last term in Eq. (1.6) becomes negligible, and the model reduces to the particle-in-a-box approximation. The typical sizes of quantum dots are on the order of the Wannier-Mott exciton radius, ensuring that the electron and hole are confined within the same spatial region. As a result, the exciton is the fundamental excitation in quantum dots. However, this simplistic view fails to capture the complexity of excitonic systems in quantum dots. Atomistic calculations for typical InAs/InP quantum dots, for example, reveal multiple confined states, including at least three electron states and six hole states (see Fig. 1.5). These states can combine to form over a hundred possible electron-hole configurations, ranging from the fundamental exciton to higher-order excitonic complexes. Each excitonic state can lead to optically active transitions, with different transition probabilities. This results in a µPL spectrum that includes lines corresponding to various excitonic complexes such as X^{1-}, X, XX, and X^{1+}, and other charged or multi-exciton states. These transitions exhibit diverse energies and intensities, reflecting the complexity of carrier configurations. Assignment of spectral lines solely based on transition energies is often ambiguous due to potential degeneracies among excitonic states. Thus, accurate identification of excitonic complexes requires advanced methodologies, which are discussed in detail in subsequent sections. Additionally, each excitonic complex has different temporal emission characteristics (e.g. excitons tend to produce photons with higher temporal coherence compared to biexciton states, and this coherence time can be tuned electrically [64]). Recognizing these allows for precise spectral alignment and photon pulse overlap and synchronization, leading to the highest indistinguishability, which is essential in scalable qPICs, especially when multiple QDs are used as photon sources. By distinguishing between excitonic states, unwanted interactions or crosstalk between different states can be minimized, leading

to higher fidelity in quantum operations within the circuit.

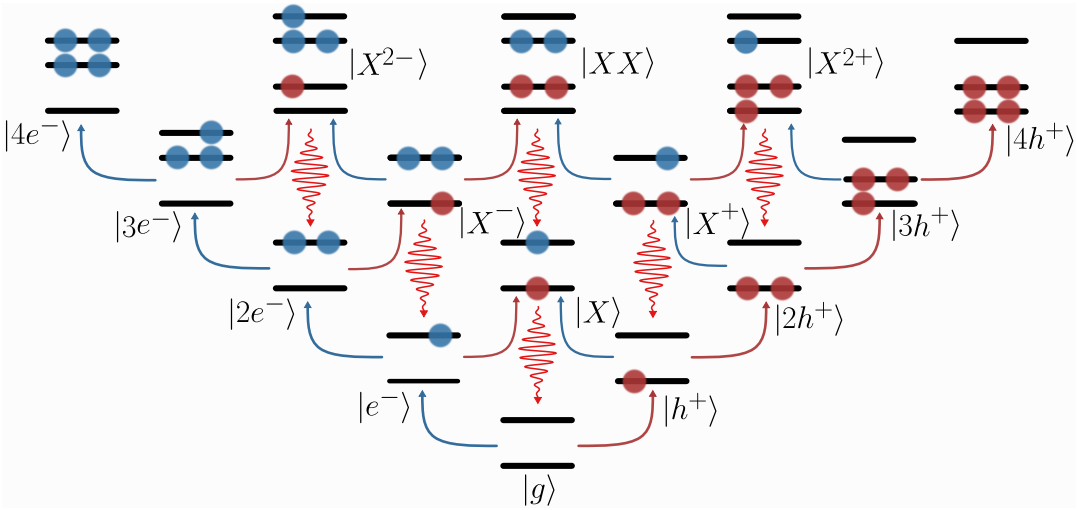

FIGURE 1.4: Scheme of the quantum dot carrier dynamics with accumulation of up to 4 carriers, occupying lowest energy levels. $|g\rangle$ is the ground state, $|ne(h)^{-(+)}\rangle$ is the n-electron(hole) state. $|X\rangle$ and $|XX\rangle$ are exciton and biexciton states and $|X^{n-(+)}\rangle$ are negatively(positively) charged exciton states. The addition of an electron (hole) is represented by the curved blue (red) arrow. This scheme omits the carriers spins and multiplet (doublet, triplet) states.

Binding energies

In a QD, the binding energy arises from the Coulomb interaction between carriers, including their direct attraction or repulsion, correlation (a many-particle effect) and exchange, which relates to the specific properties of the interacting fermions. The strength of correlation and exchange is influenced by the spatial overlap of the electron and hole wave functions. In bulk materials, because of the larger Bohr radius, the biexciton binding energy is significantly smaller than the exciton binding energy and can primarily be attributed to the correlation and exchange between two neutral excitons. Generally, the increased localization of excitons in QDs results in an increase in the biexciton binding energy. The binding energy of an excitonic complex can be defined as:

$$\Delta E_b(E^n) = E(X^n) - E(X), \tag{1.7}$$

where $E(X^n)$ is the recombination energy. Taking into account the direct Coulomb interaction between carriers $J_{ss}^{(ee)}$ for electrons and $J_{ss}^{(hh)}$ for holes, the basic excitonic complexes' binding energies can be expressed as follows:

$$\begin{aligned} \Delta E_b(X^+) &= J_{ss}^{(hh)} - J_{ss}^{(eh)}, \\ \Delta E_b(X^-) &= J_{ss}^{(ee)} - J_{ss}^{(eh)}, \\ \Delta E_b(XX) &= J_{ss}^{(hh)} + J_{ss}^{(ee)} - 2J_{ss}^{(eh)}. \end{aligned} \tag{1.8}$$

These binding energies are in the Hartree-Fock approximation and are neglecting the exchange interaction because it is smaller in magnitude than the direct Coulomb interaction. The values of the direct Coulomb interactions are given in Tab. 1.4.

Direct Coulomb interaction	InAs/InP QD	InAs/GaAs QD
$J_{ss}^{(eh)}$	~26 meV	~22 meV
$J_{ss}^{(hh)}$	~20 meV	~22 meV
$J_{ss}^{(ee)}$	~18 meV	~22 meV

TABLE 1.4: Values of direct Coulomb interactions for InAs/InP and InAs/GaAs QDs for a lens shaped dot with a height of 3 nm and diameter set to 25 nm, after [61]

.

Notably, this small Coulomb interaction (relative to atoms with $J \sim 10eV$) on the same order as the energy level spacing shown in Tab. 1.2 causes the electron and hole filling process to violate the Aufbau principle of shells filling, which means that multiple excitonic complexes can be observed at the same time. This is important in the exploration of the exciton dynamics in InAs/InP QDs.

Dynamics

The carrier dynamics in quantum dot structures are significantly different than in bulk materials, mainly due to the heterointerface between two materials and the discrete energy levels inherent in quantum dots. The dynamic evolution begins when carriers in a semiconductor are typically generated with a laser with an energy greater than the bandgap of the host material (in the case of InP $E_g \sim 1.42$eV $\sim$ 870 nm at 5 K) or they can also be injected electrically when possible. Carrier dynamics in QDs involve processes such as carrier relaxation, recombination, and transfer, which are influenced by the size, shape, and composition of QDs, as well as their surrounding environment. The dynamic carrier processes include the excitation of electrons from the barrier's valence band into the conduction band, creating free electrons and holes. The photogenerated (or electrically injected) carriers are not in thermal equilibrium, and their relaxation typically occurs through phonon interactions. These carriers relax from the barrier to the wetting layer before being captured into the quantum dots, either directly cascading down to the ground state or into higher energy states with subsequent relaxation, while radiative and nonradiative recombination processes dictate the emission properties. This relaxation is typically divided into four categories: coherent, non-thermal, hot carrier, and isothermal [65]. Additionally, interactions with nearby QDs or the surrounding matrix can lead to carrier transfer, carrier-carrier and carrier-phonon scattering, and electrons and holes are redistributed throughout the conduction and valence bands, further complicating the dynamics. Additionally, carriers may transfer from

the quantum dot to nearby deep levels, leading to trapping and/or nonradiative recombination. The relaxation of charge and spin occurs at different rates, influenced by Coulomb repulsion [66]. Finally, radiative recombination occurs when an electron and a hole recombine together, releasing energy in the form of a photon which can be measured in a µPL experiment.

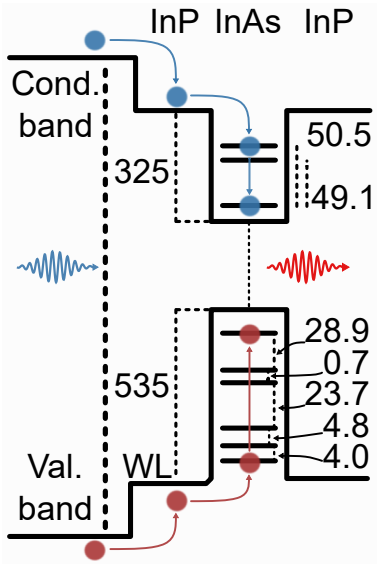

FIGURE 1.5: A schematic energy diagram along the growth direction, depicting carrier dynamics in quantum dot structures during nonresonant excitation within the barrier. Energies between levels are given in meV after Ref. [67].

Additionally, in respect to the dynamics, in the study of atom–field interactions (from which QD-cavity systems can inherit their insights) two different regimes can be identified: the strong coupling regime and the weak coupling regime. These regimes are categorized based on the value of the atom–field coupling constant, which is determined as follows:

$$\kappa = \frac{p_{ij}}{\hbar}\sqrt{\frac{\hbar\omega_0}{2\varepsilon_0 V}} \tag{1.9}$$

In this context, ω_0 represents the atomic transition frequency, p_{ij} denotes the dipole matrix element, and V refers to the volume of the cavity. The strong coupling regime is characterized by the condition $\kappa \gg \gamma$, where γ is the spontaneous decay rate inside the cavity. Within this regime, the emission spectrum of an atom placed in a cavity with a high-quality factor ($Q \to \infty$) exhibits two distinct peaks, which result from mode splitting [68, 69]. This strong coupling in a single quantum dot-semiconductor microcavity system was observed over 20 years ago [36]. In classical terms, the change of the spontaneous decay rate arises from back-action, which refers to the interaction of the atom with its own field. This field is the one that returns to the atom after being scattered by the surrounding environment. Conversely, in the quantum electrodynamics framework, the decay rate is driven by vacuum

field fluctuations, which depend on the characteristics of the environment, which is relevant in the context of the QD in a photonic cavity and experimental results in the next chapters represent the data in the weak coupling regime.

1.5.4.1 Identification of excitonic complexes in QDs

The correct identification of excitonic complexes in standard µPL spectra can be achieved using several methods. The emission signal from a QD (which is a consequence of the system's relaxation from a higher energy level to a lower one) can be analyzed in terms of polarization, time, or energy. Experimental data, such as binding energies, can be compared with theoretical models. External perturbations can be introduced into the QD system by varying the excitation power, magnetic field, electric field, or strain. Additionally, interactions with phonons can be studied through temperature changes, and excitonic states can be selectively excited (e.g., p-shell excitation, resonant excitation). Moreover, excitonic complexes can be analyzed using autocorrelation and cross-correlation techniques. Together, these methods, briefly summarized in Tab. 1.5, provide a comprehensive approach to the identification of excitonic complexes.

Method	Description	References
Polarization	Resolving the signal based on its polarization allows to measure fine structure splitting of an exciton and biexciton (typically absent in basic trions, observable for higher excitonic complexes).	[70, 71]
Power	Dependence on exciation power of varies for excitonic complexes where typically, exciton has a linear, and biexciton quadratic dependance.	[71–73]
Magnetic field	Spin splitting in magnetic field in Voigt configuration is a clear criterium of whether an excitonic complex is neutral or charged.	[63, 74, 75]
Electric Field and charge injection	Biexcitons and other complex excitonic may show a different rate of energy shift compared to neutral excitons, due to different polarizability and permanent dipole moment.	[76]
Linewidth ratio and line jitter	The emission linewidths of excitonic complexes confined within quantum dots reflect their interaction with a fluctuating charge environment caused by defects (spectral diffusion). Analyzing fluctuations in spectral line positions to understand environmental interactions.	[77, 78]
Autocorrelation and cross-correlation	Measuring the temporal correlation of emitted photons allows to identify cascaded emissions distingiusing trions, and exciton-biexciton cascades (asymmetric antibunching, bunching).	[79, 80]
TR PL	Bright and dark exciton dynamics can cause bi-exponential decay for excitons due to spin flip, with mono-exponential decay for trions.	[81]
Temperature	Single-dot carrier dynamics can be reservoir-dominated and change activation energies for particular complexes.	[71, 82]
Model	Using theoretical models to compare experimental eg. binding energies with predicted values.	[46, 75, 83, 84]
State excitation	Exciting specific energy states (e.g., p-shell) to selectively populate particular excitonic complexes.	[84]
Optical gate effect	Resonance fluorescence can be quenched by Coulomb blockade by tunneling of a carrier from a structural deep level, the optical gate with weak non-resonant laser can suppresses Coulomb blockade, switching back the QD into a neutral state, distinguishing trions and excitons.	[85]

TABLE 1.5: Selected methods used for the identification of excitonic complexes and their brief descriptions with references.

1.5.4.2 Excitons in magnetic field

As discussed previously, for the development of QD-based qPICs, the identification of emission lines in terms of involved excitonic complexes is highly useful. Part of the research outside of the scope of this thesis was devoted specifically to this identification aspect and magneto-optical spectroscopy (additionally providing the means for the reduction of fine-structure splitting), with results described in two works [86, 87]. The magnetic field is an especially useful tool in the study and identification of the excitonic complexes because bound excitons in QDs have a non-zero total magnetic momentum. In structures with reduced dimensionality, the interaction with magnetic fields is enhanced compared to bulk semiconductors or quantum wells because of the localized wavefunctions of carriers on a relatively small lattice size and reduced inhomogeneities [63]. The external magnetic field causes the diamagnetic shift because a charged particle in an external magnetic field will rotate at cyclotron frequency. This rotational motion generates an additional effective field that interacts with the external magnetic field. Since the cyclotron motion is induced by the external field, the diamagnetic shift is a second-order effect that only becomes significant at stronger fields. Consequently, all states tend to shift toward higher energies in the presence of high magnetic fields; this shift is typically a quadratic function of an applied magnetic field, where the Zeeman splitting is linear. The energy evolution of an excitonic complex in a magnetic field can be approximated by:

$$E(B) = E(0) + \frac{(g_e \pm g_h)\mu_B B}{2} + \gamma B^2 \tag{1.10}$$

Where $E(0)$ is the transition energy in zero magnetic field, γ is the diamagnetic coefficient, g_e (g_h) is the electron(hole) g-factor, and μ_B is the Bohr magneton. In the case of trions, the emission line splits into a quadruplet of energy levels due to the Zeeman splitting of both the initial and final states into doublets. The four resulting lines should exhibit identical intensities, attributed to the mixing of states induced by the applied magnetic field. These transitions are linearly polarized, with the polarization planes of the two "inner" and two "outer" pairs being orthogonal to each other [88, 89]. For neutral excitonic complexes, regardless of the fine structure splitting value, the exciton's dark and bright states remain separated by the electron-hole exchange interaction energy, maintaining qualitatively distinct behavior [63]. This analysis is limited since it does not provide information about the number of carriers forming exciton complexes, only the information that it is charged. Co-authored articles [86, 87] are describing magneto-optical experiments in Faraday and Voigt configurations, which allowed for the determination of in- and out-of-plane g-factors and corresponding diamagnetic shifts and identification of excitonic complexes (particularly trions) in InAs/InP quantum dots. This identification was based on a polarization-resolved μPL in high magnetic fields. For InAs/InP asymmetric quantum dots, conditions were determined for vanishing fine-structure splitting and possible generation of highly entangled photon pairs, which are crucial for

advanced protocols in qPICs.

1.5.5 Quantum light source

In the KLM scheme, information is encoded in the quantum state of photons. A single photon can act as a qubit, where the quantum information is represented in different degrees of freedom, such as the photon's polarization or path. The presence of a single photon in a particular mode (e.g., one out of two possible paths) corresponds to a superposition state of the qubit. To encode and manipulate quantum information accurately, each photon must be emitted reliably and one at a time. The ideal single-photon source possesses the following characteristics:

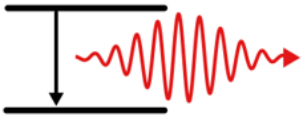

On-demand - an ideal single-photon source creates a photon deterministically when triggered by a laser or electrical pulse at a time arbitrarily chosen by the user (in contrast to probabilistic sources, which random nature prohibits generation on demand).

Pure - each emitted radiation field contains strict single photon with no multiphoton contribution as measured with the autocorrelation experiment. This can be characterized by the second-order intensity correlation function using a Hanbury Brown and Twiss experimental setup. The high single-photon purity increases the security of quantum communications [90] and minimizes errors in quantum computation and simulation [91–94].

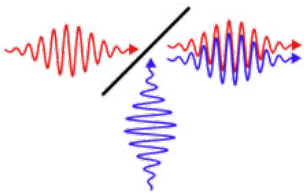

Indistinguishable - parameters of the photons packages such as wavelength, polarization, and temporal and spatial characteristics have to be the same. In addition, radiative decay must be the only decoherence process present. If any dephasing or additional decoherence processes occur, the emission linewidth will not be transform-limited. Often quantum technologies require effective photon-photon interaction, for example, for Bell-state measurement. Indistinguishability can be measured with the Hong-Ou-Mandel experiment [95].

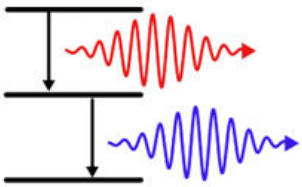

Entangled photon pairs - ideally the source should be able to generate entangled photon pairs since some applications require it (simulation algorithms and QKD). The entanglement from biexciton cascade can be prepared in the polarization or time basis or simultaneous in both forming hyper-entangled state [96]. The fidelity of an entangled-state preparation can be measured in a quantum tomography experiment. For example using strain tuning, 98% entanglement fidelity and 97% concurrence have been reported [97].

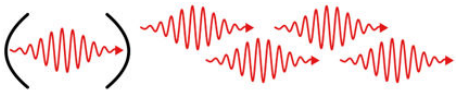

Brightness - the repetition rate should be as high as repetition rate of the excitation, constrained only by the temporal duration of the excitation and single-photon pulses. Due to the typically high refractive index of semiconductors, for the unstructured sample, the light extraction efficiency is typically limited to a few percent because of the total internal refraction at the material interface. Photon loss hinders the effectiveness of quantum dots as on-demand single-photon sources and can introduce errors in quantum computational algorithms [98, 99]. The brightness of a source can be determined by measuring the extraction efficiency (see Sect. 1.7.4).

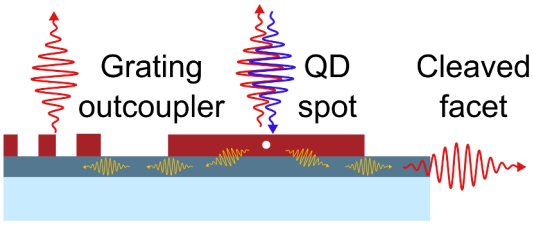

On-chip integrated source: single-photon sources integrated directly on chips would significantly enhance the capabilities of advanced applications and improve scalability. This integration enables miniaturization of photonic systems, leveraging the well-developed semiconductor industry for scalable, stable, and robust fabrication.

Characteristic	QDs	InAs/InP QDs
Deterministic	50 nm [100]	90 nm [101]
Pure ($g^{(2)}(0)$)	10^{-5} [102]	0.0032 [101]
Indistinguishable	99.6% [103]	84% [104]
Entangled	97.8% [97]	97.5% [105]
Bright (end-to-end)	57% [106]	1.13% [104]
Integrated	On-chip HOM [107]	Large-scale tunable QDs [108]

TABLE 1.6: Comparison of key characteristics of various QDs and InAs/InP QDs. The values provided for InAs/InP quantum dots include a high degree of purity, as mentioned in recent studies. All values in the table are approximations. Entanglement value is given for the InAsP quantum dot in an InP photonic nanowire waveguide.

1.5.5.1 Autocorrelation

In the context of single-photon sources and experimental results in subsequent chapters, especially important is the Hanbury-Brown and Twiss (HBT) experiment, which is used to measure the second-order correlation function $g^{(2)}(\tau)$ and to determine the value of correlated events at zero time delay ($g^{(2)}(0)$). Actually, the measurement results give insight into the single-photon emission purity of the source and not to the purity of the Fock state (e.g. Fock state F(2) is pure but not single-photon). Experimentally, two photodetectors are positioned symmetrically around a 50:50 beam splitter to independently measure photon counts and record the relative arrival times of photons at the two detectors. If the radiation field is statistically stationary and consists of only a single mode, then ($g^{(2)}(\tau)$) can be written as:

$$g^{(2)}(\tau) = \frac{\langle \hat{a}^\dagger(t)\hat{a}^\dagger(t+\tau)\hat{a}(t+\tau)\hat{a}(t)\rangle}{\langle \hat{a}^\dagger(t)\hat{a}(t)\rangle^2} \tag{1.11}$$

where $\hat{a}, \hat{a}^\dagger(t)$ are photon creation and annihilation operators, respectively, the τ is the time delay. Physically, $g^{(2)}(\tau)$ measures the probability of finding a photon pair with the time separation of τ.

Contrary to the first-order correlation function, the second-order coherence allows for differentiation and characterization of different light field types. If we take the number state (Fock state $\langle n|$) with a defined number of photons, $n = 1$ for a single photon source the $g^{(2)}(0)$ is given by:

$$g^{(2)}(0) = \frac{\langle n|\hat{a}^\dagger\hat{a}^\dagger\hat{a}\hat{a}|n\rangle}{\langle n|\hat{a}^\dagger\hat{a}|n\rangle^2} = 1 - \frac{1}{n} \tag{1.12}$$

This gives for $n = 1$, $g^{(2)}(0) = 0$ and for a laser with large n, $g^{(2)}(0) = 1$

With this autocorrelation function, the sources of light in HBT experiment can be classified into four categories:

Single-photon source	Quantum emitter	Coherent	Thermal	Superbunching
$g^{(2)}(0) < 0.5$	$g^{(2)}(0) < 1$	$g^{(2)}(0) = 1$	$2 \geq g^{(2)}(0) > 1$	$g^{(2)}(0) > 2$

TABLE 1.7: Comparison of different photon statistics.

In the context of the results shown in Chapt. 3 and 4, it is important to note that, typically in cavity coupled systems, there is a trade-off between higher efficiency and single-photon purity. In addition, the second-order correlation function is limited to assess only multiphoton probability and lifetime. It does not provide additional information into the simultaneous insight in source and cavity background emission photon statistics, which can be achieved by measuring the third-order correlation function, allowing for further optimization of the source in a cavity and to study cavity QED. It should also be noted that to demonstrate a pure single-photon state,

without large vacuum state contribution, $g^{(2)}(0)$ should be 0 or a negative Wigner function should be measured [109].

1.5.6 Photonic cavity

Optical cavities play a crucial role in altering the emission characteristics of any light source in the sense of its recombination rate, polarization and directionality; this interaction between the quantum emitter and a reflective cavity is studied in the field of cavity quantum electrodynamics. This interaction is used to achieve brighter and more indistinguishable single-photon sources [103, 110]. Photonic crystals are periodic structures that can interact with light in a way similar to an electron interaction in a crystal. If in this lattice we introduce a point defect or misalignment, it can confine the light, resulting in the formation of a photonic crystal cavity (PhCC). They can form a cavity via Bragg scattering (in the longitudinal direction) and total internal reflection (in both transverse directions).There are many different types of PhCCs and photonic structures which are presented in Tab. 1.8. Photonic crystal cavities provide a means to change the spontaneous emission rate of quantum systems positioned in the defect region. By tailoring the physical characteristics of the cavity, the local density of states (DOS) at the quantum system's emission wavelength λ_0 can be either enhanced or suppressed relative to the DOS in free space. The local DOS at λ_0 is determined by the cavity's capacity to store energy at the emission wavelength λ_0. Consequently, a higher quality factor, defined as $Q = \omega_0/\Delta\omega$, leads to a greater DOS. For a sufficiently large cavity, the density of states can be approximated as:

$$\rho = \frac{1}{\omega_0}\frac{DQ}{V} \tag{1.13}$$

Here, V represents the cavity's volume, while D denotes the mode degeneracy, which refers to the number of cavity modes sharing the same frequency. Taking into account that free-space of states is:

$$\rho_0 = \frac{1}{\omega_0}\frac{8\pi}{\lambda_0^3} \tag{1.14}$$

after combining the Eq. 1.13 and Eq. 1.14, the spontaneous decay rate enhancement is determined by:

$$K = \frac{\rho}{\rho_0} = \frac{D}{8\pi}Q\frac{\lambda_0^3}{V} \tag{1.15}$$

a significant enhancement relies on a compact cavity volume and a high Q-factor, other factors influencing cavity enhancement with an emitter are discussed in the next section. For this thesis, three types of cavities: H0, H1, and 1D waveguide linear cavity were fabricated, but for a comparison, an additional type of cavities is presented in Tab. 1.8.

Cavity type	Advantages	Design
H0	Small mode volume, higher light-matter interaction	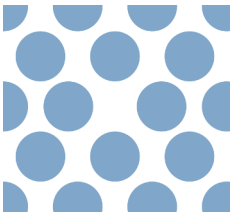
H1	High Q-factor, sustains two orthogonal fundamental cavity modes that are degenerate	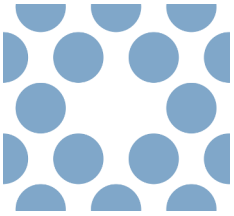
L3	Extended mode volume, better fields overlap, support directional emission	
Nanobeam (linear)	Directional, ease of integration in PIC	
Bowtie	Extreme field enhancements, high Purcell factors	
Micropillar	Vertical emission of light, coupling to external optical systems	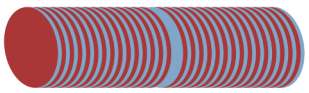
Microdisk	Supports Whispering-Gallery Modes	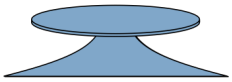

TABLE 1.8: A comparison of different cavity types, their advantages, and their design scheme.

1.5.6.1 Purcell Effect

The spontaneous emission rate of light sources is modified by their surroundings; especially, the spontaneous emission rate of the source dipole can be controlled by cavity design and exact positioning inside to match with the field maximum of the cavity mode. The increased local density of optical states of the photonic structure results in inhibited or enhanced emission rate. This relation is given by the Purcell factor:

$$F_p = \frac{3}{4\pi^2}\left(\frac{\lambda}{n}\right)^3 \frac{|d \cdot E_0|}{|d| \cdot |E_0|}\left(\frac{Q}{V}\right) \tag{1.16}$$

where λ is the wavelength, n is the refractive index of the material, Q is the quality factor of the cavity, and V is its mode volume, d is the dipole and E_0 is the electric field mode. As seen from the equation 1.16, to maximize the Purcell factor for a particular wavelength and material with fixed n, the cavity should have a high value of Q and a small mode volume. From the fabrication standpoint, the emitter should be placed in the center of a cavity, and its dipole should be oriented parallel to the cavity - $\frac{|d \cdot E_0|}{|d| \cdot |E_0|} = 1$. Fabrication with nano-resolution, with e-beam lithography, allows for reducing the cavity dimensions and highly increasing Q. Eq. 1.16 is an ideal case when the cavity and emitter are in resonance; we observe enhanced emission. Since currently most of the QDs are grown nondeterministically, they have to be selected, and their resonance has to be fine-tuned either with temperature (see Fig. 5.14 for experimental results) or electric field with Stark Tuning [106, 111], improving their coherence even to their Fourier limit. Importantly, this lifetime reduction and improvement of the coherence can decrease the influence of phonons on dephasing and increase chip operation temperature. It can lead to improvement of the coherence can decrease the influence of photonic wires [112–117], micropillar cavities [4, 103, 118], photonic crystals [119–121], circular Bragg gratings [4, 101, 122–124], tunable cavities [106, 125] and hybrid structures [126, 127]. Alternatively, to improve the strength of the light-matter coupling, i.e. the ratio between the Q factor and the volume of the cavity mode, a cavity with extreme dielectric confinement can be used [128]. This modified photonic environment allows the realization of quantum communication [129–132], quantum teleportation [133], and as input of quantum states for photonic quantum computing [134, 135].

1.6 Photonic Integration Technologies

In the context of the PIC industry, there are four different integration approaches from which III-V qPIC can leverage expertise and fabrication techniques:

- III-V on InP integration - growing epitaxial layers of ternary or quaternary materials on a shared InP substrate, enabling the production of optoelectronic devices. This approach supports full monolithic integration of both passive and active components on a single platform [136].
- Silicon on insulator (SOI - monolithic silicon photonics) - serves as the ideal platform for conventional silicon photonics, where most optical functionalities are achieved through devices built from the silicon device layer. Additionally, selective area epitaxy of germanium is utilized for photodetection purposes.
- III-V heterogeneous integration - leverages silicon-based processing within a monolithic silicon photonics platform, while integrating III-V materials for active optical functionalities like gain, photodetection, and phase or amplitude modulation. A key advantage is the ability to integrate multiple epitaxial materials on a single PIC, all interconnected via a shared silicon waveguides [137].
- III-V epitaxial grow on silicon - integrating III-V materials with silicon through epitaxial growth, eliminates the need for III-V substrates and allows the use of existing 300 mm processing, testing, and packaging infrastructure. Albeit direct epitaxial growth of InAs/InP QDs on silicon is limited.

These integration approaches can be broadly categorized into heterogeneous and homogeneous.

- **Heterogeneous integration**: Integration of different types of components that may be manufactured using different technologies (e.g. SiN, SOI, InP) and assembled on the same system.
- **Homogeneous integration**: Integration of similar types of components that are fabricated using the same process technology and typically integrated on a single die.

Heterogeneous integration addresses the increasing cost and limitations of monolithic fabrication design employing a modular approach for complex designs. However, the proposed solution in the form of heterogeneous integration comes with its own set of challenges. Rather than simplifying the design process, it actually complicates it. Transitioning from a single monolithic system-level architecture reintroduces issues that have been effectively managed, such as thermal, electrical, and mechanical stresses. From the other perspective, the homogeneous integration typically follows Moore's law, while the heterogeneous integration allows for an accelerated growth of component count. Integration technologies can also be categorized based on dimensionality:

- **2D integration**: Traditional integration, where all components are placed on the same planar surface (single chip).
- **2.5D integration**: Components are placed side by side on an interposer, which acts as a high-bandwidth bridge between them.
- **3D integration**: Components are stacked vertically on top of each other and connected by vertical interconnects.

For more details on vertical integration see Chapt. 3 where the results of heterogeneous integration using direct bonding are described, and in Sect. 5.1 the process of heterogeneous integration using micro-transfer printing is detailed. The heterogeneous integration of the InP and SiN waveguides is provided in Sect. 5.2 and the homogeneous integration between InP and InP in 5.11.

1.6.1 Quantum photonic computing

Key aspects of quantum technology such as quantum communication, quantum sensing, quantum computing, and simulations can be realized with qPICs. Implementing a quantum simulator requires its physical implementation with a quantum mechanical platform that can be precisely controlled. There are already many proposed quantum emitters, building blocks, and material platforms for their integration, which are summarized in Table 1.9 and a conceptual illustration for a basic qPIC is presented in Fig. 1.6.

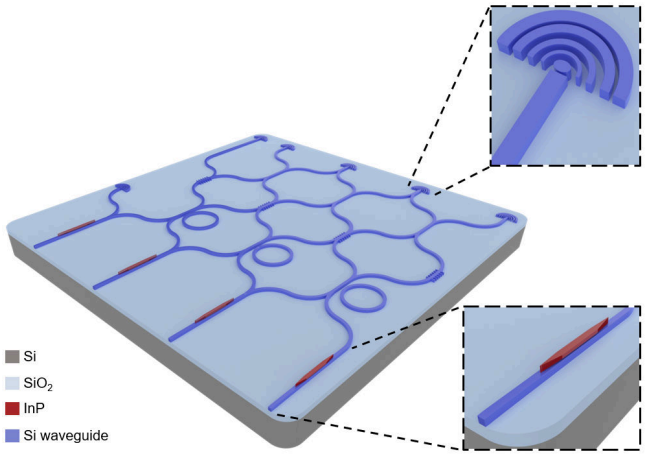

FIGURE 1.6: Illustration of a qPIC with a heterogeneously integrated QD emitter. The structure includes a silicon substrate (gray), a silica layer (light blue), and patterned silicon waveguides (blue) with InP (red) and InAs QDs. Enlarged views highlight single-photon source and outcoupler regions, while the silicon waveguide circuit demonstrates possible information processing using phase shifters, ring resonators, and directional couplers published in Ref. [22].

	Building block	Examplary platform
Quantum system	QD Atomic like defects Trapped ions Nanotubes Cavity arrays Electronic spins Superconducting circuits Nuclear spins SPDC	III-V semiconductors Diamonds 2D materials Rare earth ions Radiation induced defects Single molecules
Non-linar processes	Frequency converters Parametric down-conversion Four-wave mixing Squeezing	$LiNbO_3$, GaAs, Si SiN, AlN, SiO_2, SOI
Circuit elements	Mach-Zehnder Beam splitters MEMS Micro-cavieties Circulators Phase Shifters	Polymers III-V semiconductors Si, SOI, SiN, SiO_2 $BaTiO_3$, Ta_2O_5
Quantum memory	EIT, AFC (Off-) Raman ORCA / FLAME Spin (gradient) echo Photons, QDs Delay lines	Atomic vapour Rare-earth ions Diamond, SiC III-V semiconductors SiO_2, Si
Single photon detector	SPAD, APD SNSPD, TES	Si, InGaAs NbN, TiN, WS_2
Classical control	Laser light sources Electronic components Modulators Quantum cascade lasers	Si III-V semiconductors SiN TCOs

TABLE 1.9: Overview of selected building blocks and platforms for qPICs. Components required for qPICs are categorized into quantum emitters, non-linear processes, circuit elements, quantum memory, single photon detectors, and classical control. For each building block, exemplary platforms are provided. For more circuit elements see Tab. 1.10.

Of these quantum emitters, all have their own strengths and weaknesses. For many years, single-photon sources based on the spontaneous parametric down-conversion (SPDC) process in nonlinear optical materials have been widely used in photonic quantum applications [138–140]. This process allows for the simultaneous creation of photon pairs, enabling the generation of one photon to be confirmed by detecting the other. However, while SPDC sources are straightforward to operate, they are fundamentally probabilistic, which can pose challenges when attempting to scale to a larger number of photons. The advantage of III-V semiconductor QDs is their ability to generate photons with excellent quantum properties as described in Sect. 1.5.5 and given in Tab. 1.6. Crucially, the strength of QDs is the on-demand operation and the possibility of integration with other semiconductor platforms [1, 2]; their drawback is the very early stage of integration with photonic integrated circuits. To exploit the potential of this integration, it is necessary to identify technological solutions and material platforms with a special focus on scalability that can transfer these concepts from the proof-of-concept status [140, 141] to practical applications within the rapidly expanding quantum computing industry [142].

1.6.1.1 SOI and SiN

Several material platforms, such as III-V semiconductors or silicon, can be utilized to create a PIC. In this thesis, two samples are fabricated on SOI with Si waveguides and one on SiN material platform with SiN waveguides and in this section these material platforms comparison is given. Silicon photonics, which employs silicon-on-insulator (SOI) wafers [18] is one of the most promising and is the mature CMOS-compatible solution for optoelectronics. In free space, light behaves as an oscillating wave composed of electric and magnetic fields. Light can be confined within dielectric materials and guided through a waveguide which is the primary component of a PIC. In silicon photonics, this waveguide is a high-refractive-index crystalline silicon (n = 3.45) wire (Si layer of 220 nm is one of the industry standards) surrounded by a lower-refractive-index silicon oxide coating (n = 1.45). Silicon oxide acts as a buffer layer to prevent mode leakage into the silicon substrate; this buffer layer is typically 1 to 3 µm thick. This refractive-index contrast enables the optical mode to be tightly confined and guided within the silicon waveguide, connecting the various elements on the chip. Most optical waveguides used in communications are single-mode, meaning they support only one guided mode for each polarization (TM and TE). Additionally, silicon is transparent in the telecom C- and O-bands due to its bandgap of 1.12 eV (1107 nm). Typically, silicon waveguides have a relatively low loss (<2 dB/cm) for wavelengths up to 8 µm (limited by absorption in silicon, scattering losses from sidewall roughness, and mode confinement), although this can vary depending on factors such as waveguide design, fabrication quality, and surface roughness [143]. The SiN waveguide platform has a wider operation window extending into the visible and near-infrared ranges. The high mode confinement in the silicon layer allows for a high density of components [128] and low bending

losses at the 1.55 µm wavelength [144]. When comparing SOI platform with SiN, the lower index contrast of the SiN system compared to SOI makes it more challenging to create high-efficiency grating couplers for out-of-plane optical input/output. In SiN photonic waveguides, losses can be reduced by an order of magnitude [145] making it more suitable for creating, for example, delay lines in the Mach-Zehnder interferometer on chip. In addition, SiN is more suitable for fiber coupling as a result of the lower refractive index. It is important to note that the choice of the bright emitter and a platform with minimal losses is critical to preserve quantum information in a system due to the no-cloning theorem (see also Sect. 1.6.3 on QKD).

1.6.1.2 Building blocks of PICs

In the context of PICs, there are multiple elements that can be fabricated on-chip, to control the fundamental properties of light that include phase, amplitude, polarization, direction, and mode size, and Tab. 1.10 gives an overview of typically used building blocks (allowing to build complex systems) and their selected parameters. In the context of this thesis, the used components are: waveguides, grating couplers, edge couplers, and DBRs (ring resonators are on one of the samples but are not discussed here).

Component	Function	Parameters	Ref.
Waveguide	Medium for efficient on-chip transmission of optical signals	Loss of 0.1–0.43 dB/cm	[146, 147]
Waveguide crossing	Structure that enables signal paths to cross with minimal interference.	Insertion loss of 0.043 dB	[148]
Y-Splitter	Passive waveguide design that splits the incoming optical signal into two paths.	Loss of 0.03–0.2 dB and broad bandwidth > 300 nm	[149–152]
MZI	Interferometer which splits signal into two paths and recombines them.	Broadband (30 nm) and GHz-fast operation	[153]
Grating coupler	Fiber-to-planar waveguide coupler for outcoupling light.	Chip-to-fiber coupling efficiency of 99.2%	[154]
Edge coupler	Interface between optical fiber mode and waveguide modes.	Low-loss (< 2dB) and broadband (100 nm)	[155]
Spot-Size Converter	Allows direct coupling of waveguides, eliminating differences in mode size.	Coupling loss of 0.5 dB per connection	[156]
Modulators	Controls the amplitude, phase, and polarization state of a signal.	High-speed performance (25 Gb/s) with low insertion loss (3–6 dB)	[157, 158]
Ring Resonator	Closed-loop waveguide structure acting as a spectral filter.	Loss of 3-4 dB/cm, FSR - 16 nm, $Q = 2 \times 10^5$	[159]
DBR	Mirror formed by etching a periodic holes.	Reflectivity of 99 %	[160]

TABLE 1.10: Description of a selected Si photonic components and their parameters.

Additional components are arrayed waveguide gratings which disperse multiple

wavelengths into multiple, spatially separated output waveguides. Semiconductor optical amplifiers, optical isolators, polarization controllers, phase shifters, and photodiodes convert an optical signal into an electrical signal.

1.6.2 Light coupling and outcoupling

Although high-quality PIC can be achieved using standard CMOS fabrication tools, for single-photon detection the interface with the optical fiber remains the main source of loss. This is due to the significant difference in the mode size between the single-mode fiber (typically MFD of around 10 µm at 1550 nm) and the waveguides (the typical SOI single-mode waveguide is 0.5×0.3 μm^2 in size) on the photonic integrated circuits. In fiber outcoupling and packaging, various methods have been developed to couple the fiber and the on-chip waveguide. These methods can be broadly categorized on the basis of the orientation of the optical path of the couplers and mode adapters. The first category is end-coupling (also referred to as edge-coupling, in-plane coupling, and butt-coupling), where the optical axis of the input and output ports runs parallel to the waveguide and has to be aligned with sub-micron precision. The mentioned difference between the fiber and waveguide mode sizes can cause up to a 30 dB coupling loss if the fiber is directly edge-coupled to the waveguide without any mode-matching structures. To reduce this loss in photonic integrated circuits, edge couplers are employed. A common edge coupler design is the inverted taper, which helps convert the mode by expanding the optical mode size to better match small-core fibers. To further enhance coupling efficiency, lensed or tapered fibers can be used to focus the light into a smaller mode, although these fibers are more expensive than standard single-mode fibers. Moreover, the precise dicing and polishing processes add complexity and cost to the manufacturing.

The second category is vertical coupling (also known as off-plane coupling), where the optical axis of the fiber is at a slight angle perpendicular to the grating coupler. They are based on gratings with a sub-micron periodic structure. This structure creates conditions for coherent interference, allowing the injected beam to be diffractively coupled into the waveguide [161, 162] and example of a simulated grating structure is shown in Fig. 1.7.

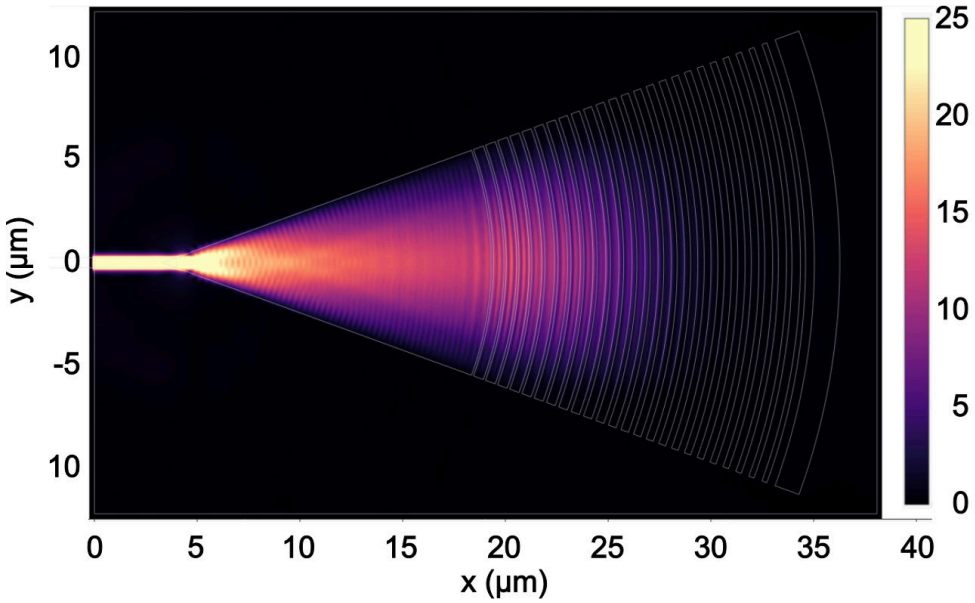

FIGURE 1.7: FDTD simulation of an examplary focusing apodized grating coupler electric field distribution (intensity scale on the right) in SOI (BOX layer thickness is 2 µm, device layer thickness is 0.220 µm, with a SiO_2 cladding of 0.780 µm). Grating coupler etch depth was set to 70 nm, the taper opening angle was set to 40 deg. with a taper length of 16 µm and 25 number of grating periods and apodization parameter of 0.031 nm. The wavelength range for this simulation was 1520-1580 nm.

Aspect	Grating Couplers	Edge Couplers (and V-groove)
Size	Compact	Larger footprint
Testing Capability	High	Low
R&D effort	Medium	Very Low (High)
Scalability	High	Low
Coupling Position	Flexible	Fixed
Coupling Efficiency	Relatively low (< 2 dB)	High
Bandwidth	Limited	Broad
Wavelength Sensitivity	High	Low
Polarization dependence	High	Low
Alignment Requirements	Medium	Medium

TABLE 1.11: Comparison of Grating Couplers and Edge Couplers.

While both approaches have their advantages and drawbacks for qPIC, where the highest coupling efficiency is required, the horizontal die-level edge coupling is the optimal solution with the best device performance. In the R&D stage of development, the vertical coupling has the potential to be more optimal for testing multiple designs. In this work, those two approaches (edge and grating coupling) have been used, characterized, and compared in Chapt. 3. It is important to note that for this sample, the interface between the chip and the single-mode fiber was mediated by a microscope objective in the optical detection path. This allowed for access to the sample inside the cryostat with the sample cooled to 5K.

1.6.2.1 Coupling between waveguides

When the photonic chip is composed of different material system waveguides (InP, SiN, Si), the coupling between them poses a significant challenge, especially in their mode matching, where mode mismatch causes significant losses in the system. The solution to this problem is specially designed couplers between waveguides, typically realized by in-plane or vertical evanescent coupling. In the Fig. 1.8 there are shown exemplary simulation results of the evanescent coupling between SiN/Si waveguides. The transmission loss is below 0.04 dBm (the top SiN waveguide has a larger volume, so its average power density is lower, and to calculate loss, the intensity has to be integrated in cross-section). This optimized example requires at least four layers for fabrication. Since in the processing, every step has to be optimized to produce the desired structure, this complex design is more suited for optimization and not for prototyping. For the fabrication of structures in this thesis, a more efficient approach (in terms of fabrication steps) was used and described in Chapt. 3.

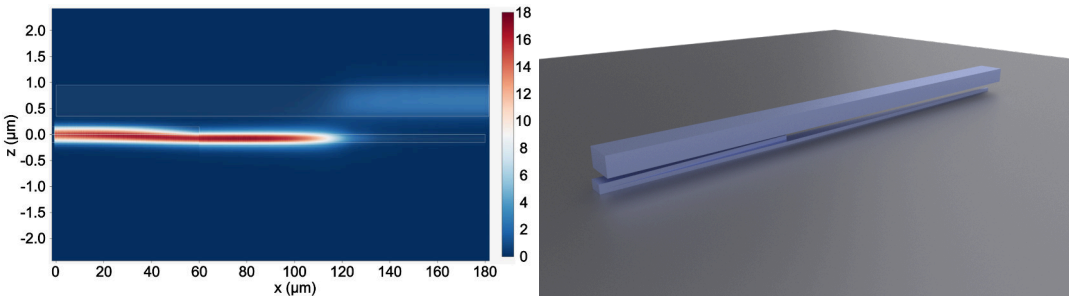

(a) SiN/Si (b) 3D view of a SiN/Si coupler

FIGURE 1.8: Simulation results of the Poyting vector field (its relative magnitude is represented as a color scale) in x and z directions of the structure of an exemplary evanescent coupling between Si waveguide with width of 0.5 µm and height of 0.3 µm to SiN waveguide of 1.0 µm width and 0.6 µm height for 1550 nm. The full confinement of light in Si WG (bottom WG) and its gradually coupling into the SiN WG is visible. In the 3D view there are visible two Si tapers at the bottom and the SiN waveguide at the top.

1.6.2.2 Etendue

In every optical system, etendue is a measure of the light occupancy of space both spatially and angularly. This metric is crucial to determine the efficiency with which an optical system can transmit light. It is mathematically expressed as the product of the area of a light source or aperture and the solid angle that the emitted light covers:

$$\epsilon = \pi n^2 \sin^2 \Omega \tag{1.17}$$

where ϵ is the etendue, n is the refractive index, A is the area of the source, and Ω is the cone angle of light from a source. Importantly, the law of conservation of etendue states that it remains constant in an ideal optical system, and the component with the smallest etendue controls the overall system throughput.

However, in real-world applications, etendue can increase due to factors such as diffusion, scattering, aberrations, and diffraction, which arise from imperfections in optical elements and are dictated by thermodynamic laws. When creating free-space configurations and photonic components on chips, it is essential to consider the light transmission between various elements, and with careful management, it ensures that the optical system operates efficiently without loss of throughput. In the work [22] the relation between the etendue of the waveguide and the single-mode fiber collecting the signal is discussed in more details, as it is crucial to determine the on-chip coupling and efficiency of the system.

1.6.3 Quantum key distribution

In the context of the development of the all-fiber C-band single-photon source for QKD (see Sect 4), if fault-tolerant quantum computers, as described in Sect. 1.1 of large scale, are realized in the future, they will have the capability, through Shor's algorithm [163], to compromise the majority of public-key cryptographic systems that our digital networks rely on. Although such quantum computers are not currently available, the current security of communication is already compromised with potential risk, known as the store-now-decrypt-later scenario. Malicious entities could intercept and store encrypted data now with the intention of decryption once quantum computing technology advances sufficiently. For secure communication in the literature, a lot of attention is put on the quantum key distribution [164–169] which is one of the core functionalities of the quantum Internet, and over the past decade, quantum information technology has made great progress, from the proof of concept stage to multiple QKD metropolitan [170–173] and satellite [174] QKD networks.

Limitations

In this section are presented limitations of the development of the QKD system. While the no-cloning theorem is often cited in the scientific literature as a key to solve security issues through QKD, it must be admitted that every technology has

drawbacks. This is particularly true for QKD, as currently it is a point-to-point communication technology which struggles to scale up for modern communication networks. It is also still susceptible to man-in-the-middle attacks (eavesdropping), intercept/resend, photon number splitting, and blinding receivers. These networks are also vulnerable to traditional cybersecurity threats. Furthermore, the United States National Security Agency does not view QKD as a viable security measure for national security information systems.

Despite its limitations, QKD shows the potential to create unbreakable encryption, particularly by generating unlimited random keys for One-Time Pad encryption. This makes it suitable for niche applications, such as secure point-to-point communications, data transfer, and for specialized applications like encrypted voice communication in specific areas. Although multiple advances, the loss in optical fiber continues to impose a limitation on long-distance quantum communication. Given the low attenuation of optical fibers at telecom wavelengths, typically around 0.2 dB/km, it is straightforward to calculate the transmission loss over optical fiber.

$$T(x) = 10^{\frac{-attenuation(\frac{dBm}{km})}{10km}x} \tag{1.18}$$

This limits the maximum transmission channels to a few hundred kilometers before the main source of errors is noise [175] and repeaters are necessary. However, the no-cloning theorem also prevents single-photon amplification. Consequently, classical repeaters would not work. This drives the development of quantum repeaters, an essential component of efficient quantum memory that is still in development [176–178]. An alternative to overcome long-distance limitations is to use multiple trusted nodes [179, 180]. This transmission limitation also motivates the development of sources with high extraction efficiency and a high repetition rate, resulting in an overall increase in brightness or count rate generation. Both aspects can be engineered with the use of a photonic environment, which directs the emission into the collection optics and also increases the spontaneous generation rate due to the Purcell effect.

Other limitations are imposed by the ease of use, cost, and size of the system - currently commercial QKD boxes are too large and expensive to be incorporated into industrial or consumer-grade electronics, limiting their use to institutions gaining from secure communication, such as banks and government organizations. This limitation arises from the difficulties in integrating the required optical components, such as the single-photon source, waveguides, single-photon detector with its cooling hardware, and processing electronics. This aspect also motivates directions of research in this thesis, namely the development of the all-fiber plug-and-play source, which allows for easy operation (setup described in Sect. 1.7.3). The integration with a compact and closed-cycle cryocooler is in the direction of a large reduction of the cost and size of the system.

1.7 Experimental setups

1.7.1 Microphotolumienscence

For the characterization of samples in this thesis, the most utilized experimental technique is the microphotoluminescence (µPL) experiment, which is typically used to study properties of single semiconductor nanostructures, such as QDs. The experiment involves a laser source to excite a QD, with the laser focused to a spot size of about a few µm spatial extent using a microscope objective. Thus, a high spatial resolution of the experiment enables a detailed study of microstructures (mesas, waveguides, grating couplers), unlike conventional macro-PL spectroscopy, which uses a lens to focus a laser beam over a significantly larger excitation area than with the microscope objective. Therefore, macro-PL serves only for studies of nanostructure ensembles. Initially, a laser with a photon energy greater than the band gap energy of the studied material excites electrons from the valence band to the conduction band. The excited electrons then relax to the bottom of the conduction band by emitting phonons (dynamics of the specific processes are described in more detail in Sect. 1.5.4 and illustrated in Fig. 1.5).

Typically, the experimental setup is composed of three main sections: excitation, imaging, and detection. All paths merge at the central point of the setup, which is the microscope objective and cryostat with a sample inside. The simplified (mirrors, couplers, and some fibers are omitted) visualization of an experimental setup is shown in Fig. 1.9. For the experiments, three types of excitation sources were used: the continuous wave lasers (Coherent CUBE) emitting at 660 nm and 787 nm, and a pulsed laser (PicoQuant LDH-D-C-810) with the central pulse photon wavelength at 810 nm. The lasers were fiber-coupled to a single-mode fiber (unless stated otherwise) to increase collimated beam quality (at the cost of available excitation power) by filtering out higher-order spatial modes, leaving only the fundamental mode, resulting in a Gaussian-like intensity profile. In a free-space setup, laser beams were outcoupled with a reflective collimator, which is based on a parabolic mirror, and it allows for alignment-free co-collimated beams of lasers at different wavelengths. It is important to note that when designing an optical system, long-pass filters and dichroic mirrors are designed for use at various angles (typically 45°, 90°) of incidence. The second section of the µPL setup is the sample's surface imaging part. It allows a live view of the microstructure during the experiment and monitors the excitation/detection spot at the sample's surface (e.g. the same part of the InP waveguide). Custom software was developed for a precise auto-alignment of the structure; more details are given in Sect. 1.7.5. The photons emitted by the sample are collected by the microscope objective. In the experiments, multiple microscope objectives were used, all from the Mitutoyo company. The objectives were apochromatic in the near-infrared spectral range, infinity corrected, and having a long working distance (M Plan Apo NIR series) with magnification ranging from 5x to 100x. The objectives provided a maximum spatial resolution for signal detection of

1.35 µm for the 1550 nm photon wavelength and a resolution of 0.73 µm for sample imaging at the 830 nm photon wavelength. Subsequently, the collected photons were transmitted through two longpass edge spectral filters. The first filter, at 805 nm, reflected laser light to the sample. The second filter, at 1200 nm, reflected the 830 nm monochromatic light to the imaging section. Finally, collected photons were coupled to a single-mode fiber. A lens was used for the coupling, and the lens parameters were matched to the numerical aperture (0.65) of the microscope objective (see also Sect. 1.6.2.2). The fiber-coupled photons were then directed to the tunable and narrow-band spectral filter (0.4 nm FWHM bandwidth), which allows the transmission of a specific wavelength controlled by a motorized actuator. Then the signal was guided to the telecom optimized (quantum efficiency about 90%) SNSPD where the signal intensity could be measured.

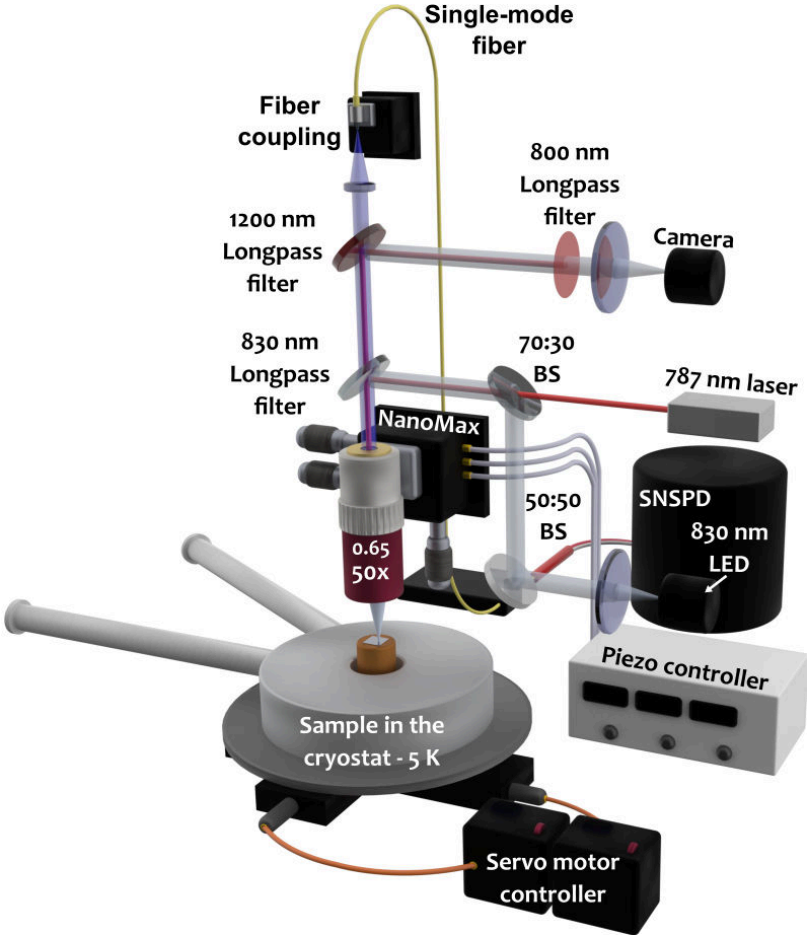

FIGURE 1.9: Visualization of the µPL experimental setup with its main components in a configuration allowing to perform autocorrelation experiment. Published in ref. [181].

1.7.2 Orthogonal configuration

Typically, PICs with waveguides ending at the edge of a chip are investigated in free space using a single-mode fiber ending with a micrometer-size lens. The lens matches the MFD of a photonic waveguide MFD (as described in Sect. 1.6.2). These

fibers, with a small focal length, are routinely precisely aligned in close proximity to a chip's edge to achieve the best coupling efficiency. However, PICs with QDs as photon emitters require cooling to cryogenic temperatures to achieve the desired QD emission. Therefore, these structures are typically placed in bulky cryostat environments that limit the available space around the PIC chip to include fiber setups. With the PIC chips studied in this thesis, there was no option to install fibers inside the cryostat environment. To solve the problem of photons outcoupling off the chip' edge with simultaneous excitation in the normal direction to the chip surface, two long-working-distance microscope objectives were used in the orthogonal configuration. This allowed a precise orientation of both objectives placed outside of a cryostat for the most efficient excitation and light collection.

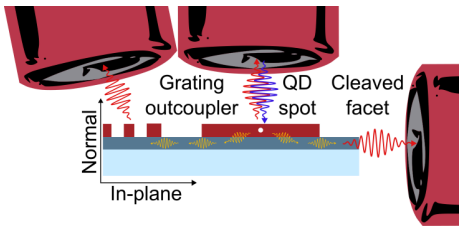

FIGURE 1.10: Configuration with 3 microscope objectives [22].

With the presented optical setup, the emission properties of the PIC chip can be assessed in several excitation/detection configurations. The optical detection can be set to either along the normal to a waveguide, from the outcoupler, or the cleaved edge of the Si waveguide as illustrated in Fig. 1.10 and Fig. 1.11. The chip was maintained at 5 K in a helium flow cryostat system (Janis ST-500) originally designed for cryogenic microscopy. To investigate general optical response of the chip, a continuous wave, λ = 787 nm laser line was used to excite the QDs in the chip. The QDs provides photons to the chip interior. To evaluate the efficiency of the components in the device, QDs were excited using a pulsed laser (λ = 805 nm, 80 MHz). Photons generated by a QD were transmitted to the chip and collected from three different directions, each requiring its own detection paths. For photon detection from the Si waveguide at the cleaved edge of the chip, two microscope objectives were employed in the perpendicular orientation. One of the objective was used to excite a QD, the second objective was facing the chip edge. This objective had a 100x magnification and a numerical aperture (NA) of 0.7. Collected photons were filtered with a tunable fiber-based narrowband spectral filter, offering a spectral resolution of 100 µeV and a spatial resolution of 0.6 µm. For photons detection in the in the normal direction a 20x magnificaton objective was employed with NA = 0.4.

Power-dependent micro-photoluminescence (µPL) intensity from the QD in the waveguide was measured using an InGaAs 1D linear chip (Princeton Instruments) for pulsed excitation and an SSPD for continuous wave excitation. The SNSPD detection system (Scontel) offered a temporal resolution of 50 ps and a dark count rate below 100 cps.

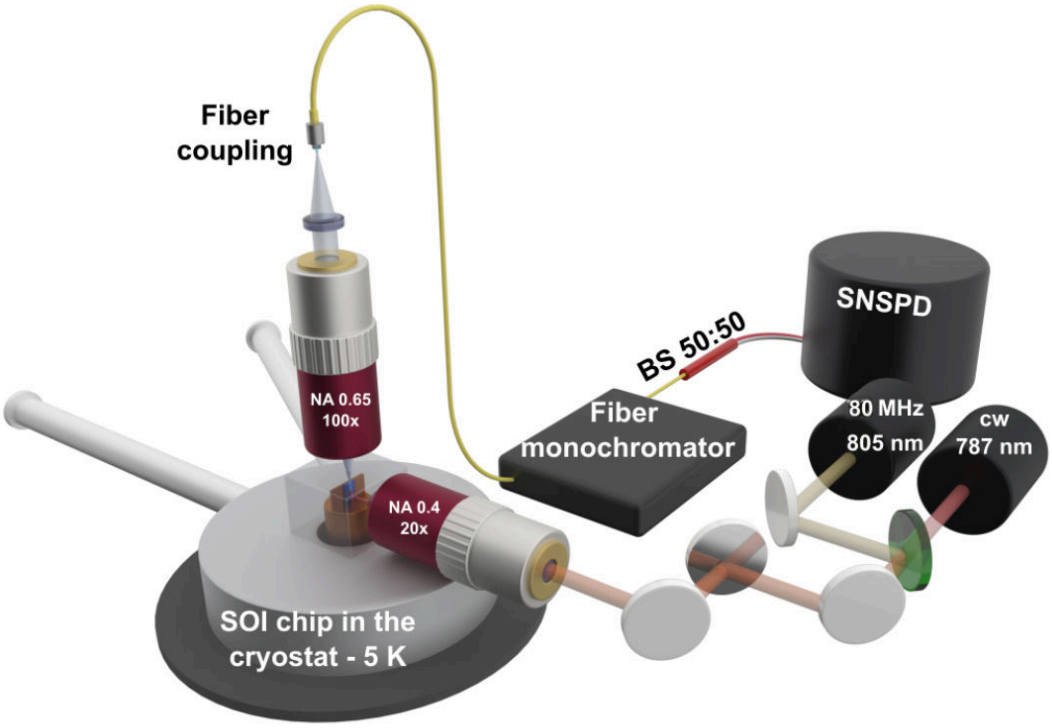

FIGURE 1.11: Simplified orthogonal arrangement of experimental setup used for evaluation of extraction efficiency from the on-chip coupled QD emission and for measurement of the autocorrelation [22].

1.7.3 All-fiber setup

This section describes an experimental setup used for the characterization of the sample that was deterministically integrated with a single mode fiber with experimental results described in Chapt. 4. In the context of QKD, an all-fiber setup refers to a system in which all the components used for transmitting and manipulating light are based on optical fibers. This contrasts with systems that use free-space optical components (objectives, mirrors, beamsplitters), where quantum signals are transmitted through the air or vacuum. In terms of experimental setup, one of the advantages of this integration is that the sample can be placed in a more compact closed-cycle cryocooler without the need of any bulky free-space optics, which require adjustment. Additionally, since the position of a sample is fixed, the setup does not require vibration damping systems. In general, this reduces the cost and complexity of the system, bringing it to more real-world applications. One of the challenges is that the unavoidable fiber connections introduce not only losses but also unwanted backreflections in the system, which are particularly problematic for the photon statistics measurements. This without filtration causes an increase in the background and unwanted resonances. Reduction of this stray light and noise in part can be achieved with the use of filters on the excitation side and with the use of

angled physical contact (APC) fiber (Smf28) connectors instead of physical contact (PC) connectors.

The experimental setup schematic is shown in Fig. 1.12 as well as the bird-eye view of the localization of the sample and the excitation and detection nodes inside the University building. The signal from the sample mounted in a cryocooler is guided outside of the laboratory and connected to the excitation and detection node. Into this fiber, the pump laser is guided with a 50:50 fiber beam-splitter. The signal is then dispersed on the spectral filter, and autocorrelation is measured on superconducting single-photon detectors using an additional 50:50 fiber beamsplitter.

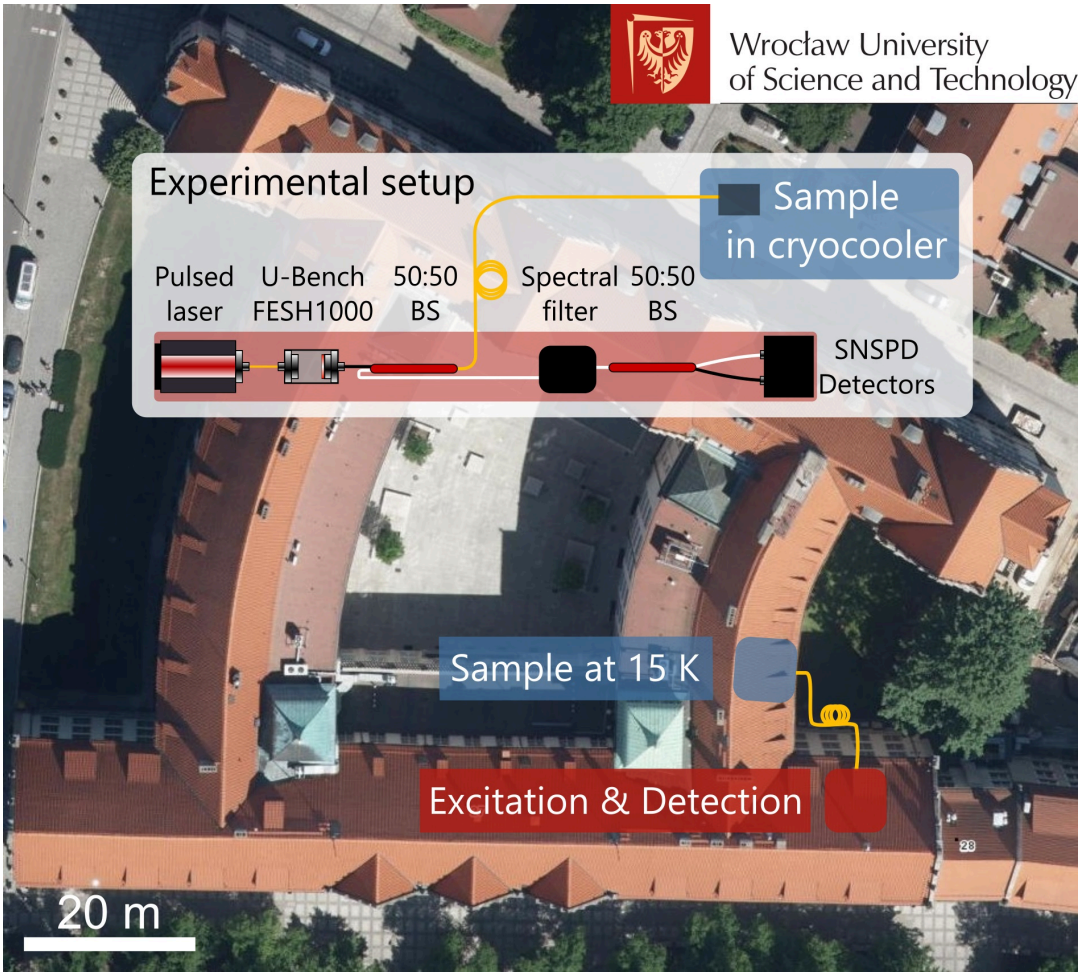

FIGURE 1.12: All-fiber experimental setup with an integrated single-photon source. In the photo background there is the location of the two laboratory nodes used for the experiment. In the inset there is a schematic of the all-fiber path from the excitation laser to the source and to the detectors.

The components used in the experiments with the all-fiber setup are presented in Tab. 1.12.

Component	Company, model	Parameters
Closed-cycle cryocooler	CTI-Cryogenics, 22	15K, dimensions of 30x40x25 cm
Pulsed laser	PicoQuant, LDH-D-C-810	805 nm, fiber-coupled repetition up to 80 MHz, 50 ps-long pulses
Continuous-wave laser	Coherent, CUBE	787 nm, fiber-coupled
Monochromator	Princeton Instruments	0.5 m focal length
Detector	Princtone Instruments, PyLoN-IR	InGaAs, InGaAs 1D linear chip
SNSPD detectors	Scontel	QE 90%, dark counts 10 Hz, time jitter (<35 ps), temporal resolution 80 ps
Shortpass filter	Thorlabs, FESH1000	1000 nm cutoff, fiber-to-fiber U-Bench
Fiber Optic Coupler	Thorlabs, TW1550R5F1	50:50 Split, 1550 ± 100 nm, FC/PC
SM fiber	N/A	SMF-28-J9, 30 m stainless steel shielded
Cryocooler connection	Custom made	SM-SM
Compressor	CTI-Cryogenics, 8200	Water-cooled, connected to cryocooler
Turbo pump	Pfeiffer Vacuum, HiCube 80 Eco	Connected to cryocooler
Fiber optical filter	WL Photonics	Polarization-insensitive electric tunable, 0.4 nm FWHM bandwidth, 1520-1580 nm tuning range, centered at 1550 nm

TABLE 1.12: Components used in the characterization of the sample in all-fiber configuration.

As a note, a tunable optical filter is built based on free-space optics using a diffraction grating to produce a band-pass transmission, with outcoupled light from a collimator to a grating put in a plug-and-play box. On a similar note, an optical filter mounted onto a plug-and-play u-bench is also considered part of an all-fiber setup since it does not require any alignment after setting up, ensuring that all the experimental configuration is considered all-fiber.

1.7.4 Extraction efficiency

In the context of QDs, the extraction efficiency asserts the ability of the structure to guide photons into the collection optics. This is governed by many factors such as

refractive index contrast, optical cavity effects, geometry and positioning, surface, and interface quality. In the literature, there is no clear definition of extraction efficiency from a quantum dot. First, there is no concrete definition of which part of the light should be taken into account when calculating the extraction efficiency. It can account for only one discrete transition or multiple emission lines caused by the excitation pulse. It is important to note that the measured count rates on the detectors should be corrected for the multiphoton events, which can be accurately measured in the autocorrelation measurement. Secondly, there is an assumption that the internal quantum efficiency of a source is 100%, which typically gives a lower limit for the extraction efficiency. In Fig. 1.13 multiple aspects of the extraction efficiency definitions are presented.

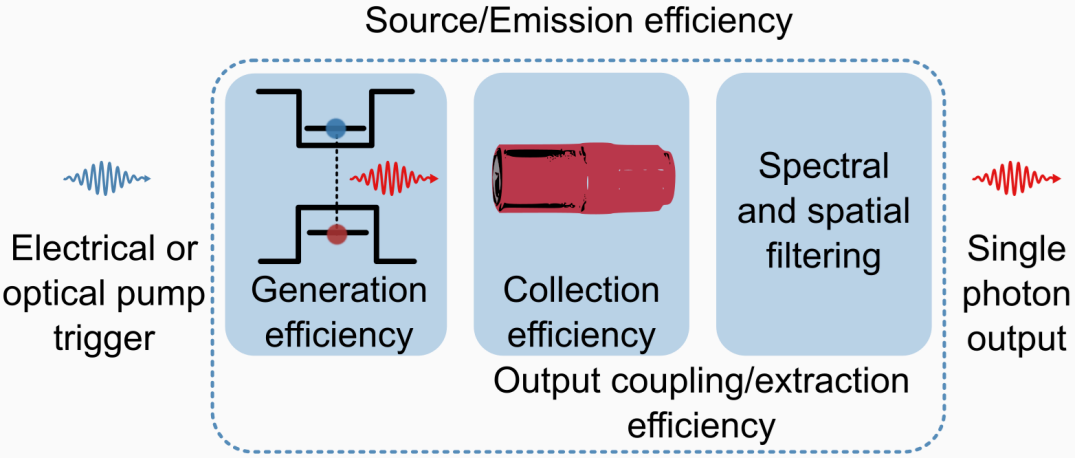

FIGURE 1.13: Different components for the determination of the extraction efficiency, after [182].

Typically, for experimental determination of the extraction efficiency, two methods are used to measure the setup efficiency (at the same wavelength as a source). Firstly, one can measure the transmission of all of the components and calculate the transmission of the experimental setup with a pulsed source with a known repetition rate (typically around 80 MHz) and compare it with the signal count rate (corrected for multiphoton events).

The second method involves the use of the source with the known average number of photons (e.g. highly attenuated pulsed laser) and guiding it through the experimental setup onto detectors. With the known power of a laser and an energy of one photon at a specific wavelength $E = \frac{hc}{\lambda}$, one can calculate the number of photons and compare it with the count rate on the detector to infer the setup efficiency. The experimental results are given in Chapt. 3. In the case of a PIC, this measurement allows for the determination of the extraction efficiency from the edge of the sample - signal outcoupled from the Si waveguide. In pair with simulations of light transfer, it allows for the indirect determination of the on-chip coupling of photons.

1.7.5 Automated real-time stabilization software for the optical microscope setup

This section is based on published work [181] and more details are given therein. Described µPL setups for near-infrared microscopy (see Fig. 1.9), used to investigate semiconductor nanostructures, require micrometer and nanometer mechanical stability due to the use of high magnification of optical objectives. However, the continuous flow cryostats used for the operation of the PIC chip at the cryogenic temperature, along with other mechanical components, introduce mechanical vibrations and temperature drift within the optical setup. Therefore, it poses a significant challenge, as reliable data collection requires excitation and detection from the exact same location on the chip in long-term experiments. To minimize mechanical instabilities, the setup is adjusted in real time by an operator; however, this is not an optimal solution.

To address these issues, a new software-based solution was developed along with certain setup modifications, allowing automatic control of crucial optical elements. The software allowed for precise control of the position of a cryostat with the PIC chip inside with respect to the microscope objective position and its focal plane via the implemented automated vision-guiding. Therefore, a precise stabilization of the optical setup in real time has been achieved. The Python-based software, featuring a graphical user interface, uses the normalized correlation coefficient matching method from the openCV library to accurately detect characteristic elements of the inspected chip and automatically correct any misalignment with pixel-level accuracy and 0.2 µm precision in real-time. The flowchart of the software is presented in Fig. 1.14.

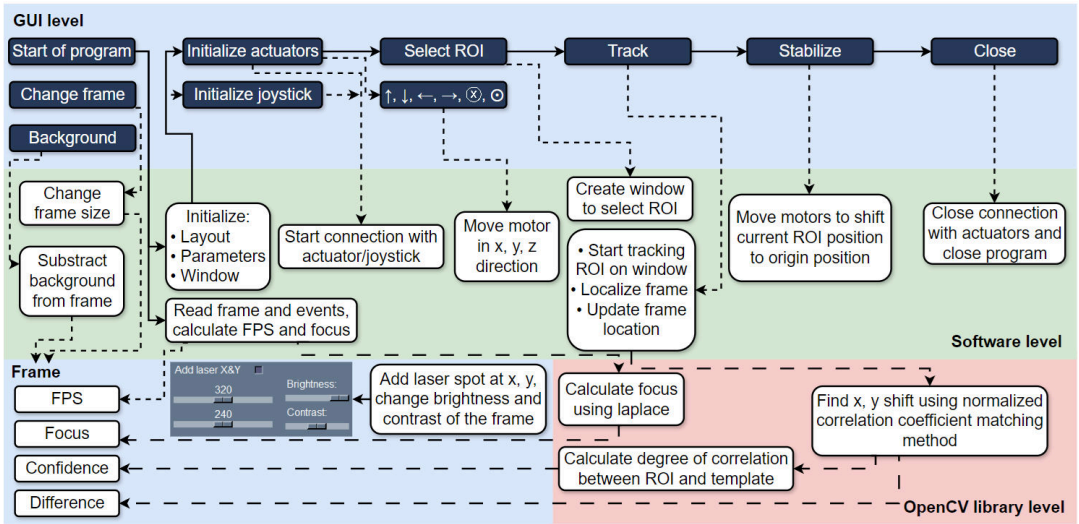

FIGURE 1.14: The flowchart illustrates the interaction among the GUI, software, and OpenCV library layers. Solid arrows represent the typical sequence of operations within the workflow. Published in ref. [181].

1.7.5.1 Normalized correlation coefficient matching algorithm

The core of the software's functionality relies on the normalized correlation coefficient matching method implemented from the openCV library. During the development phase, all available template matching algorithms from the library were tested, along with the phase correlation method [183] and the Haar cascade classifier. Although the correlation coefficient matching method has been shown to offer the highest precision and confidence in finding a match, it also comes with a higher computational cost, limiting the size of the image frames based on available computing resources. Unlike neural network-based models, which require extensive training data, this method only requires a single template snapshot for tracking, making it more adaptable. The algorithm is robust against variations in translation, brightness, and contrast, which are common in optical microscopy setups. The algorithm normalizes both the template and the image by setting their means to zero, transforming darker areas of the image into negative values and brighter areas into positive ones. This adjustment ensures that when bright regions in the template overlap with bright areas in the image, the resulting dot product is positive, and the same occurs when dark regions overlap, as the product of two negative values also results in a positive score. Conversely, mismatches, such as dark regions in the template overlapping with bright areas in the image, produce negative values. The matching process can be summarized by the following relations:

$$R(x,y) = \frac{\sum_{x',y'} \left(T'(x',y') \cdot I'(x+x',y+y')\right)}{\sqrt{\sum_{x',y'} T'(x',y')^2 \cdot \sum_{x',y'} I'(x+x',y+y')^2}} \tag{1.19}$$

$$T'(x',y') = T(x',y') - \frac{1}{(w \cdot h)} \cdot \sum_{x'',y''} T(x'',y'') \tag{1.20}$$

$$I'(x+x',y+y') = I(x+x',y+y') - \frac{1}{(w \cdot h)} \cdot \sum_{x'',y''} I(x+x'',y+y'') \tag{1.21}$$

In this context, I represents the source image and T denotes the patch image that is compared to the source image. The variables w and h correspond to the width and height of the template image, respectively. The coordinates range as follows: $x' = 0...w-1$, and the $y' = 0...h-1$. The template is moved one pixel at a time (left to right, then top to bottom). For each location, a metric R is computed that yields values between -1 and 1, indicating the degree of correlation between T and I at a specific position, thereby forming a result matrix R. In the software, the function minMaxLoc() is utilized to determine the highest value within the R matrix. In each frame, this location is compared to the one established when the user selected the region of interest (ROI). If the specified pixel threshold (typically set to 0 for maximum precision) is exceeded, the program controls the motors to reduce the deviation below the threshold, which effectively returns the ROI to its original position.

Focus detection

As an addition to the software, the focus value metric was developed, and the frame's focus value is determined by calculating the variance of its Laplacian. The Laplacian provides a two-dimensional isotropic measure of the image's second spatial derivative, highlighting regions with rapid brightness changes. This feature is used to adjust the microscope objective in the z-axis to locate the point of maximum image contrast—i.e., the focus position. The Laplacian of an image can be computed by applying a convolution filter with a small kernel to the frame.

$$\begin{bmatrix} 0 & -1 & 0 \\ -1 & 4 & -1 \\ 0 & -1 & 0 \end{bmatrix} \begin{bmatrix} -1 & -1 & -1 \\ -1 & 8 & -1 \\ -1 & -1 & -1 \end{bmatrix}$$

FIGURE 1.15: Two common Laplace kernels.

Chapter 2

Heterogeneous integration of III-V material

This chapter outlines the fabrication methods and procedures used to fabricate the devices characterized in this thesis. It covers integration technologies, direct bonding, and micro-transfer printing, as well as the lithographic processes used to fabricate the waveguides and cavities. Since fabricated devices share multiple fabrication and characterization steps, the fabrication and characterization techniques used are described first, and in subsequent chapters, the used procedures are given.

2.1 Fabrication methods

2.1.1 Direct bonding

Direct bonding is the fabrication processing technique that allows two materials to be joined together (typically two semiconductor wafers or a wafer and a processed chip). It is sometimes referred to as glueless bonding or van der Waals bonding. The prerequisite for a high yield of this process is the flatness and cleanliness of the wafers [184, 185]. Because the surfaces of a wafer bond with water molecules from the air as seen in Fig. 2.7, they have to be treated with oxygen plasma shortly before the wafers contact. This technology is used to bond materials where joint growth or processing is impossible (e.g. due to different crystalline structures). This is an essential processing step in the presented device fabrication technology - wafer bonding of the InP with InAs quantum dots and SOI platform.

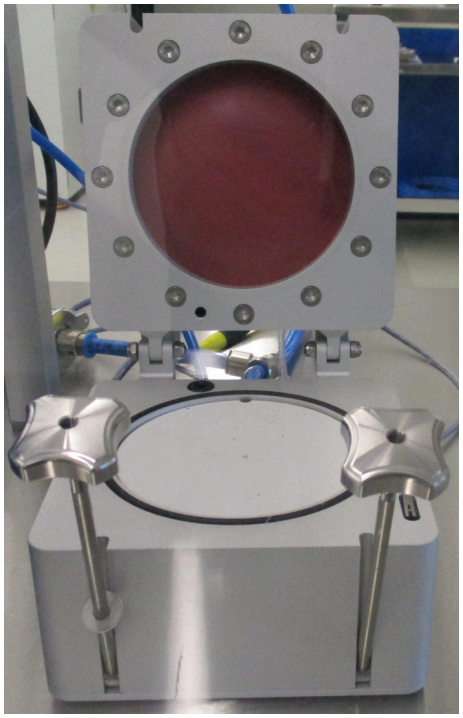

FIGURE 2.1: Used NILT Compact Polymer Bonder with visible slot for 4" substrate.

For all of the described direct bonding (and adhesive bonding with use of the BCB) the NILT compact polymer bonder was used (visible in Fig. 2.1). It allows the bonding of 2" and 4" substrates and chips. The process temperature can be between 20 °C and 300 °C in atmospheric pressure or in vacuum. The bonder can supply pressure up to 6 bar. The parameters used for direct bonding of InP wafer with InAs QDs are given in Sect. 3.2.

2.1.2 Micro-transfer printing

The second important integration method used in this work was micro-transfer printing (µTP or sometimes referred to as MTP). This method facilitates the integration of various semiconductor devices onto different substrates. These devices are initially fabricated on their native substrates, such as silicon, gallium arsenide, or indium phosphide, using standard epitaxy and lithography techniques. Subsequently, the sacrificial layer under the device layer is etched away, leaving the device connected only by thin tethers (from native material or resist ones). Microstructured stamps made of polydimethylsiloxane elastomer (PDMS, see Fig. 2.2 b)) use Van der Waals forces to pick up devices by pressing and breaking the tethers. The stamps then transfer the devices onto another substrate, such as pure silicon, an SOI chip, indium phosphide, silicon nitride, lithium niobate, gold, titanium, glass, and other

materials. In this context of micro-transfer printing, a device typically is a part of a coupon, which is a small section or piece of a semiconductor or other thin-film material that is pre-fabricated and then selectively removed from a donor substrate for transfer onto a receiving substrate. Coupons are often used to create heterogeneous structures, allowing precise placement of micro-devices like LEDs, lasers, or sensors on various surfaces without needing to grow or fabricate the materials directly on the final substrate. In the initial phase of the µTP process development, the coupon transfer technology was established, where there were fabricated 50x50 micrometer sized fields in InP (called coupons) with either resist or InP tethers. Later, as the process matured, it was switched to the direct fabriaction of a device (InP nanobeam of a size about 1x20 micrometer with InP tethers) transferred directly to a target substrate.

In this thesis there was used the Micro Transfer Printer (µTP-100 Transfer Printing System) manufactured by X-Celeprint Ltd. This system comprises three elements: the transfer stage visible in Fig. 2.2 a), the electrical cabinet, and the PC user interface. This transfer stage is composed of three main elements: the optical path with a stamp and stages for 6" source and target wafers. The angle position of these wafers can be fine-tuned with a differential screw. The stamp, source, and target are positioned by creating an underpressure (vacuum). The motorized stages allow for the source and target movement in the x and y directions, and the optical microscope and stamp can move separately on the z-axis. In addition, the cleaning pad for the PDMS stamp was mounted and made available for automatic processes. As they are crucial for an efficient transfer, the stamp parameters during the process of micro-transfer (overdrive distance, acceleration, overdrive speed, pre-pickup time) were characterized and described in Sect. 4.1.1. The overdrive distance is the distance which the stamp will travel towards the source after positioning on top of a structure. Overdirve speed is a velocity with which the stamp will travel overdrive distance. The pre-pickup time is a time for which stamp movement will be stopped after reaching overdrive distance. Acceleration parameter is an acceleration of a stamp during the pick-up process.

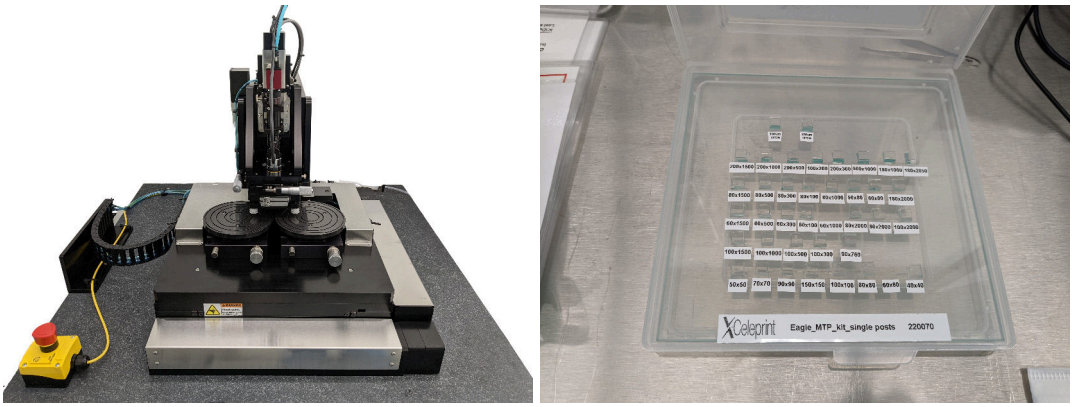

(a) Micro Transfer Printer (µTP-100 Transfer Printing System) from X-Celeprint in DTU cleanroom.

(b) µTP kit - single posts of various sizes.

FIGURE 2.2: Used setup (a) and PDMS stamps (b) for micro-transfer printing.

Adhesion to the stamp

The µTP process is based on carefully balancing the adhesion between many components: the top layer of the source, the PDMS stamp, the bottom of the source, and the top of the target layer. Typically, the adhesion forces should follow this relation:

Pick-up	**Printing**
PDMS > Tethers	Source-Target > PDSM

TABLE 2.1: Relation between forces for a successful pick-up and print of a structure.

The main principle allowing for a PDMS stamp to operate in the pick-up and printing regime is a viscoelastic effect where the strength of the adhesion changes with the stamp speed. This phenomenon is called kinetically switched adhesion, which leads to strong adhesion when the pick-up speed is fast and weak adhesion when the printing speed is slow. In the case of the vertical pick-up, the separation energy G_{PDMS} depends on the delamination speed v and can be approximated by:

$$G_{PDMS}(v) = G_0 \left[1 + \left(\frac{v}{v_0}\right)^n\right] \tag{2.1}$$

where G_0 is the separation energy at rest ($v = 0\ \frac{mm}{s}$), v_0 is the pick-up speed at which $G(v) = 2G_0$, n is a fitting parameter. The G_0 depends on the PDMS stamp (its composition, material, and wear) and can change during its use. If the force G_{PDMS} is greater than F_{SUB}, which is the force of adhesion of the structure to a substrate, then the removal of a structure will be possible. In the opposite case, printing is possible. Consequently, there is a stamp speed condition for picking up $v > v_c$ and $v < v_c$ for printing.

Tethers

During the membranization of the structure, the device layer has to be suspended and secured to the whole wafer or chip before transfer. The structures that hold the membrane are called tethers; their design can be categorized into resist (polymer) tethers and semiconductor tethers (from the source material). They can be designed in various shapes and sizes to create tethers that detach easily and smoothly when the device is lifted from the initial wafer and have a smooth bottom surface for good adhesion to a target wafer. The advantage of resist tethers is that the breaking force is usually much smaller than that of a wafer's semiconductor material. Consequently, they can be larger and fabricated with optical lithography, which is much more available than electron beam lithography (which was used to create small tethers from InP).

Resit tethers

As a first approach to tethers, resist tethers were used, but they turned out to be suboptimal to InP tethers. Depending on the selected layers, sidewall protection with a resist may be necessary during membranization. The resist sidewall is made by overlapping the edges, which should be protected with a resist. Designing sidewall protection with sufficient tolerance (4 µm was determined to be adequate) is crucial to accommodate potential misalignment, as such misalignment could lead to etching beyond the intended areas and collapse the coupons. AZ 5214 E was tested for resist tethers and yielded identical results to AZ MIR 701.

Release technology

One of the crucial steps in the sample fabrication is the membranization process, where the chip is immersed in an etchant (BHF or $FeCl_3$) and the sacrificial layer (i.e. InAlAs or SiO_2 is etched away). The device layer is not damaged because of the high selectivity in which oxidation-reduction chemical reactions act only on the sacrificial layer. To obtain devices with a flat and smooth bottom surface, the purity of the ingredients must be high. Etchant sometimes may require filtering to reduce particle contamination levels (especially in the case of $FeCl_3$).

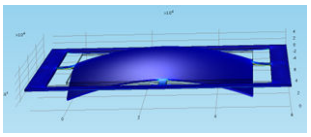

One of the biggest challenges in the membranization process is stress management, surface tension, and electrostatic forces between the bottom of a coupon and the substrate, which cause the collapse of the coupons and nanobeams. At this micro-mass scale, any gravitational forces can be neglected. A visualization of this stress-induced bending is shown on the right, featuring a COMSOL simulation that accounts for the effects of high deposition temperatures and subsequent layer shrinkage during cooling. The model includes a 250 nm InP device layer with a 250 nm SiO_2 mask layer on top, applied to a 50 × 50 μm^2 coupon. Vertical deformations are in the range of 1 µm (in the picture, deformations are not to scale), causing the sticking of a coupon to a substrate. Therefore, the SiO_2 top layer was replaced by the SiN one, where compressive and tensile stresses could be engineered. The alternative approaches in the nanostructure membranization which are avoiding surface tension of water are: supercritical drying (with CO_2) [186], Xenon-based drying [187] and sulfur-based solutions.

2.1.3 Characterization

The properties of the samples fabricated and processed in a cleanroom were checked by various inspection methods, i.e. microscopy (optical, interferometric, SEM, and AFM) and ellipsometry. In this section, a brief description and representative results of these methods are provided.

2.1.3.1 Microscopy

Optical Microscopy

In the cleanroom, the most widely used optical microscope for optical characterisation was the Nikon ECLIPSE L200N, equipped with microscope objectives of 2.5x - 100x and an eyepiece with 10x magnification. The working distance for the 100x objective is 1.0 mm, with a numerical aperture of 0.9 and a resolution of 0.37 µm. The microscope images were taken with a camera resolution of 2448 x 2048 pixels (5 MP). Semi-automatic stitching was used for large-area images. The primary purpose of the optical microscope was to inspect and analyze the pattern dimensions and quality after various lithography steps and to inspect any inhomogeneity and cleanliness of the sample surface.

Optical Profiler

The primary purpose of the optical profiler with the S Neox sensor head was to perform 3D topographic imaging of surfaces, step height measurements in smaller trenches and holes than those achievable with standard stylus methods, and roughness measurements with a larger field of view (FOV) than the Atomic Force Microscope (AFM), although with less spatial resolution. It can also be used to measure

the shape of large, rough surfaces using Focus Variation and for thick- and thin-film measurements, provided the refractive index is known. This optical profiler integrates three techniques: confocal and interferometry methods along with Active Illumination (Ai) Focus Variation — and can perform both thick- and thin-film measurements on transparent layers. This configuration allows for precise and flexible measurement capabilities, making it suitable for various advanced imaging and profiling applications requiring fast 3D topographic imaging of surfaces. Fig. 2.3 shows a representative result with an optical profiler performed in a DTU cleanroom.

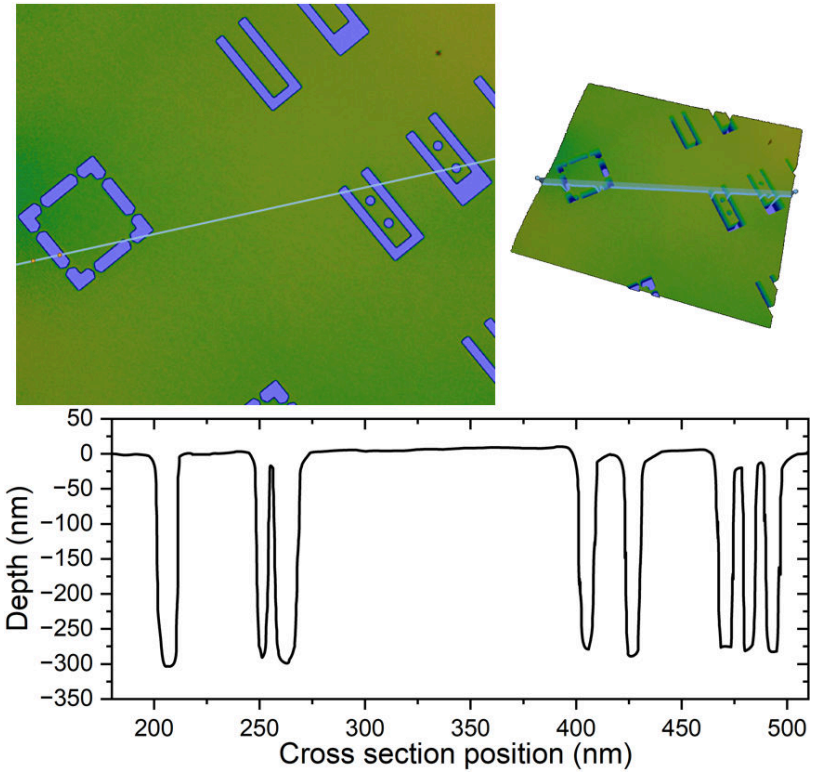

FIGURE 2.3: Examplary result of an optical profiler measurement of a coupon and cantilevers (used to investigate stress in the structure), with the height difference measurement in the bottom and 3D profile in the top right corner.

Scanning Electron Microscopy

The Zeiss Supra SEM can produce highly magnified images of various specimens, with magnifications exceeding 5×10^5 and offering ultra-high-resolution imaging. This equipment was essential and extensively utilized to achieve high-resolution and depth-of-field images while not requiring sample preparation. Its primary purpose was to measure conducting and semiconducting samples. The accumulation of charge in non-conducting materials (e.g. SiO_2) leads to deflection of the electron beam, lowering the resolution and interfering with the measurement. In terms of performance, the maximal resolution of this SEM ranges from 1 nm to 2 nm. Still, it is limited by vibrations and highly dependent on the sample type and the operator's skills. The instrument is equipped with several detectors, including a secondary

electron (SE2) detector, an Inlens secondary electron (Inlens) detector, which were most commonly used, a high-definition four-quadrant angular selective backscattered electron detector, and a variable pressure secondary electron (VPSE) detector that were also available. The electron source is a Field Emission Gun (FEG), and the SEM operates at fixed high vacuum pressures ranging from 2×10^{-4} mbar to 10^{-6} mbar. The SEMs of the fabricated structures are presented in the later chapters.

Atomic Force Microscopy

In the DTU cleanroom, the Bruker AFM Dimension Icon-Pt instrument was used. AFM is a scanning probe microscope that scans a sharp probe across a surface in various modes, such as contact or tapping. This technique produces a surface topographic map with a lateral resolution of approximately 1 nm and a vertical resolution of less than 1 nm, making it highly effective for topographic characterization at the nanometer scale. However, the primary limitation is often the size of the probe used. The primary purpose was to measure surface roughness and to assess step or structure heights within the nanometer and sub-micrometer range. Fig. 2.4 shows an exemplary result of an AFM measurement performed in a DTU cleanroom (the measurement was carried out with the help of Monika Mikulicz). This measurement was done for one of the first designs for the nanobeams directly transferred from the source wafer (without coupon); the area was too small to perform this measurement.

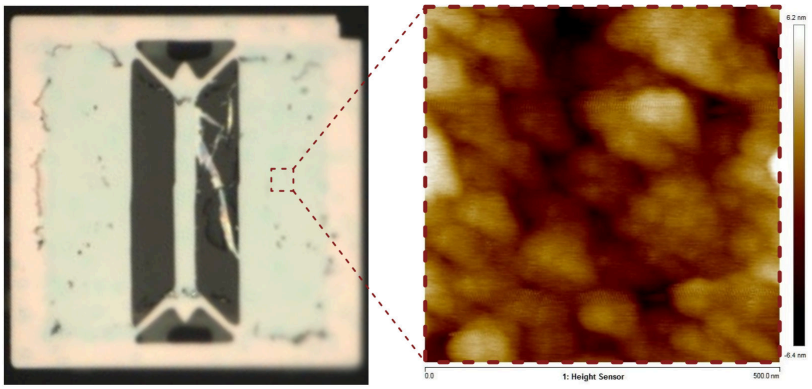

FIGURE 2.4: Image on the left presents one of the early devices attached to the PDMS stamp. The AFM image on the right of the surface of the bottom of an early version of the design. The Z range is 13.1 nm, and surface roughness Rq 1.77 nm over an area of 500 x 500 nm^2.

2.1.3.2 Ellipsometry

The ellipsometer (VASE, J.A. Woollam) is an instrument that was used to determine the thickness of thin films, both single-layer and multilayer, as well as to measure the refractive index. It works by measuring changes in the polarization of light as it interacts with the sample. In addition, the ellipsometer was able to measure reflectance and transmission intensity. The film thickness and optical constants can be

estimated by fitting an appropriate model to the acquired data. In particular, the accuracy of these results is highly dependent on how well the chosen model represents the actual sample and the quality of the fit. Since it is challenging to quantify the accuracy of the results, it is essential to ensure that the model aligns with the known characteristics of the sample and to refine the fit to achieve the lowest possible Mean Squared Error (MSE). This instrument is particularly effective for measuring thin films, such as oxide layers less than 100 nm thick. The ellipsometer can measure SiO_2 film thicknesses ranging from less than 20 Å to approximately 10 µm. Typical thin films that can be measured include SiO_2, SiN, thin metals, various photoresists, polymers, SOI materials, and many others. This spectroscopic ellipsometer operates at angles ranging from 45 deg. to 90 deg. It covers a wavelength range of 210 to 1690 nm, with a spectral resolution of 1.6 nm pixel resolution, a 5 nm bandwidth for wavelengths between 280 nm and 1000 nm, and a 3.4 nm pixel resolution and a 10 nm bandwidth for wavelengths between 1000 nm and 1690 nm.

In Fig. 2.5 there are shown the exemplary results of the ellipsometry measurements for two layers stack (for sample integrated using µTP), SiN/Si and SiN/InP/SiO_2/Al/Si, the red and green lines represent the measured data, and the black line represents the fitted model. The fit between the experimental data and the model is in good agreement, with a low MSE within a wide spectral window (300 - 1690 nm). After a satisfactory fit, it becomes possible to determine parameters such as the refractive index and thickness of the materials, allowing for a fast evaluation of the grown or etched layer stack.

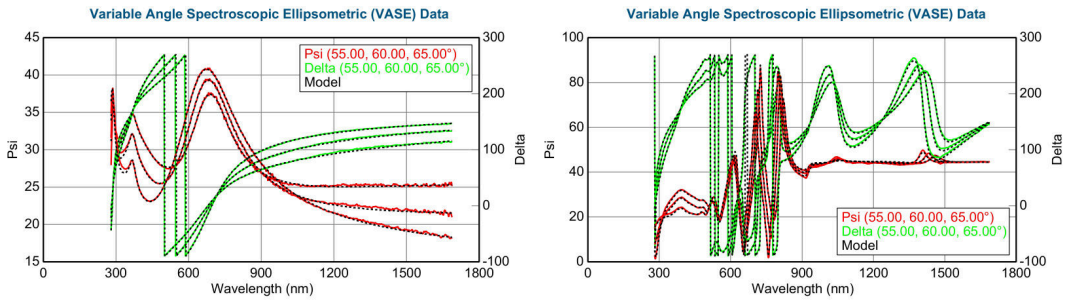

(a) SiN/Si (b) SiN/InP/SiO_2/Al/Si

FIGURE 2.5: (a) VASE data for a PECVD grown SiN of 93 nm on the Si substrate (b) Multilayer VASE data for a sample with the 110-nm-thick Al layer, 615 nm SiO_2, 308 nm of InP, and 95 nm of SiN. Measurement during the fabrication of the sample integrated using µTP.

2.1.4 Lithography

Lithography is one of the most used, precise, and suitable techniques for the mass production of semiconductor microstructures and nanostructures. This process starts with designing the mask file using GUI tools such as CleWin or KLayout. It is possible to parameterize and automate the creation of complex mask layouts using the gdspy (Python module). Briefly, in the lithographic process, after the substrate is

prepared through the deposition of, e.g. HMDS, the resist layer is spin-coated, and the mask is exposed. Lithography can be classified into two categories: electron-beam lithography and optical lithography, depending on whether the electrons or photons are used to expose a mask on the resist layer. After exposure, the wafer or chip is developed, and the pattern can be etched on the substrate with dry or wet etching. The last step usually involves the removal of the resist layer, e.g., in an ultrasonic bath with a solvent. All steps in this process should be inspected with the characterization tools. This process is illustrated in Fig. 2.6.

FIGURE 2.6: Spatial light modulator projects a laser light onto the wafer exposing deposited resist. The pattern is developed and etched, and the resist is stripped. In this example, a positive photoresist is used.

HMDS

HMDS (Hexamethyldisilazane) is a chemical primer that enhances photoresist adhesion to the substrate. It modifies the substrate's surface, making it more hydrophobic and thus improving the bonding between the photoresist and the substrate. In addition, it ensures a more uniform coating, which is crucial to achieving precise lithographic patterns.

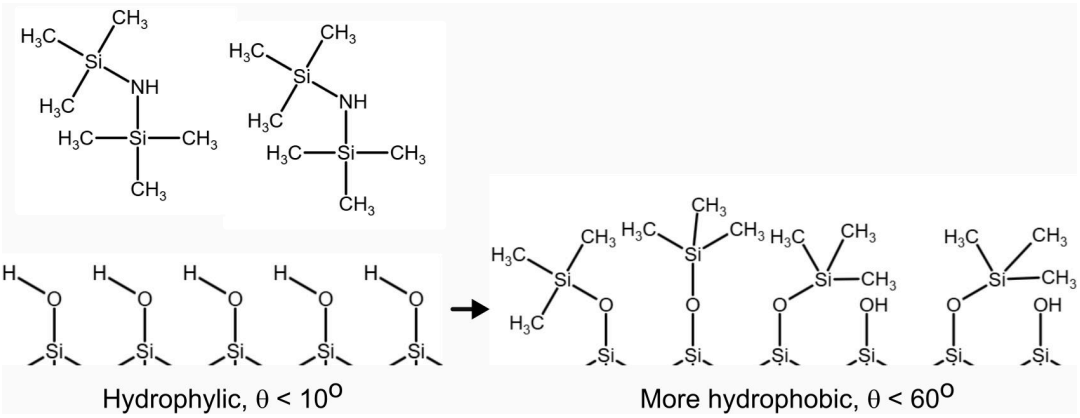

FIGURE 2.7: Surface modification using HMDS reduces surface energy by converting hydrophilic silanol groups into a more hydrophobic surface.

Alignment

If the fabrication process requires more than one lithography step, the layers must be precisely aligned. This can be achieved using alignment marks, such as crosses, boxes, and gratings. During fabrication, it was found that for maskless optical lithography, alignment crosses with a width of 1 µm have the best alignment accuracy compared to crosses with widths of 8 µm and 2 µm.

Mask design

Mask design and inspection were done using CleWin and Klayout software. The Python-based software gdspy was used to develop the mask with parameterized patterns like hole radius and taper design.

Optical and electron beam lithography

For optical lithography, the Heidelberg Instruments MLA150 Maskless Aligner was used. This maskless system was beneficial because it allowed for quick prototyping of the designs, compared to traditional photolithography, which involves creating a physical photomask, followed by using a stepper or mask aligner to project the CAD-designed pattern onto a resist-coated wafer or plate. The limit of the resolution given in Tab. 2.2 is given by the exposure wavelength (in this case, the laser diode at 405 nm). For the fabrication of the smaller features, the electron beam lithography was used (JEOL JBX-9500FSZ) with a resolution limited by electrons' scattering to about 10 nm.

TABLE 2.2: Comparison of used optical and electron beam lithography at DTU.

Category	UV Maskless Lithography	E-beam Lithography
Minimum Resolution	∼0.6 µm	∼10 nm
Process Time (4')	Tens of minutes	Hours
Throughput (4')	0.4 – 5 wafer/hour	0.1 – 3 wafer/hour
Training	Few hours	Long, for Ph.D. students and up

Spin coating

In the spin coating process, to apply a thin uniform resist film, a liquid photoresist is deposited onto the center of a substrate and rapidly rotated. The centrifugal force evenly spreads the solution across the surface, and the rotation speed and the viscosity of the solution control the film thickness. Most of the spin coating was done using a Süss MicroTec Gamma 2M spin coater, which is a fully automatic and programmable cassette-to-cassette system. For chips and 2" wafers, after the deposition of HMDS, they were crystalbonded to the 4" carrier wafer. The typically used photoresist was a positive tone AZ MiR 701 (29 cPs) spun at 4000 rpm.

The manual spin-coater was used for a sample described in Sect. 5.1 with gratings. The wafers were pre-spin baked at 160 °C for 10 min. to dehydrate the surface. The 1:5 diluted BCB in 1-methoxy-2-propanol was spin-coated on a wafer for 60 s

at 5000 rpm with an acceleration of 1000 rpm/s^2 and baked at 90 °C for 10 min. to evaporate the solvent.

2.1.5 Wet and dry etching

The main difference between wet and dry etching is that wet etching easily allows isotropic etching. This is crucial for removing material underneath a layer, which is useful in forming structures such as coupons and membranes. Dry etching is typically anisotropic, allowing the precise transfer of a mask pattern to a wafer with better control of the feature's shape. Wet etching is generally used to etch larger volumes of material than dry etching, but it is less controllable and precise. The brief comparison is given in Tab. 2.3.

Wet etch	**Dry etch**
High etch rate difference between materials, leading to high selectivity	Anisotropic etching is possible
Time-saving: Can etch multiple chips simultaneously	Does not attack the backside of the sample
Easy to start up new etch solutions	

TABLE 2.3: Comparison of wet and dry etch.

Wet etching

For integration using the μTP, it is necessary to etch any epitaxial structure (sacrificial layer) underneath the device layer (typically the InP layer with InAs QDs). In this process, the selective chemical reaction removes a sacrificial layer underneath the device layer, while it does not damage the surrounding layers. For flat and smooth surfaces, the etching agents of high purity and high selectivity must be used; a selected combination of device materials, sacrificial layers, and etching agents is given in Tab. 2.4.

Device material	Sacrificial layer	Etchant
InP	InGaAs	$FeCl_3$
InP	AlInAs	$FeCl_3$
GaAs	InAlP, InGaP	HCl
SOI	SiO_2	BOE
SiO_2	Si	TMAH, KOH
$LiNbO_3$	SiO_2	BOE

TABLE 2.4: Selected device material platforms and compatible sacrificial layer with its etchant.

Wet etching of the sacrificial layer InAlAs and SiO_2, as well as any other wet chemistry process, was carried out in a fume hood. Before the etching of the devices, the etch rates were tested on sacrificial unpatterned parts of a wafer or chips.

InAlAs etch

For chips with the InAlAs sacrificial layer, wet etching was performed using a $FeCl_2$:DI (1:2) solution, with the ratio precisely maintained with a graduated cylinder in each batch. The mixture was stirred with tweezers for 10 seconds to ensure uniformity. Various etching times were tested for different batches, specifically 5, 6, 7, 10, 11, and 12 minutes. After etching, the chips were removed from the solution, immersed in DI water for a few minutes, and then placed on paper, with any remaining water gently removed using a flow of N_2 gas. It was observed that slow air drying of a wet chip led to the accumulation of particles on its surface, which should be avoided. The etch depth followed a linear relation with the etching time. The etch rate coefficient was determined to be 2.9 µm/min from linear regression and this value represents a lower boundary estimate. In some cases, the etching rate may be faster. However, it is preferable to etch for a longer duration than the calculated time to ensure complete etching. There are also visible slight saturation effects near the center of the square device, suggesting that more etch time is required for correct processing.

SiO_2 etch

The SiO_2 etching was done using buffered oxide etching (BOE), typically used to etch silicon dioxide on silicon wafers. Used BOE combined hydrofluoric acid and ammonium fluoride in 7:1 proportion. Etching solutions containing ammonium fluoride produce silicon surfaces that are atomically smoother than those etched with just hydrofluoric acid. BOE has a slower and more consistent etch rate and is less harsh on photoresists because of its nearly neutral pH solution. Typically, the etch rate for BOE is given for thermal oxide (about $80\frac{nm}{min}$), but for PECVD deposited thin film, it is much faster and estimated from the tests to be $200\frac{nm}{min}$. Fig. 2.8 presents an SEM image of the cross-section of the InP waveguide with SiO_2 partially etched underneath, which is one of the samples used for the calculation of the SiO_2 etch rate in BOE.

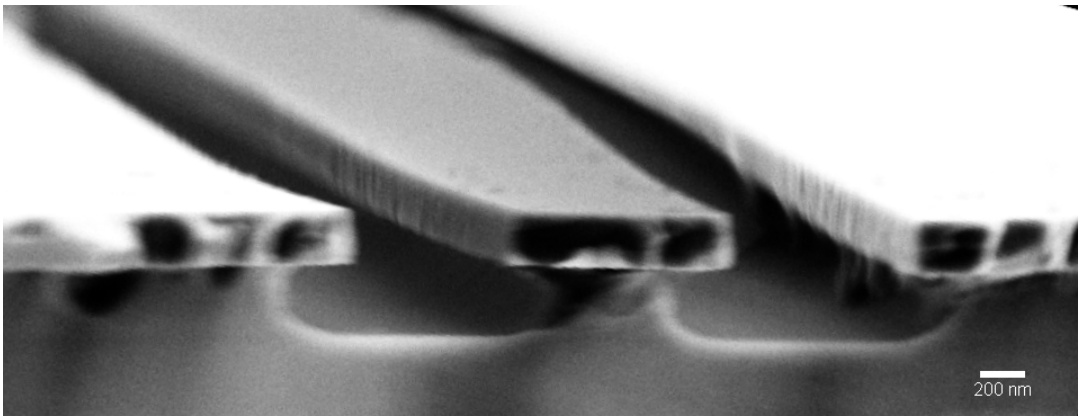

FIGURE 2.8: InP waveguide on top of the SiO_2 layer which is partially etched with BOE 7:1.

Dry etching

Inductively coupled plasma (ICP) etching was used for dry etching. It combines chemical and physical etching processes, making it effective for the precise removal of isotropic materials at the nanoscale. The process uses gases that chemically react with the substrate, forming volatile products alongside a physical bombardment of particles. This approach offers several benefits, including increased reactivity of reactants as a result of the dissociation of gas molecules into more reactive components, high tunability through precise control of ion acceleration, parallel processing of the substrate, and the creation of a well-collimated beam that ensures efficient etching. However, these advantages come with the trade-offs of increased complexity, high costs, and the requirement for toxic or hazardous gases. The etched depth is governed by the etch rate of both the substrate and the mask. The selectivity, or the ratio of these two rates, determines how deep the etching can proceed before the mask is etched away, with desired depths ranging from tens of nanometers to the full thickness of a wafer. Additionally, the sidewalls and surface roughness produced by the etching process are crucial, with requirements that vary significantly depending on the application.

Since the used ICP system also incorporates both an optical endpoint system and a laser endpoint system for early samples, there were fabricated 500x500 μm^2 fields to check the etched layer in real-time. It was found not to help detect an overreaching of layers due to a lack of precise signal change for the next layer. However, the fields were great for checking resist residue and with a profilometer (Dektak) it was possible to check the etching distance.

SiN etch

After the development of the mask in the CSAR e-beam resist, this pattern has to be transferred to the SiN hard mask. This was done with ICP SiN etching. This SiN etching was done at the temperature of 20 °C with fluorine chemistry and the ratio of 10:2:2:1 of the N_2:SF_6:CF_4:CH_4 gases. The SiN etch rate was about $60\frac{nm}{min}$. It is

important to completely remove the CSAR e-beam resist in an appropriate solvent (e.g. remover 1165 from MICROPOSIT^{TM}) after SiN etching since its residues will increase the roughness of the InP surfaces, which in turn decrease cavity quality factors.

InP etch

For the InP etching, the SiN layer was always the mask. InP ICP etching was performed at a temperature of 180 °C with bromine chemistry and a 1:3:5 ratio of Ar:CH_4:HBr gases. Immediately after the sample was unloaded from a process chamber, the samples were immersed in deionized water (DI) to stop the continued etching after exposure to the atmosphere caused by residual bromine. The InP etch rate was about 430$\frac{nm}{min}$. For some structures for which there were also InAlAs instead of SiO_2 under InP, its etch rate was about 200$\frac{nm}{min}$ in the same process.

2.1.6 Thin film deposition

To deposit thin layers of SiN and SiO_2, the Plasma Enhanced Chemical Vapor Deposition (PECVD) system was used. This system is also capable of silicon oxynitride, and boron and phosphorus doping. PECVD is a chemical vapor deposition method that utilizes plasma to accelerate the chemical reaction rates of reactive species. This process enables the deposition at lower temperatures, which is frequently crucial in semiconductor manufacturing. In Fig. 2.9 there are shown color charts for SiN and SiO_2 that show how the apparent color of the layer changes with material thickness (the color of the dielectric film on silicon is determined by the incident angle of the light source, the source's luminance, the film's thickness, and the type of dielectric material). This allowed for quick evaluation of the film thickness in a cleanroom without additional measurement. The color of the deposited film is an essential factor because it affects the required exposure dose during photolithography because of changes in reflectivity.

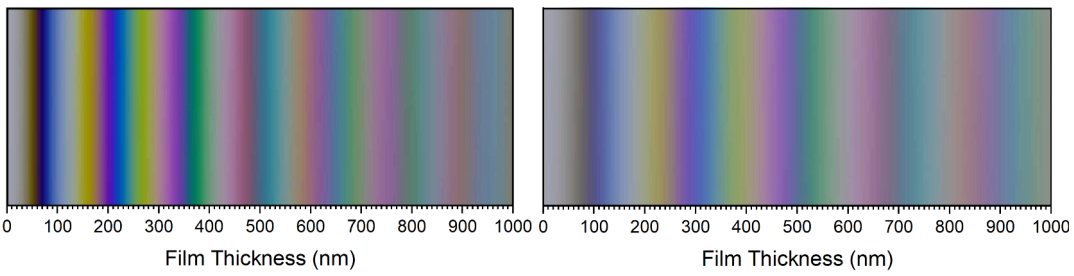

(a) SiN (b) SiO_2

FIGURE 2.9: Visible color of a (a) SiN and (b) SiO_2 film on silicon varies depending on its thickness, adapted from [188].

SiN deposition

The deposited SiN was used as a mask in a dry etching of InP. It was also used as

a stress management layer for the membranization process, where, with the deposition of SiN with high frequency, its tensile stress increases. It also increases chip brittleness, necessitating careful handling during debonding. The stress in SiN can be modulated by adjusting the deposition time ratio between high-frequency (HF) and low-frequency (LF) components. In the machine used (see Sect. 2.1.6), achieving a stress range of -450 MPa to 300 MPa was possible, changing the HF to LF deposition time ratio from 0 to 3. With the correct ratio, one can deposit an unstressed film. During fabrication, cantilevers were also fabricated, giving information on the stress in the structure. Under SEM, no bending was observed, indicating that the stiffness of the layers and their stresses are balanced. For all processes with high frequency SiN deposition, the gases ratio was SiH_4:NH_3:N_2 - 40:55:1960. The deposition rate was measured on an ellipsometer and was $110\frac{nm}{min}$.

SiO_2 deposition

The deposition of SiO_2 has served two purposes. Firstly, with its low absorptance (2-7 %) in a 1.0-2.0 µm spectral window, it is a suitable spacer material between InP and Al layers [46]. Secondly, it was used as a top layer after the micro-transfer printing process; by depositing it around the microstructure, its position was secured for handling and cooling down in the cryostat. For the deposition of SiO_2, the gas ratio was N_{20}:SiH_4 - 2000:17 in low-frequency generator mode. The deposition rate was measured on an ellipsometer and was $170\frac{nm}{min}$.

E-beam evaporation

The E-beam evaporator (Temescal) was used for metal deposition via electron-beam evaporation. In this process, the material is deposited in a line-of-sight manner from the source, meaning that it only coats the sample surface that directly faces the source. This characteristic makes it particularly effective for applications like the lift-off technique, by which a sample with Au (110 nm)/ Ti (5 nm) contacts layer was prepared (see Sect. 5.3.1). This system was also used for all the deposition of Al layers for samples which were bonded with Si.

2.1.7 Conclusions

In this section, the most important fabrication methods were presented: direct bonding, micro-transfer printing, characterization (optical, SEM, AFM, ellipsometry), lithography, wet and dry etching, and thin film deposition. The description of direct bonding and micro-transfer printing, their use and performance evaluation, will be presented in Chapt. 3, Chapt. 4, 5 and Sect. 5.4 respectively. In the following sections, the characterisation results for fabricated samples will be presented. The description of the InAs/InP QDs fabrication process has been omitted, and details can be found in Chapt. 3 and in the referenced publication [45]. Overall, the fabrication methodologies available at the DTU and presented above provided a wide set

of tools for advanced semiconductor processing for heterogeneous integration and played an essential role in the fabrication of PICs presented in this thesis.

Chapter 3

Heterogeneous III-V integration on SOI using direct bonding

In this chapter, a description of sample fabrication, including the direct bonding technique, is provided. The design of the device described in Sect. 3.1 is composed of six elements which are: InAs/InP quantum dot, InP waveguide, InP taper, InP outcoupler, Si waveguide, and cleaved edge. The operation of this device is as follows: the external pumping laser source generates excitations in an InAs/InP QD, which subsequently recombine, producing single photons around 1550 nm. These photons are guided through the InP/Si hybrid WG and, in the tapered section, are efficiently transferred to the Si WG beneath it.

One side of the chip, photons are outcoupled from the SI WG using the InP grating structure. From the other side, photons are outcoupled from a cleaved edge of the Si WG. Both photon output ports can be used to collect QD emission propagated through the Si WG within the µPL experimental setup to test photon coupling efficiency from the QD to the chip interior and off the chip and evaluate the fabrication technology. The direct bonding technique used here, as described in Sect. 3.2, enables the bonding of a full 2-inch epitaxially grown InP wafer to the SOI chip. As described in the author's contributions section the fabrication was done mainly by the dr. Paweł Holewa and dr. Aurimas Sakanas. The same processes e.g., direct bonding, optical lithography, wet and dry etching were later used by the author to fabricate samples in the next chapters.

In Sect. 3.2.1 there are presented studies of a single device to analyze the emission spectral pattern of the particular quantum dot (QD), in order to assess the purity of its single-photon emission, while this demonstration combines the coupling of photons from the InP/Si WG to the Si WG on the SOI platform, which could be scaled up to form complex integrated quantum photonic circuits.

3.1 Device design

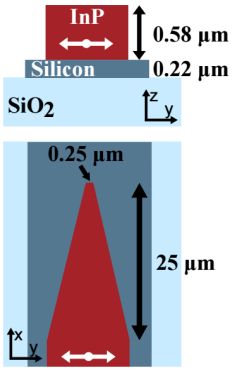

FIGURE 3.1: Diagram of the device design with an InP waveguide on a Si waveguide. Published in ref. [22].

First, the hybrid waveguide geometry is composed of an InP waveguide (with an InAs/InP QD) with linear tapers on both sides. This waveguide is placed on top of a Si waveguide, which is terminated on both sides with planar Si and the InP grating outcoupler. A tapered section is presented in the Fig. 3.1. The structure is optimized to achieve efficient mode coupling between the InP and silicon sections, with a tapered InP waveguide atop a silicon waveguide, enabling smooth transitions and low insertion losses. The device employs half of a circular Bragg grating outcoupler to effectively extract light from the Si waveguide, with parameters such as ring width and grating period tuned to optimize outcoupling performance. The dimensions in the design of the fabricated structures were based on those already published by the NQP group, where numerical studies for this material system have been performed via an FDTD in Ref. [189]. More about FDTD simulations-driven chip design is given in Sect. 3.1.1. In the structure, the nominal InP waveguide height is 580 nm on top of a 220 nm thick Si waveguide, and the widths of InP and Si waveguides are varied in the micrometer range. The length of the taper is 25 µm and its tip has a finite width of 250 nm as depicted in Fig. 3.1 on the right. The entire fabricated structure is demonstrated in Fig. 3.14.

3.1.1 FDTD simulations

The extensive simulations and optimization of this heterogeneously integrated InP/Si on-chip system are already presented in the literature by Dr. Paweł Mrowiński et al. [189]. These simulations revealed that in this hybrid waveguide design, multimode operation is unavoidable due to the refractive index contrast ($n_{Si} > n_{InP}$) within the target telecom C-Band window.

In Fig. 3.2, there are shown distributions of the electric field intensity in an exemplary InP/Si hybrid waveguide structure with a taper. Panel (i) shows the center of the structure with a emitting dipole source, taper section on the right, and transfer of light to the Si part. Panel (ii) shows the optical field distribution at the edge of the chip, which is used to calculate on-chip coupling efficiency and panel (iii) shows the far-field optical intensity distribution from the sample edge. By restricting the collection angle to 45 degrees, as achieved in the experiment with a 0.65 numerical aperture microscope objective, a far-field collection efficiency of 89% can be achieved.

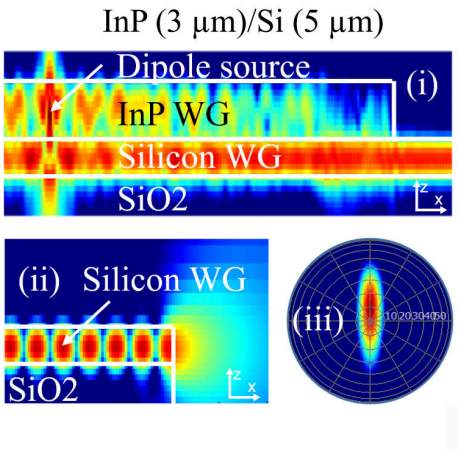

FIGURE 3.2: Electric field distributions in the simulated structures [22].

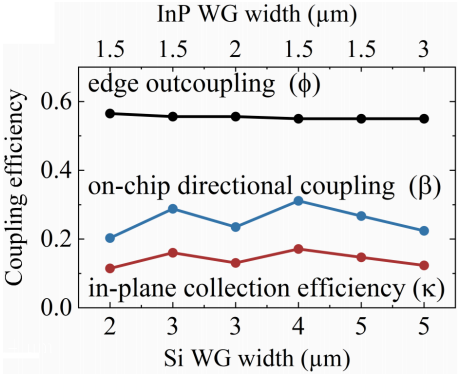

FIGURE 3.3: Calculated (solid circles) coupling efficiencies for the edge outcoupling and on-chip directional coupling for the fabricated geometries with lines as a guide to the eye [22].

Due to reflection at the Si WG edge/air interface, there are about 30% losses, which are the main contribution to losses for the edge outcoupling in such a device. These coupling efficiencies were calculated for different waveguide dimensions spanning the Si WG width from 2 μm to 5 μm and the corresponding InP WG width from 1.5 μm to 3.0 μm. The edge outcoupling efficiency (ϕ) is at a level of ∼60%, on-chip directional coupling (β) in the range of 20% to 30%. The in-plane collection efficiency (κ) is a product of edge outcoupling efficiency and on-chip directional coupling ($\kappa = \phi \times \beta$), and it is on the level of 10% to 15%.

Dipole orientation

The QD for the photonic integration circuits is simulated as a dipole source and its orientation (QD orientation) affects the properties of the system. In the numerical studies, the best scenario was investigated for the optimal coupling to TE-like propagating modes in the waveguide. The simulations assume that: (i) the dipole is localized in the center of the InP WG and (ii) the polarization is in-plane of the chip and perpendicular to the waveguide elongation axis. Polarization along the WG axis was not considered because, for the center position of the dipole, coupling to propagating modes is negligible (TE or even TM-like modes should have negligible field vector components along the WG). In the optical experiment, no polarization was

selected. As the fundamental excitonic states provide orthogonally polarized photon states (exciton - X and biexciton - XX photons are linearly polarized, whereas the charged excitons - CX produce circular or elliptical polarization [74]) and should not have notable polarization anisotropy induced only by a highly asymmetric confinement potential. Therefore, the utilized experimental setup had a lack of sensitivity to the polarization properties of detected photons. In other words, since X can emit in one of the two orthogonal linear polarization states, when the linear polarization is along or perpendicular to the WG elongation axis, one of the photons would always be coupled to the TE mode. This means that 50% of the total X emission is coupled to the mode. If the X polarization is at 45 degrees with respect to the WG axis, it would be coupled with 50% of one of the polarization states projected on the WG elongation axis and 50% of the other one. The same holds for the XX emission. For the CX emission, circular polarization would always be coupled at 50% to the TE WG mode. Figure 3.4 schematically shows that randomly oriented with respect to the TE WG mode, linearly polarized H and V photons give constant intensity when projected to the linearly polarized TE mode.

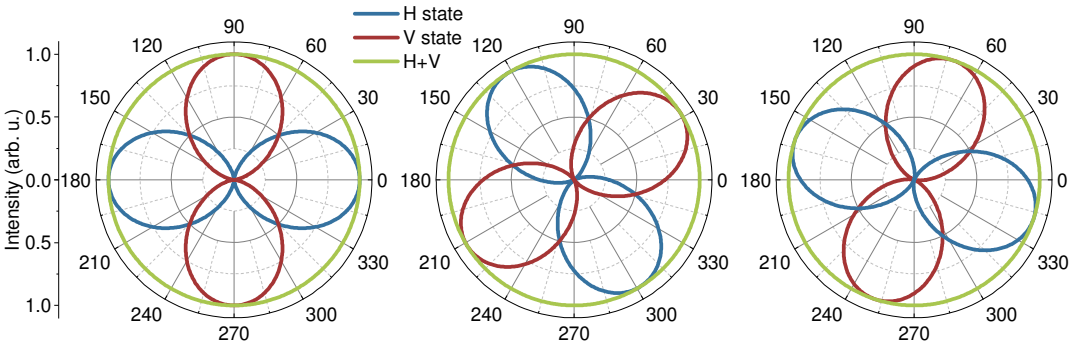

FIGURE 3.4: Polar plot of two orthogonal polarized states of exciton showing that regardless of the dipole orientation (QD orientation with respect to the waveguide) their combined intensity (which is projected onto the TE mode) stays constant.

3.2 Chip fabrication

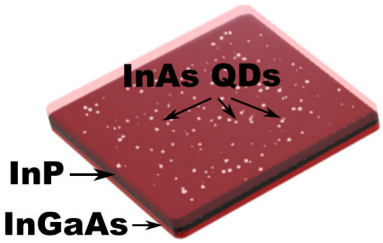

FIGURE 3.5: Epitaxy of InAs/InP QDs [22].

The chip fabrication begins with a low-pressure metal-organic vapour phase epitaxy (MOVPE) growth process on InP(001) substrates of low-density Stranski-Krastanov InAs/InP quantum dots (QDs) [45] (see Fig. 5.6). Initially, the InP substrate underwent thermal deoxidation at 650 °C in a phosphine (PH_3) ambient, followed by the deposition of a 0.5 μm-thick InP buffer layer at 610 °C. Subsequently, the substrate temperature was lowered to 485 °C for quantum dot growth. The growth process included annealing the InP substrate in an arsine (AsH_3) ambient, enabling As/P exchange reactions to form a two-dimensional (2D) In(As,P) wetting layer (WL) with tunable thickness and composition. The thickness and arsenic content of the WL were controlled by varying the annealing duration, with the transition to three-dimensional (3D) island formation occurring as the WL thickness exceeded the critical threshold (h_c).
Following the formation of the WL, additional layers of InAs were deposited. The nominal thickness of these layers was carefully controlled to approach the near-critical nucleation regime, achieving low-density QD arrays with tunable densities ranging from 10^7 to 10^9 cm^{-2}. To further refine the QD properties, the growth process was interrupted by stopping the trimethylindium (TMIn) flux while maintaining the AsH_3 flux, enabling controlled QD size and morphology. These QDs are randomly distributed within a 580-nm-thick InP layer, which is used as the basis for creating InP WGs. In this process, the positions of the QDs are not controlled in relation to the waveguide axis. Additionally, an InGaAs etch stop layer is introduced between the InP slab and the underlying InP substrate. In general used quantum dots exhibited sharp, well-isolated photoluminescence peaks in the telecom C-band.

Concurrently, Si WGs and alignment marks (AMs) are patterned using ultra-violet (UV) optical lithography in a positive-tone photoresist on top of the 220-nm-thick Si layer of a standard SOI chip (Fig. 3.6). The Si WGs are defined by two 10 µm-wide openings that also act as efficient vertical out-gassing channels to facilitate high area bonding [190].

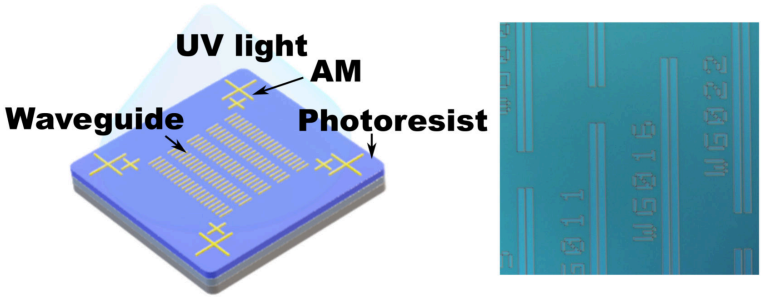

FIGURE 3.6: Photolithography of SOI chip and on the right positive photoresist patterned on the SOI wafer [22].

Simultaneously, silicon WGs and alignment marks (AMs) are fabricated on the 220-nm-thick silicon layer of a standard SOI chip using ultraviolet (UV) optical lithography with a positive-tone photoresist (see Fig. 3.6). The silicon WGs are shaped through two 10 µm-wide openings, which serve a dual purpose by also functioning as vertical out-gassing channels to enhance the bonding area efficiency [190].

The design is etched into the silicon layer using inductively coupled plasma advanced oxide etching (ICP-AOE) (see Fig. 3.7). Following this, the surfaces of the flipped InP chip and the silicon layer undergo an oxygen plasma treatment to enhance the concentration of hydroxyl groups, which play a key role in forming bonds at the interface [191, 192].

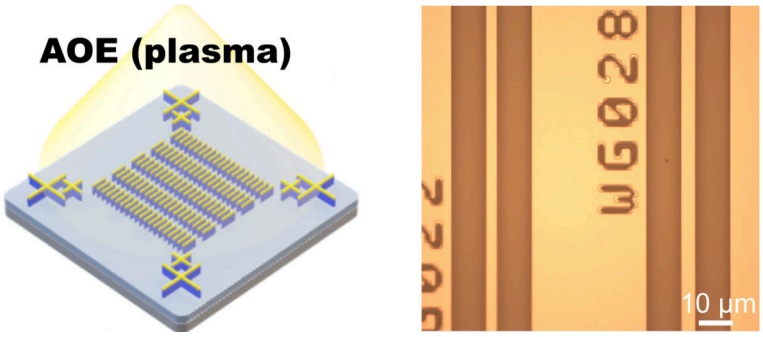

FIGURE 3.7: Etching of SOI chip [22].

In the fabrication process, a quarter segment of a 2-inch InP wafer was bonded to an SOI chip, which was cut from a complete SOI wafer to align with the shape of the InP quarter. Right after low-power plasma ashing, the surfaces are brought into direct contact under high pressure (approximately 2 kN) and elevated temperature (250 °C) within a vacuum environment inside the bonder. The sample is held under these conditions for 60 minutes before the temperature is gradually reduced. This process achieves a robust bond between the InP and Si layers without the need for an intermediate material (see Fig. 3.8), resulting in a typically high bonding yield exceeding 70 %, as assessed on a quarter segment of a 2-inch InP wafer.

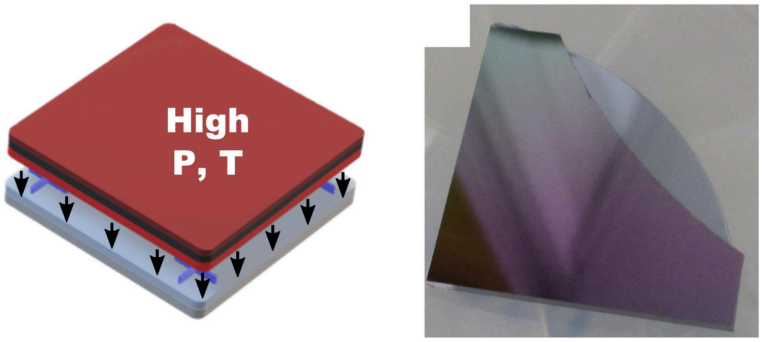

FIGURE 3.8: Direct bonding, a segment of a 2-inch InP wafer (partially seen at the bottom) is bonded to the SOI chip, which is visible at the top with its backside exposed [22].

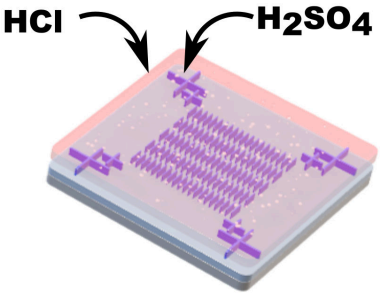

FIGURE 3.9: InP substrate removal [22].

The InP substrate is dissolved using hydrochloric acid (HCl), while the etch stop layer is removed with a solution of sulfuric acid and hydrogen peroxide (H_2SO_4:H_2O_2), as illustrated in Fig. 3.9. This step allows for removal of the origin InP substrate leaving only thin layer with QDs.

Extra fabrication steps are implemented to ensure precise alignment of InP nanobeam waveguides over the silicon waveguides during the electron-beam lithography process. Initially, the alignment marks (AMs) patterned in the SOI layer are exposed. This is followed by defining openings in the InP layer using ultraviolet (UV) lithography, as depicted in Fig. 3.10.

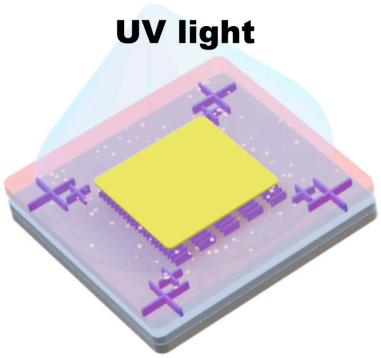

FIGURE 3.10: Revealing of AMs [22].

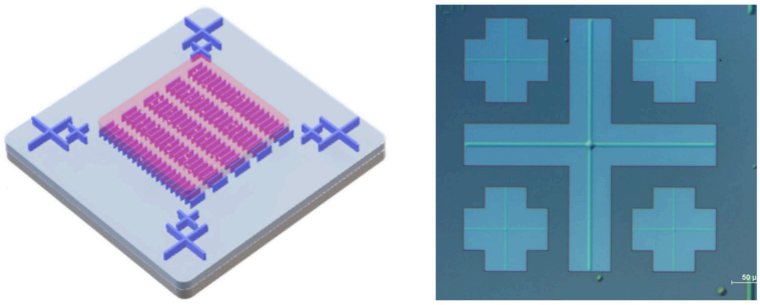

FIGURE 3.11: Selective InP wet etching [22].

Subsequently, the pattern is transferred through etching with HCl, as shown in Fig. 3.11. On the right is a patterned positive resist which covers the semi-transparent InP membrane, ready for wet etching to expose the alignment marks (AM) in the underlying silicon layer.

Electron-beam lithography with high-precision alignment (around 40 nm) [193] employing hydrogen silsesquioxane (HSQ) negative tone resist is utilized to define the InP nanobeam waveguides and outcouplers, which are accurately placed over the silicon waveguides (see Fig. 3.12).

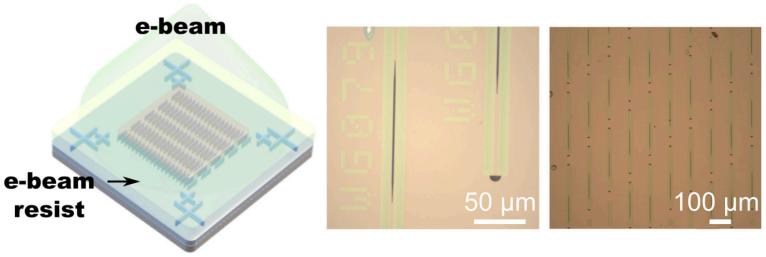

FIGURE 3.12: E-beam lithography, on the right negative resist exposed after electron beam lithography for shaping the InP waveguides [22].

The design is etched into the InP layer using hydrogen bromide (HBr) plasma with inductively coupled plasma reactive ion etching (ICP-RIE). The HSQ mask is then stripped away using buffered hydrogen fluoride (BHF), as shown in Fig. 3.13.

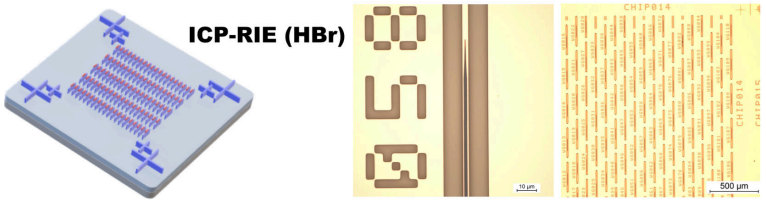

FIGURE 3.13: Etching of InP, on the right the SOI wafer with InP waveguides after ICP-RIE etching, displaying the fabricated structure [22].

Fabrication workflow

The fabrication workflow is summarized in Tab. 3.1.

Step	Equipment	Procedure
Surface preparation	Oven: HMDS	HMDS deposition
Spin coat resist	Spin coater	
SOI exposure	MLA	Expose pattern: 405 nm
Development	Manual developer	
Inspection	Optical microscope	Inspect pattern and alignment marks
Descum	Plasma asher	10-15 s oxygen plasma ashing, Removing residual resist
Si etching	AOE	Transferring pattern by etching Si down to SiO_2 (220 nm)
Mask removal	Fume hood	Remover1165 in ultrasonic batch (over 30 min), IPA rinse,
Plasma activation	Plasma asher	30s and 300 $\frac{ml}{min}$ O_2 flow at 400W
Bonding	Wafer bonder	Pressure 5 Bar
InP substrate removal	Fume hood	HCl 70 min batch, risne with DI
InGaAs removal	Fume hood	H_2SO_4:H_2O_2=1:1 30s, risne with DI, N_2 blow dry
Spin Coat resist	Spin coater	Resist AZ 5214E 1.5 µm
SOI exposure	MLA	Uncover Si Aligment marks
Descum	Plasma asher	10-15s oxygen plasma ashing, removing residual resist
Aligment marks reveal	Fume hood	InP wet etching, H_2SO_4:H_2O_2=1:1 30s, risne with DI, N_2 blow dry
Mask removal	Fume hood	Remover1165, IPA rinse, DI rinse, N_2 blow dry
Pretreatment	Spin coater	Resist: HSQ
E-beam exposure	E-beam writer	Use aligment
Development	E-beam fumehood	AZ400K:H_2O = 1:3 for 2 min 40 s, DI water: risne N_2 blow dry
InP dry etching tapers	ICP etch	
Resist strip	Fume hood	BHF 2 min, DI Risne, N_2 blow dry
Cleave the wafer	Fume hood	Cleave the wafer perpendicularly to the SOI waveguides

TABLE 3.1: Procedure used to fabricate structures described in this chapter.

SEM characterization

To evaluate the processing accuracy, the fabricated hybrid InP/Si waveguide structure was examined using SEM. A representative micrograph of the on-chip microstructure is displayed in Fig. 3.14. It illustrates a single device showcasing the hybrid (InP/Si) WG section, a silicon WG segment, and the circular Bragg grating outcoupler on the right side, while the left side terminates with a cleaved facet. To showcase the cleaved edge and an outcoupler simultaneously, the image was composed of two SEM images and false-colored to highlight the contrast between InP and Si. The rectangular etched region in Si is also presented. The SEM images indicate high-quality fabrication and precise alignment of the InP WG integrated onto the Si WG, with a positioning error estimated to be less than 100 nm. However, there are minor deviations from the design specifications: the InP WG width was approximately 50 nm narrower, and the Si WG width was about 150 nm narrower, attributed to differences in dry etching processes. These discrepancies were assessed on the basis of median values.

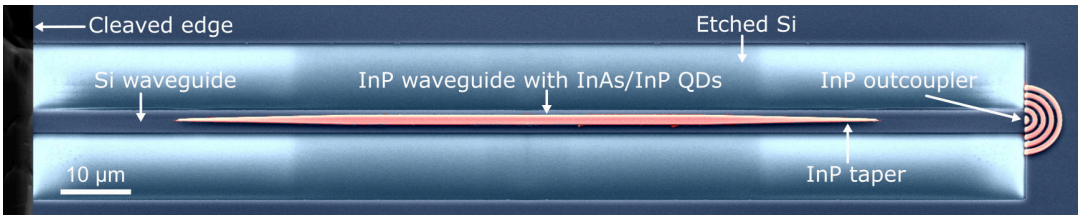

FIGURE 3.14: SEM micrograph of a top view of an exemplary fabricated structure. In the middle, there is a hybrid InP/Si waveguide structure with an InP grating outcoupler on the right and a cleaved edge on the left. This arrangement allows for studying optical properties od the structure from the 3 different spots (middle, cleaved edge, and the outcoupler) [22].

Figure 3.15 presents SEM micrographs of an InP outcoupler made up of InP rings positioned on a planar silicon section, specifically featuring half of a circular Bragg grating (CBG). The lower micrograph offers a closer, detailed view of the CBG outcoupler. Alternatively, a similar configuration having higher outcoupling efficiency could be fabricated entirely in silicon, necessitating an extra e-beam lithography process. The CBG grating design features 5 periods, with each ring having a width of 0.7 µm and a grating period of 1.2 µm. Their fabrication in the InP layer is a compromise. It allows for skipping the e-beam lithography step, which otherwise makes the fabrication process complicated.

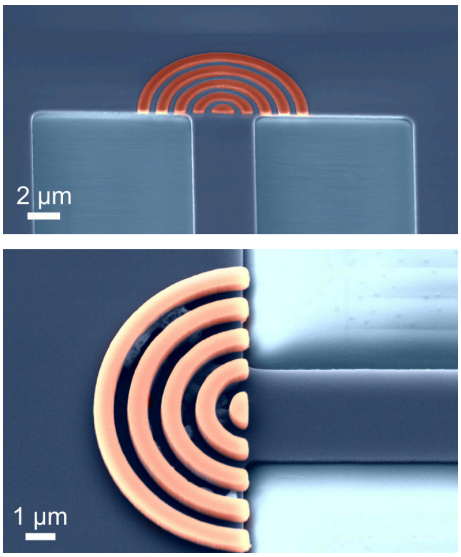

FIGURE 3.15: SEM images of InP circular Bragg grating forming an outcoupler [22].

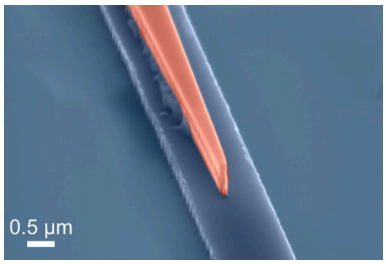

FIGURE 3.16: A linear taper of the InP waveguide on top of the silicon waveguide [22].

The InP taper geometry was restricted to 25 µm in length, having a finite tip width of 250 nm. A larger taper length exceeding 25 µm is not needed because, in the simulation, there can be seen the saturation of light transmission to Si [189]). As seen on the SEM micrograph unveiling the taper (Fig. 3.16), its edges are smooth, indicating that the dry etching step is well optimized.

3.2.1 Optical characterization

To optically characterize the fabricated devices, the experimental setups described in Sec. 1.7.1 and Sec. 1.7.2 were used. As seen in Fig. 3.13 on the right, the waveguides were prepared in a way (skewed pattern) that after cleaving of the chip, there would be a high probability that at least some of the Si waveguides end at the cleaved edge, giving access to the outcoupled light field after its passing through the waveguide. The linear density of the waveguides is about 20 devices per 1 mm. The wafer quarter visible in Fig. 5.11 was cleaved into multiple chips, and approximately 100 individual devices were checked. There were multiple criteria for a suitable device selected for further experimental studies, i.e.:

- The InP waveguide should have exactly one QD along its volume - this would allow to exclude spectral overlap of a signal from multiple QDs. Since the growth mode of the QDs resulted in their low surface density (with an average 430 nm dot-to-dot separation), a more common situation was that there was no QD in an InP waveguide.
- Operation in the C-band - for the applications described in the Chapt. 1, the operation near 1550 nm is desired to hold the compatibility with the low-loss silica fiber transmission window.
- Bright emission - the intensity of the signal in terms of photon counts per second has to be high enough since after the generation of photons in a QD, they have to be transferred through multiple components: from InP WG to Si WG and then outcoupled (through grating outcoupler or from the edge) and processed in e.g. HBT setup.

As a result, about 4% of the devices have shown the required criteria and were selected for further experiments.

3.2.1.1 Normal configuration

Figure 3.17 presents the result of the microphotoluminescence experiment performed as a function of excitation power at a temperature of 5 K for one of the selected devices. In this case, the µPL experiment configuration employs the same excitation and detection path, aligned parallel to the WG surface (normal direction). The width of the InP WG for this device is 2.95 µm, and the width of the Si waveguide is 4.85 µm. The spectrum was recorded at various excitation power densities (saturation power $P_S = 7\mu W$) along the straight section of the hybrid WG, revealing inhomogeneously broadened emission lines within the 1530-1553 nm range. The linewidth (taken as FWHM of a Gaussian fit) of the 1537 nm emission line marked as an exciton is measured to be (197 ± 40) µeV, which is narrower than the 340 µeV linewidth observed in similar QDs from an unprocessed sample [194]. This linewidth improvement may be attributed to reduced charge fluctuations near the QD, which influence spectral diffusion, as lower excitation power densities are applied in the structured system.

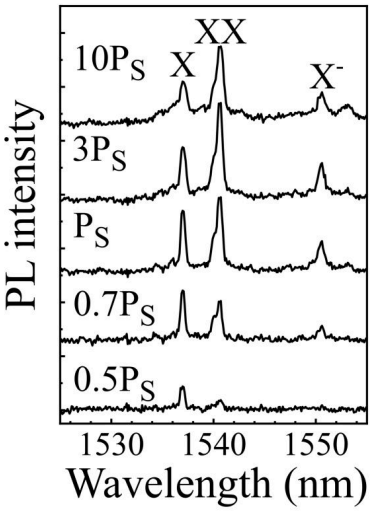

FIGURE 3.17: µPL spectra from the investigated InAs/InP QD embedded in a InP waveguide of 2.95 µm width at 5K. X - Exciton, XX - biexciton, X^- - negative trion. Spectra for different excitation power range from 3.5 to 70 µW [22].

Additionally, no QD blinking was detected. Based on previous studies of InAs/InP QDs [46, 71, 195] and analysis of the intensity dependence of the emission lines, these spectral features are assigned to recombination processes involving neutral exciton (X), biexciton (XX), and negatively-charged exciton (X^-) complexes confined within a single InAs QD embedded in the InP WG. In particular, apart from the described lines, the µPL response did not exhibit any additional spectral lines in the C-band when the excitation spot was scanned along the WG, indicating the absence of other optically active QDs that emit within the targeted spectral range of the device.

3.2.1.2 Orthogonal configuration

To demonstrate photon coupling from the QD to the SOI platform, we compared QD spectra obtained using the standard µPL excitation-detection configuration (as described in the previous section) with spectra recorded using two new experimental configurations, where the excitation and detection paths are spatially separated. In both new configurations, excitation is performed perpendicular to the InP waveguide (normal direction). At the same time, detection is carried out either via the outcoupler or the cleaved facet of the chip, as illustrated in Fig. 3.18. The new setup configuration uses an additional microscope objective in a detection path to collect photons from the outcoupler in the perpendicular direction and the cleaved facet of the Si waveguide in the in-plane direction of the chip (the so-called perpendicular configuration described in Sec. 1.7.2)

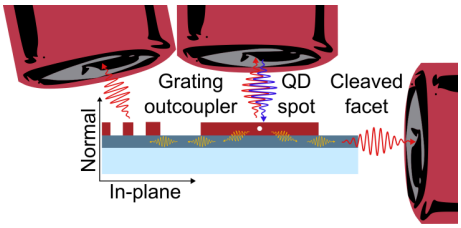

FIGURE 3.18: This orthogonal configuration with 3 microscope objectives is described in more details in Sect. 1.11 [22].

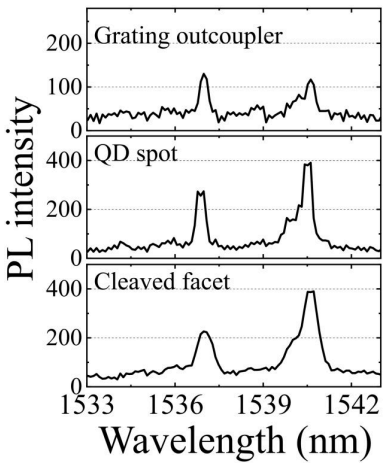

FIGURE 3.19: µPL collected using three different collection paths [22].

The emission from the QD was gathered using three different setup configurations (keeping the excitation through normal direction). As can be seen in Fig. 3.19, all registered spectral patterns exhibit qualitative consistency in terms of the spectral position of emission lines and their broadening. For the detection path at the CBG outcoupler, QD-emitted photons must travel approximately 80 µm, spanning the distance between the InP WG and the CBG, before being scattered and collected by the objective, proving qualitatively on-chip coupling of the light field between photonic components.

Figure 3.20 presents a qualitative comparison of the µPL intensity collected from the grating outcoupler, directly at the QD location, and from the Si WG cleaved facet (in-plane direction). The data were taken from the PL peak intensity displayed in Fig. 3.19 and plotted at the background of photon extraction efficiency estimated from the numerical simulation with the FDTD framework. Both the qualitative and quantitative agreement can be seen, with the highest collection efficiency from the cleaved facet, which is a direct proof of efficient coupling of QD emission to the Si WG. In contrast, in case of scattered light from the InP taper end, the collection from the cleaved facet would be strongly suppressed (FDTD simulations show 5̃% [22]).

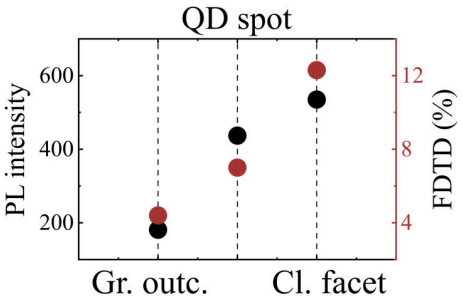

FIGURE 3.20: Comparison of experimental results from the three collection spots with FDTD simulations [22].

3.2.1.3 Single-photon measurements

Both extraction efficiency and single-photon emission purity measurements require a detector capable of sensing single photons, i.e. counts per second generated by every incoming photon. The former experiment was performed using pulsed excitation, while the latter was performed using continuous-wave excitation.

Extraction efficiency

A different waveguide was selected for single-photon emission purity measurement and extraction efficiency evaluation. The resultant spectra can be seen in Fig. 3.21 (a). The spectral lines from QD emission are similar to those previously identified for another waveguide and presented in Fig. 3.17. Identification of the emitted complexes was based on the power series seen in Fig. 3.22 and the information on charged-exciton and biexciton binding energy expected for InAs/InP QDs.

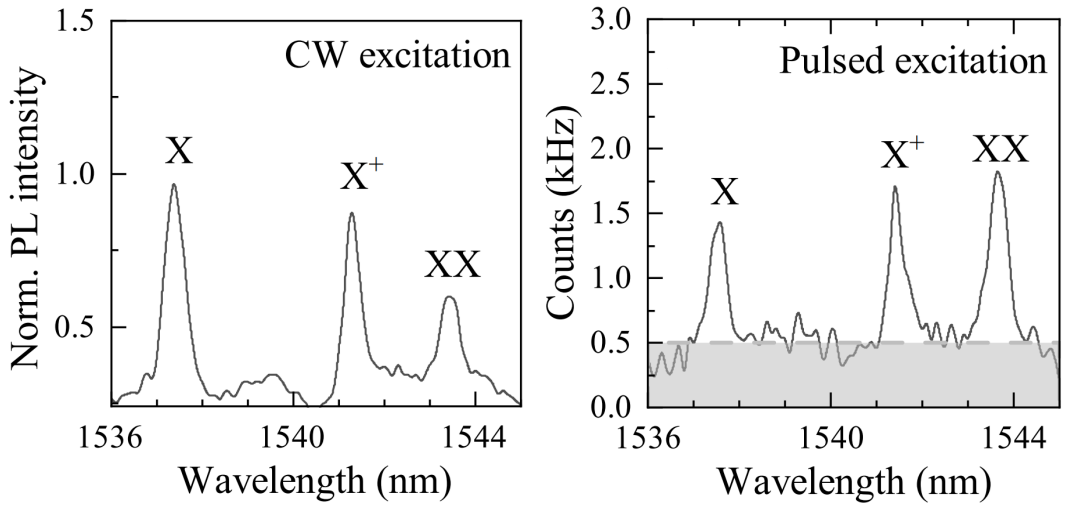

(a) Continuous wave excitation of a QD in an InP WG with a 660 nm laser.

(b) Pulsed excitation of a QD in an InP WG with a 805 nm laser.

FIGURE 3.21: Non-resonant micro-photoluminescence experiment with identified excitonic complexes (X, X^+, XX) measured with a monochromator and a CCD camera - (a), and fiber coupled and dispersed on a tunable filter and detected by an SNSPD detector - (b). The grey area in (b) depicts the background photon noise contribution (500 counts/s). The detected count rates for the lines X, X^+, XX amount roughly to 1000, 1400, and 1500 counts/s, respectively (without background contribution). Both spectra are collected from a cleaved facet of the Si waveguide [22].

The measured extraction efficiency can be lower than the value calculated using numerical methods due to several technological factors, i.e.:

- misalignment of the QD relative to the InP WG axis - due to the non-deterministic nature of the fabrication process - the position of a QD can be off center, which leads to reduced coupling of QD emission into propagating modes of the waveguide [189].
- misalignment of the InP WG relative to the Si WG - it leads to the reduced on-chip coupling between these WGs, albeit as seen from the SEM micrograph in Fig. 3.14, the positioning uncertainty is estimated to be below 100 nm.
- structural irregularities along both the InP and Si waveguide sections, imprecise taper shaping near the tapered tip, or edge roughness from cleaving the sample - it leads to lower photon collection efficiency from the cleaved facet (simulations predicted 89%).
- non-radiative recombination within the QD - it decreases the internal quantum efficiency [196–198].

As a consequence of varying carrier kinetics for different exciton complexes, we have obtained linear scaling factors of the emission intensity from an exciton and a positively charged exciton ($I \propto P^1$) and superlinear (near quadratic) for XX, as

expected [72, 73]. In Fig. 3.22, there are presented power-dependent microphotoluminescence experiments taking into account QD emission lines shown in Fig. 3.21.

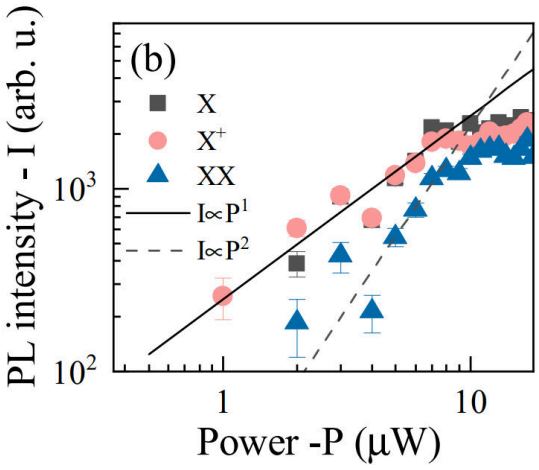

FIGURE 3.22: Log-log plot of μPL intensity versus excitation power for the lines presented in Fig. 3.21. The symbols are experimental data points, while the solid(dashed) line shows linear(quadratic) fit to the data [22].

As described in Sec. 5.11, to calculate extraction efficiency in pair with the measured spectra under pulsed excitation, there is a need to include losses in the optical setup. Table 3.2 shows the efficiencies of the optical components used and the estimated total setup efficiency. These efficiencies of the elements were obtained using a power meter and a tunable continuous-wave laser source (Toptica DLC Pro) set to 1540 nm to match the exciton transition. The total setup efficiency is a product of the elements' efficiency, and its uncertainty was calculated using the uncertainty propagation method.

Multimode - single-mode coupling

As revealed by the FDTD simulations [189], the hybrid InP/Si WG is unavoidably multimode. In our experimental setups, the source of the highest losses is light field coupling between the multimode Si WG on-chip and a single-mode fiber outside of a cryostat. As described in the fabrication section, multiple devices were fabricated. Still, the highest probability of finding a QD in an InP waveguide was for the largest InP waveguides (width of 2.95 μm). This corresponds to the increase of the Si waveguide size (width of 4.85 μm), which for this size operates as a multimode. In the detection path, standard SMF-28 single-mode fiber was used.

The multimode(MM) - single-mode(SM) coupling was determined experimentally. The coupling efficiency was estimated by coupling the continuous-wave laser of a 1540 nm photon wavelength into the Si WG on a chip. The light transmitted from the waveguide edge was first guided into a multimode optical fiber, with the intensity measured using an InGaAs CCD camera, establishing a baseline reference. Next, a SM fiber replaced the MM fiber, and the intensity measurement was repeated. The coupling efficiency was determined by comparing the photon counts

from these measurements to the reference counts. Using the reference as a benchmark of 100%, the coupling efficiency with the SM fiber was estimated to be 1%. It is important to note that this is a rather upper boundary since coupling to the MM fiber was assumed to be 100% efficient.

TABLE 3.2: List of components used to measure extraction efficiency. In the second column, the efficiency of a component with measured concentricity is shown. Two last rows are the values of the calculated extraction efficiency [22].

Element	Efficiency
Cryostat window	90(2) %
Microscope objective	40(3) %
MM/SM Coupling	1.0(1) %
Fibers and fiber connectors	61(10) %
Monochromator	60(5) %
SNSPD	87(3) %
Total setup efficiency	0.115(26) %
Extraction efficiency (one direction)	5.1(11) %
Extraction efficiency (both)	10.2(21) %

Single-photon purity

As a last experiment for this sample, the second-order auto-correlation measurements using the Hanbury-Brown and Twiss setup were performed. For more details on the experimental setup and autocorrelation measurement, see Sec. 1.5.5.1, 1.7.1, and 4.1.2.1. The QD emission was collected from the cleaved facet of the device, with continuous-wave laser excitation applied from the top to the QD location. The neutral exciton emission was selected from the measurements shown in Fig. 5.11. The autocorrelation measurement conditions optimized for the signal-to-background ratio enabled recording of histogram counts, which undoubtedly display the antibunching minimum presented in Fig. 3.24.

Moreover, there was not observed any bunching at time delays near the antibunching minimum, suggesting a low likelihood of QD re-excitation caused by recapture processes of carriers trapped in nearby charge traps that may occur immediately following recombination of an excitation in a QD [199, 200]. The measured rise time of 590 ± 120 ps indicates a relatively high effective pump rate (laser excitation power) [71] and aligns with previous findings for these QDs [194]. The influence of background emission on count rates can be accounted for using the formula [201]:

$$g^{(2)}_{corrected}(0) = \frac{C_N(\tau) - (1-\rho^2)}{\rho^2} \tag{3.1}$$

where $\rho = \frac{S}{S+B}$ in which S and B represent the signal and background count rates, respectively. The $C_N(\tau)$ represents the observed coincidence count normalized to the theoretical coincidence count expected from a Poissonian source of equivalent intensity. For the exciton line presented in Fig. 3.21, the ρ value is 0.75.

Figure 3.23 presents a contour plot originating from the analysis of equation 3.1. The white dashed line denotes the boundary region, where the $g^{(2)}_{corrected}(0) = 0$. This line gives the upper uncertainty value for $g^{(2)}_{corrected}(0)$, which implies that to increase the accuracy of the estimation of the single-photon purity, the signal-to-noise ratio has to be increased.

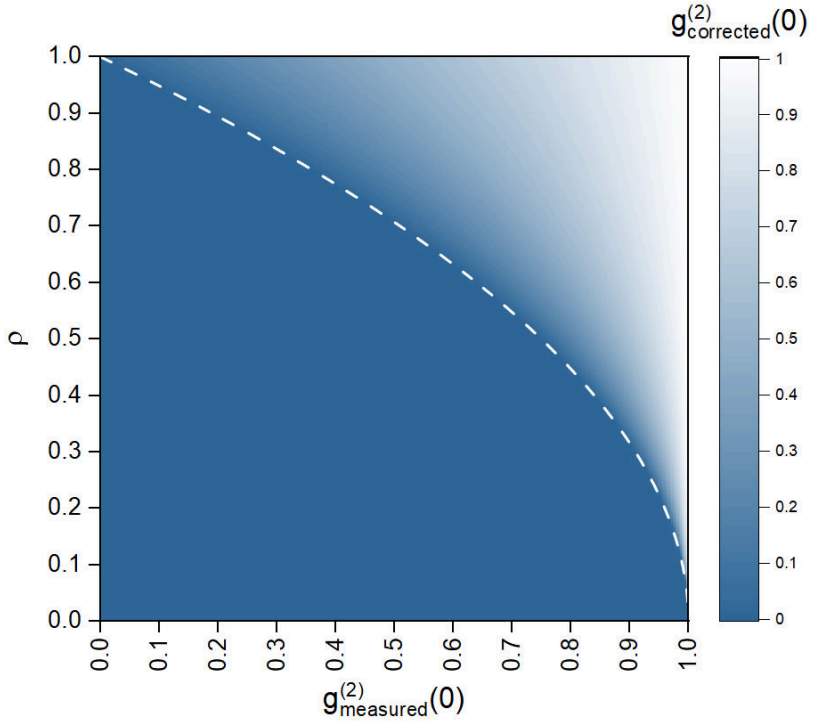

FIGURE 3.23: A contour plot generated using Eq. 3.1, with measured, corrected second-order correlation function, and signal-to-noise ratio. Published in ref. [22].

The background counts at a level of 0.5 kHz (visible in Fig. 3.21) are the primary source of the multiphoton events, and Fig. 3.24 has this background subtracted. This leads to the value of $g^{(2)}(0) = 0.02$, which reflects the high purity of sphotons propagation on-chip. Without this background subtraction, the fitting procedure yields the value of $g^{(2)}_{fit}(0) = 0.17(12)$, also proving the single-photon emission of the source.

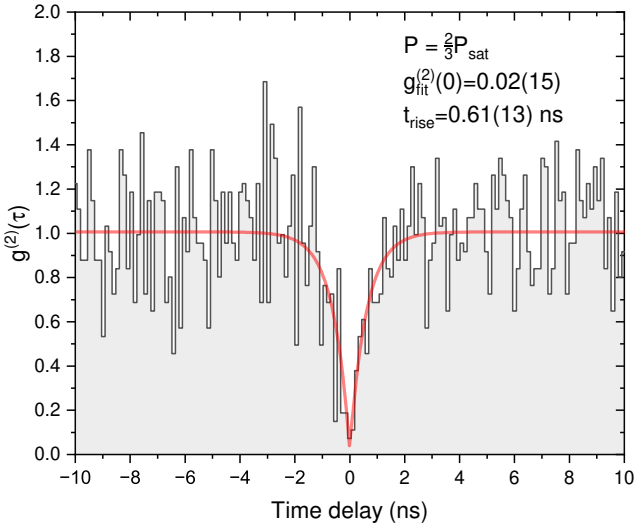

FIGURE 3.24: Auto-correlation histogram of the natural exciton emission from the QD, measured under CW excitation from the cleaved edge of the device. The saturation power is 7 µW. The solid red line represents a fit to the experimental data. From this histogram, there was subtracted background emission with energy matching that of the observed transition [22].

3.2.2 Conclusions

In this chapter, fabrication steps for direct heterogeneous integration and optical characterization of InAs/InP-QD-based single-photon emitters coupled with the SOI chip were outlined, which is a highly relevant technological advancement for quantum photonic integrated chips. The presented direct bonding method allowed for wafer-scale integration and is not limited to the SOI platform.

The direct bonding process supported by lithography steps allowed one to successfully define essential building blocks of a quantum photonic integrated chip, namely a single photon emitter inside the InP waveguide placed on the Si waveguide, allowing for photon transfer between a QD and the SOI chip interior, and the photons outcoupling. Within the presented approach over the 70% of the chip area was successfully directly bonded giving high yield of this process. The out-coupling interface, responsible for photon exchange between a chip and its external environment, comprises half of a circular Circular Brag Grating. Such a specified quantum device was optically evaluated to establish some critical parameters, including photon emission wavelength, the on-chip directional photon coupling, and the photons outcoupling off the chip.

The optical properties of the device were determined using microphotoluminescence experiments at the cryogenic temperature, where the QD emission efficiency was the highest. The standard setup has been upgraded, allowing for evaluation

of the device parameters by examining photons transmitted through the chip interior. In this way, the QD-confined electronic states have been identified as either neutrally charged exciton, biexciton or charged-exciton, providing single photons to the chip within the telecom C-band spectral range. The background-corrected single photon generation purity was determined to be 98%. Finally, the on-chip directional coupling of photons from the QD to the Si chip was estimated to be roughly 5.1%.

The fabrication methodology presented in this chapter can be applied to other materials utilized in photonics, such as silicon nitride and lithium niobate, enabling scalable technology. The device fabrication yield can be increased by localizing the QDs prior to the definition of the InP waveguide [101], and their fabrication can be carried out around the localized QD. It gives additional advantages, enabling precise shaping of the QD environment to boost the QD emission properties.

Chapter 4

Heterogeneous III-V integration on fiber with micro-transfer printing

This chapter presents a technological advancement of fiber-integrated quantum dot-cavity systems operating in the telecom C-band. The sample fabrication section describes a micro-transfer printing technique which was applied to the deterministic integration of InAs/InP quantum dots coupled to a photonic crystal cavity of H1 type with a standard telecom single-mode fiber. Such a device was optically characterized at cryogenic temperatures. It shows stable single-photon emission examined through a standard telecom fiber and the all-fiber setup located at a distant node. Therefore, this demonstrates the capability of such a device to be used in the quantum communication between distant nodes of the silica fiber network. This work aligns with the motivation of developing QKD systems by demonstrating more applied quantum technology.

4.1 Sample fabrication

The InAs/InP quantum dot structure used for this study was grown by a metalorganic vapor-phase epitaxy (MOVPE) [45, 194] in the Stranski-Krastanov growth mode. The growth details are presented in Chapter 3. The growth process involves depositing a 500 nm InP buffer layer, a 200 nm $In_{0.53}Ga_{0.47}As$ sacrificial layer, and a 244 nm InP layer on a (001)-oriented InP substrate at 610 °C. Subsequently, the 0.93-monolayer-thick InAs was deposited, leading to the formation of high-density QDs. The 244 nm-thick InP capped the dots. Next, a 500 nm-thick SiO_2 release layer was deposited by PECVD, followed by a 120 nm Al layer deposition using an e-beam evaporator. These layers serve two purposes: separating the device from the source wafer after etching and facilitating 2D imaging through the transparent SiO_2 at 1.55 µm [101]. The wafer with the Al on top was then spin-coated with BCB and bonded after flip chip to a Si wafer under vacuum and high force (2 kN) at 250 °C. The InP substrate and $In_{0.53}Ga_{0.47}As$ layer were subsequently removed using HCl and (10 %)H_2SO_4:H_2O_2, respectively [46]. A 96 nm-thick SiN layer was deposited on the InP membrane, acting as an electron-beam lithography mask and a stress management layer by inducing tensile stress.

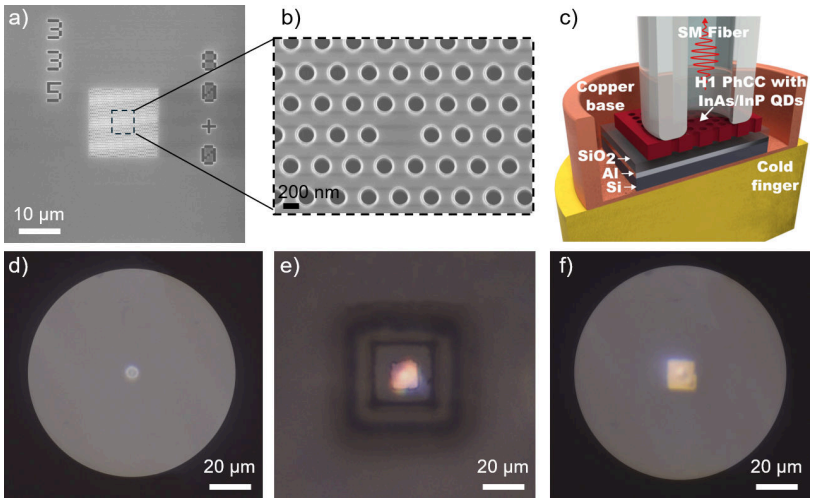

FIGURE 4.1: Integration process of a single 2D photonic microstructure into a cleaved single-mode fiber. a)-b) Scanning electron microscope (SEM) images of an H1 2D PhCC before the membranization process. c) Schematic depiction of the cross-section of the fabricated device. d) A fiber core before the micro-transfer process of the cavity. e) Coupon with the cavity on the PDMS stamp during the transfer procedure. f) The cavity structure after transferring on the fiber core.

A series of H1 point defect 2D PhC cavities were patterned using electron beam lithography. The cavities varied by the hole radii (80 nm, 100 nm, 120 nm) and lattice constants (335 nm to 435 nm in 10 nm steps). After dry etching of InP with HBr using inductively coupled plasma reactive ion etching, the structure was membranized by removing the underlying SiO_2 release layer in a BHF wet etching process. Representative SEM images of the fabricated PhC cavities before membranization are shown in Fig. 4.1.

After the sample was membranized, a copy of the chip was characterized experimentally at DTU. The chip was placed in a setup allowing wide-band IR illumination with polarized light from SLED. The light reflected off a cavity was filtered by the polarization analyzer in an orthogonal configuration and measured using an optical spectral analyzer (OSA) (this technique is also known as resonance scattering). This setup allowed for the observation of the fano-resonance and an evaluation of the mode central wavelength with the cavity parameters. The results are demonstrated in Fig. 4.2. This information was crucial because only selected nanobeams with the mode spectral position near 1560 nm at room temperature were transferred by µTP to the fiber tip.

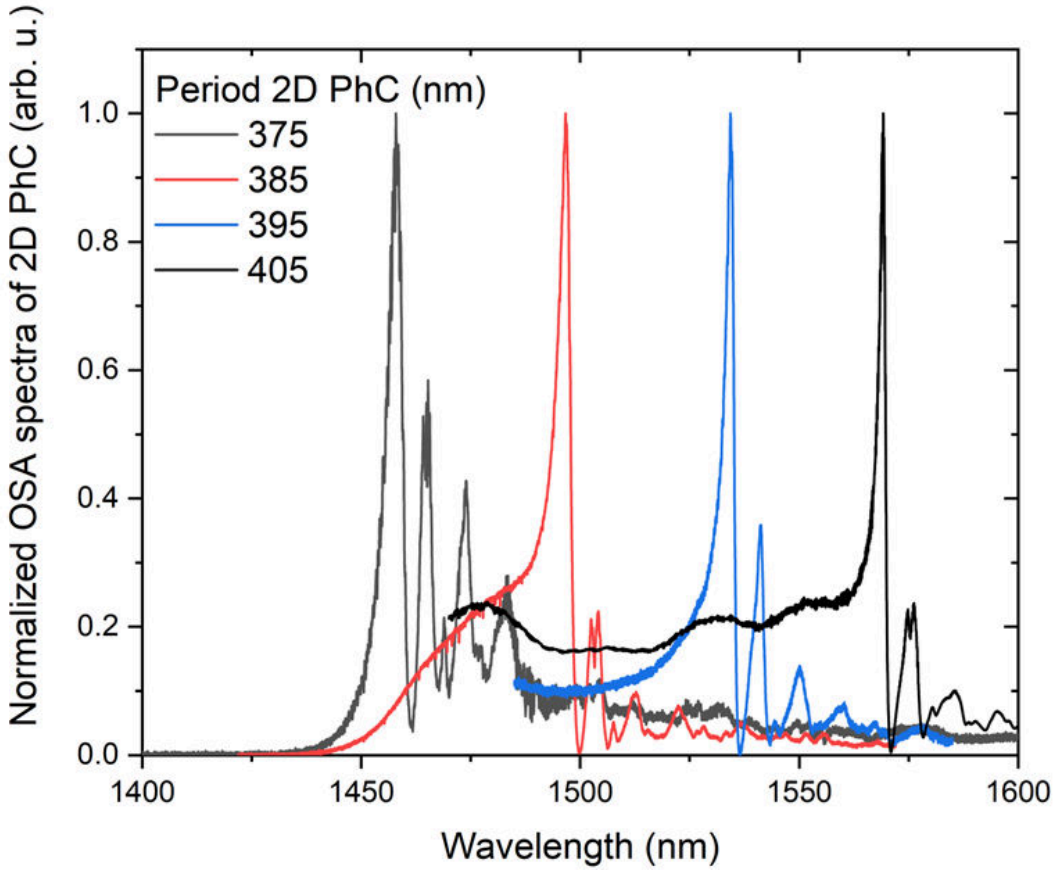

FIGURE 4.2: Measured fano-resonance for 2D photonic crystal cavities with a different lattice period. The resonance is visible, allowing for determining the fundamental cavity mode as a function of a lattice period. After a linear fit of the data, the equation is as follows: resonant wavelength = 3.71(6)*period (in nm) + 66(24) nm.

4.1.1 Micro-transfer printing parameters

For µTP picking, the parameters were experimentally tested within the following ranges: overdrive distance of 100–170 µm, acceleration of 0.4–0.7, overdrive speed of 20–32 $\frac{\mu m}{s}$, and pre-pickup time from 1 to 4 seconds. The optimal parameters for the presented structures were the following: an overdrive distance of 140 µm, acceleration of 0.7, an overdrive speed of 32 $\frac{\mu m}{s}$, and a pre-pickup time of 4 seconds. Excessive overdrive speed was observed to displace the coupon excessively (occasionally causing interference patterns to vanish and the coupon to darken - indicating contact with a substrate). Longer pre-pickup time appeared to allow sufficient adhesion time for the stamp. Furthermore, it was checked that the processes' yields increased if they moved from the critical speed, where for the highest acceleration $0.8\frac{\mu m}{s^2}$ and the slow print speed Y the yield was the highest.

4.1.2 Optical characterization

Initially, the device was examined under relatively high excitation power. Figure 4.3 a) displays room temperature QD ensemble emission and a cavity mode at 1573.4

nm. The spectral response was measured in the microphotoluminescence setup for one of a device. Figure 4.4 shows the spectral response of another device. It presents a group of sharp, inhomogeneously broadened lines identified as emission from single QDs. In addition, a sharp spectral feature below 1475 nm is observed (more pronounced at lower excitation power) attributed to the higher-order cavity mode emission. The temperature series shown in Fig. 4.3 a) demonstrates the QD emission shifted to shorter wavelengths mainly due to temperature-driven bandgap changes. The visible cavity mode blueshift of $\tilde{1}3$ nm is related to temperature-induced changes in the refractive index in the cavity material [202]. In addition, the mode quality factor increases with the drop in temperature from 620 to 750.

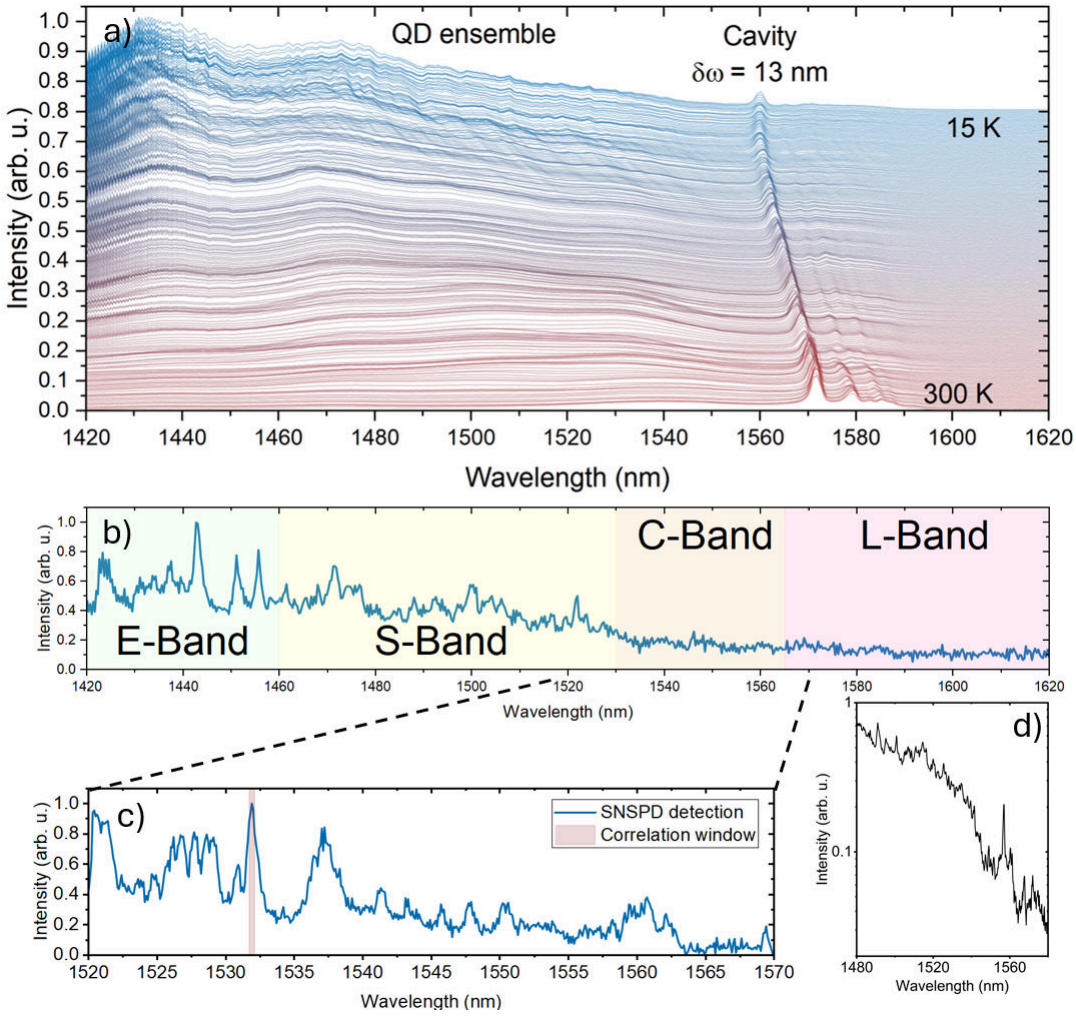

FIGURE 4.3: Photolumenscence spectra of the investigated devices. a) Temperature evolution of PL spectra for one of a device. Temperature ranges from 15 K to 300 K. The continuous-wave excitation power amounts to 500 µW (see also Sect. 1.7.3 for the more information about the experimental setup). b) PL spectrum from another device registered at 15 K and low excitation power (in the range of hundreds of nW). c) Spectra of the same device as in panel b) measured with the SNSPD detector and the all-fibre tunable spectral filter for higher resolution d) a second fabricated device with the transition on cavity mode with linewidth more than two times narrower than that of the cavity mode.

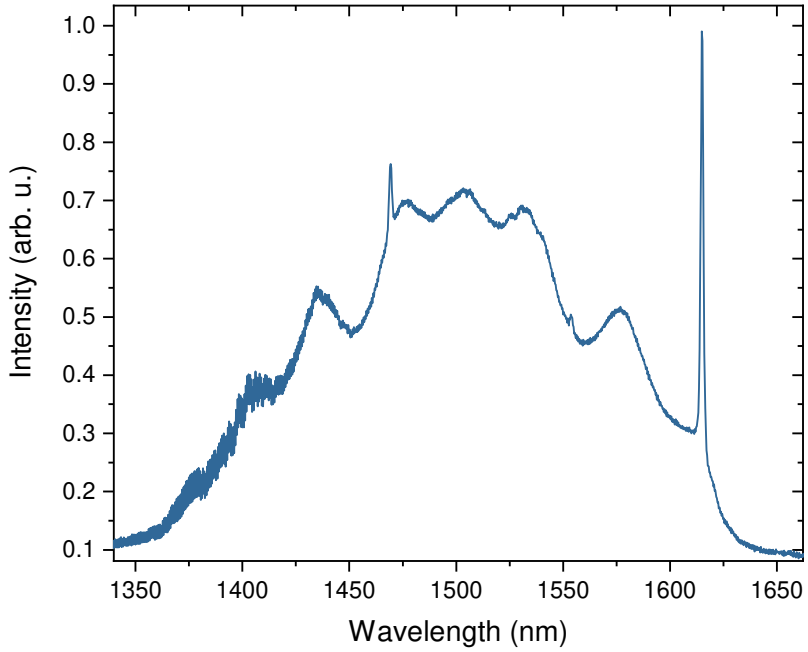

FIGURE 4.4: Emission spectrum of a fiber-integrated device with visible, prominent cavity mode at over 1600 nm and small intensity modes at lower wavelengths.

In the Fig. 4.3 b) there is a zoomed-in spectrum collected at 15 K along with highlighted telecom bands for standard optical fibers. To observe single QD-like transitions in the telecom C-Band, the average laser power before the cryocooler fiber feedthrough was reduced to 146 nW (in Fig. 4.3 b) the cavity mode is not visible due to much lower excitation power). The spectrum with focus on C-band was measured with the fiber-coupled setup equipped with an SNSPD detector and is shown in Fig. 4.3 c) and reveals a high density of quantum dots emitting numerous excitonic transitions overlapping with the strong background emission, which could also couple nonresonantly into the cavity's fundamental mode [203]. For comparison, in Fig. 4.3 d) there is presented a spectrum of a different device with a Purcell-enhanced QD transition on a cavity mode and its power series is shown in Fig. 4.5. The argument for the Purcell-enhanced emission is that this device exhibits a significantly narrower linewidth than the cavity mode, measured under higher excitation power than the device in Fig. 4.3 c) and additionally, it can be seen that it is composed of at least two Gaussians. Albeit its signal-to-noise ratio is lower than compared to the line highlighted in Fig. 4.3 c).

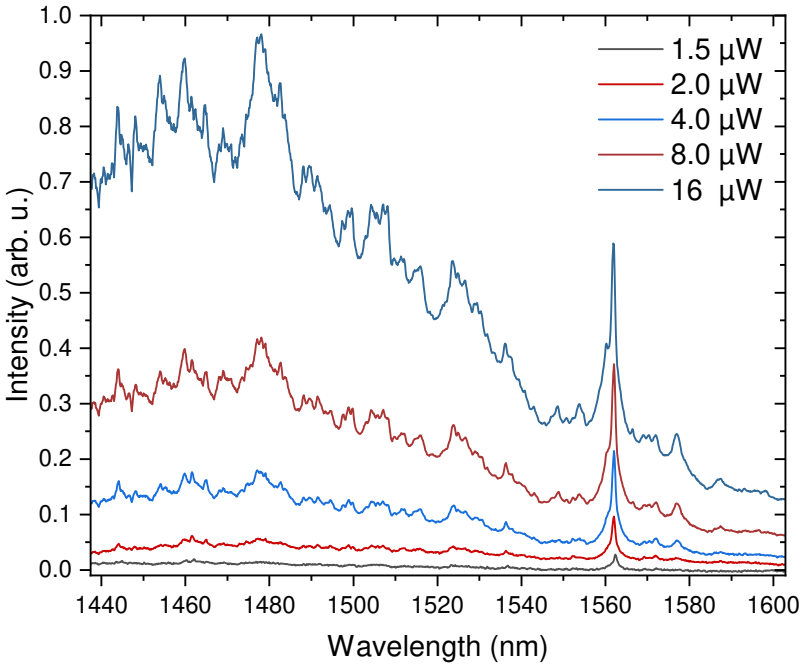

FIGURE 4.5: Excitation power dependence of the PL spectra of a high density InAs/InP QDs in a 2D H1 photonic crystal cavity. Detection was done on the monochromator at the excitation was the 660 nm cw laser.

4.1.2.1 Time-resolved measurements

The QD emission line at 1532 nm has been selected for time-resolved photoluminescence measurement. The line is displayed in 4.3 c). The selection criteria for the autocorrelation measurement was the relatively high intensity of the line compared to other lines visible in the registered PL spectrum, spectral location in the vicinity of the C-band, and a good signal-to-noise ratio, meaning a small contribution of the background emission to the registered photon counts. Interestingly, the chosen QD emission line aligns with the erbium(III) ion transition $^4I_{13/2} \rightarrow {}^4I_{15/2}$ [204, 205]. As typical for atomic systems, the erbium ion transition is expected to have a very long lifetime. Therefore, it can be considered the memory element for a photon state, which is important for storing quantum information. This transition has garnered significant interest due to its alignment with the telecom C-band and the silica-based fiber-optic communication systems. The line in Fig. 4.3 d) was unsuitable for single-photon emission analysis due to high background noise interfering with multiphoton events. A fabrication of a device with a lower density of QDs is expected to address this issue, enabling pure single-photon Purcell-enhanced emission from individual QDs. Non-resonant pulsed excitation was used to assess the lifetime of the 1532 nm QD line. The resultant time trace is presented in Fig. 4.6 b), exhibiting biexponential decay with fast and slow components, having a decay time of 0.9 ns and 6.6 ns, respectively. Considering typical InAs/InP QD ensemble lifetimes of around 2 ns [101, 194, 206], the short lifetime could be attributed to the QD

transition coupling with a higher-order cavity mode with a weak Purcell factor of approximately 2.

The purity of single-photon emission was evaluated in the HBT setup, using the same excitation scheme as for time-resolved photoluminescence. To mitigate the influence of the long-lifetime emission component, potentially originating from uncorrelated background emission [203], the HBT experiment was conducted with a laser repetition rate reduced to 40 MHz to prevent overlapping correlation peaks. The emission line was isolated using an all-fiber-based spectral filter, with the spectral range indicated by the pink area in Fig. 4.3 c). The collected histogram data were fitted using a periodic exponential decay function described in [207].

$$g^{(2)}_{fit}(\tau) = C_{bg} + g^{(2)}(0)e^{\frac{-|\tau|}{\tau_d}} + \alpha \sum_{n\neq 0} e^{\frac{-|\tau \pm nT|}{\tau_d}} \tag{4.1}$$

Figure 4.6 shows the measured histogram of coincidences with subtracted background contribution C_{bg}. The resulting data were fitted with a function where amplitude α is for pulses outside zero delay and a time constant decay of 2.2 ns. The fitted value of $g^{(2)}_{fit}(0)$ was determined to be 0.27(12). This measurement was performed near saturation power, enabling earlier observation of the $g^{(2)}(0)$ minimum due to the significant background emission. However, while the fitted $g^{(2)}_{fit}(0)$ value is relatively high, an excitation power reduction is expected to decrease $g^{(2)}_{fit}(0)$ [208]. Since $g^{(2)}_{fit}(0)$ does not vanish for pure single-photon emission, the background contribution to single-photon purity can be quantified using the following formula:

$$g^{(2)}_{corrected}(0) = \frac{C_N(\tau) - (1-\rho^2)}{\rho^2} \tag{4.2}$$

using the signal-to-background ratio, $\rho = (S)/(S+B)$ of 0.7 where S and B represent the signal and background count rates, respectively [201], and with $C_N(\tau)$ representing the normalized number of measured coincidences, the corrected value of $g^{(2)}_{corrected}(0) = 0.14(14)$ can be determined. This corrected value accounts for the absence of background contributions.

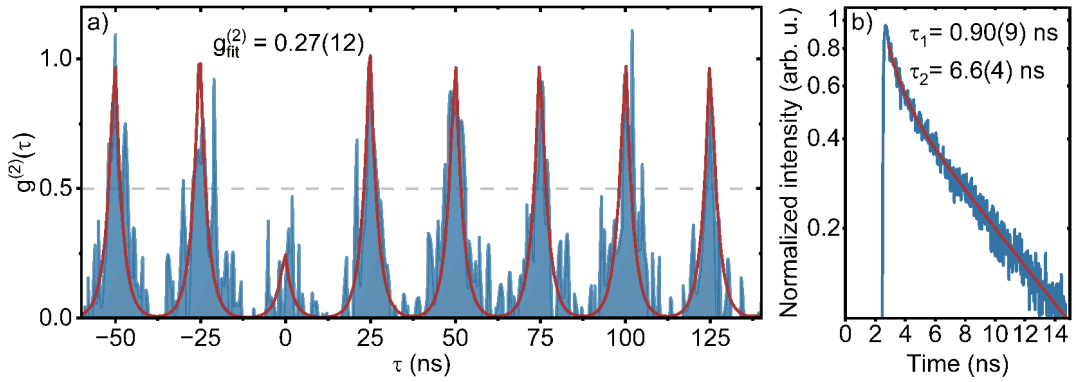

FIGURE 4.6: Time-resolved experiments a) Second-order autocorrelation measurement with pulsed (triggered) optical excitation of 146 nW and 40 MHz repetition rate with background subtracted. The dip at zero delay time confirms that the emitter is a single photon emitter. The blue curve represents experimental data and red lines correspond to fitting curves showing $g^{(2)}_{fit}(0) = 0.27(12)$. b) Decay profile of the quantum emitter emission within the same spectral window as for autocorrelation measurement. The decay curve is fitted using the double exponential function to estimate the decay constants - fast 0.90(9) ns and slow 6.6(4) ns.

The stability and operational readiness of a fiber-coupled QD source are essential for practical applications. Since the micro-transfer printed membrane is sub-micrometer in thickness and the whole device has 4 layers of different chemical adhesive, it could be highly susceptible to any mechanical and thermal stress shifting the membrane in respect to the fiber core. The stability of the device was assessed by monitoring the single-photon flux for over 40 hours. As shown in Fig. 4.7 a), the normalized intensity plot of the single-photon count rate reveals long-term fluctuations, potentially attributed to cryocooler thermal fluctuations or background variations due to the exposed fiber link in an open environment.

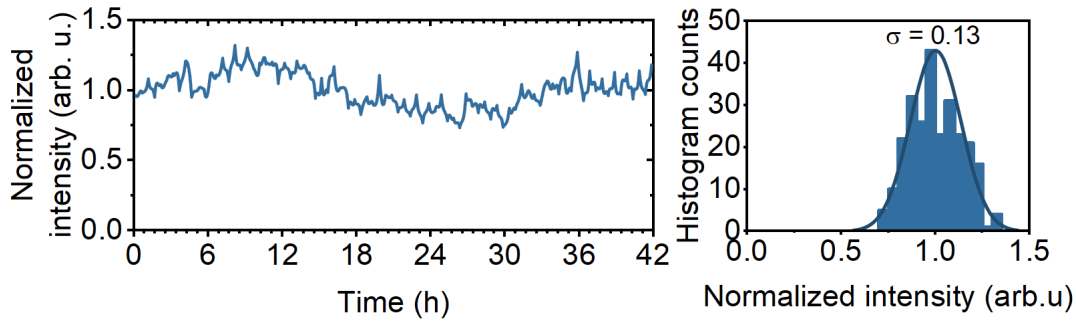

FIGURE 4.7: Evaluation of the device's long-term performance a) Plot of the normalized single-photon count rate of the device. Measured in the same configuration for which autocorrelation measurement was performed. b) Plot of a histogram of the normalized intensity showing the distribution of the signal intensity with a standard deviation value $\sigma = 0.13$. The calculated signal fluctuation without a long timescale component is reduced to $\sigma = 0.09$.

4.1.3 Conclusions

This chapter presents the design, fabrication, and optical characterization of a triggered, fiber-coupled QD-based single-photon source operating in the third telecom window. The source utilizes high-density InAs/InP quantum dots. To enhance photon coupling to standard single-mode fiber, an H1 point defect 2D photonic crystal cavity was used in combination with a metallic back reflector and a SiO_2 spacer layer. The device integration was achieved through a high-yield (near all of the cavities were successfully transferred to the fiber) and accurate micro-transfer printing technique. The device, when operated between two distant laboratories connected by commercial single-mode fiber, exhibited stable long-term coupled QD emission and reliable performance over multiple cooling cycles, demonstrating its robustness for practical applications. Single-photon emission characteristics reflect $g^{(2)}_{fit}(0)$ values of $0.27(12)$ and a background-corrected value of $g^{(2)}_{corrected}(0) = 0.14(14)$, proving antibunching in the generated stream of photons.

Moreover, the SiO_2 release layer and underlying metallic mirror used before transfer printing offer the potential for deterministic integration of single QDs in the photonic structure employing 2D microPL imaging [101]. This would enable the precise design of the cavity on a pre-selected QD to maximize coupling with the fundamental mode. However, it requires reduced QD density to provide successful preselection as well as to minimize background emission contributions, enhancing single-photon purity [209] . Furthermore, quasi-resonant excitation schemes can reduce background emission and improve single-photon purity [210]. Additionally, improved surface quality can enhance light coupling efficiency to the fiber [211]. Micro-transfer printing allows for real-time feedback during alignment and by observing the fundamental mode of the cavity through the fiber, the alignment process can be dynamically adjusted to maximize coupling efficiency.

This device successfully maintains single-photon generation functionality despite the complexities of advanced processing. The presented design has effectively overcome challenges related to precise alignment, mode mismatch, and mechanical stress during fiber coupling. This robust integration framework is not limited to single-photon sources, finding applications in other fields. These include quantum key distribution, quantum metrology, and photon-based simulations, necessitating precise fiber alignment. Furthermore, it applies to lab-on-fiber sensing [212, 213], highly sensitive refractive index and temperature measurements [214, 215], and Raman scattering detection [216], all of which require stable operation and precise fiber coupling.

Chapter 5

Micro-transfer printing on SOI, SiN, InP, and metal contacts

5.1 Micro-transfer printing on SOI platform

This section focuses on the design, fabrication, and characterization of a 1D PhCC with InAs/InP QDs, called an InP nanobeam cavity. As the introduction outlines, such structures are of significant interest for their potential applications in integrated photonic circuits and quantum technologies. The initial sections detail the sample design, source (InP nanobeams) and target structure (SOI chip with Si WGs and outcouplers). Subsequently, the micro-transfer printing process is presented, ensuring relatively high yield, determinism, and precision, enabling seamless integration of III-V materials with silicon photonics.

The section further explores the experimental characterization of the fabricated devices, conducted at both room and cryogenic temperatures. These studies demonstrate light coupling from the nanobeam cavity to the SOI chip and the external outcoupler, validating the design and fabrication process. Additionally, the ability to tune the QD transition to the cavity by adjusting the structure's temperature is presented. Finally, the last section discusses the optical properties of the cavity, highlighting the Purcell enhancement achieved for QD transitions.

5.1.1 Sample fabrication

Chip design

The nanobeams were designed to have 1 µm width and 15 µm length. The periodically etched holes along the nanobeam form a 1D PhCC. The exemplary structure is shown in Fig. 5.1. A series of 1D PhCC has been fabricated with the period varied from 300 nm to 380 nm in a step of 10 nm, and the gap ranged from 800 nm to 900 nm in a step of 20 nm. The radius was set to either 80 nm or 100 nm. The mask designs (generated by a python script file using the Python gdspy library) assumed that the circles' radius would increase by 12.5 nm during fabrication (over-etch of the mask during InP dry etching, measurements performed in Chapt. 5.4). The mask design is visible in Fig. 5.2. Initially, the mask design included resist tethers - a grey

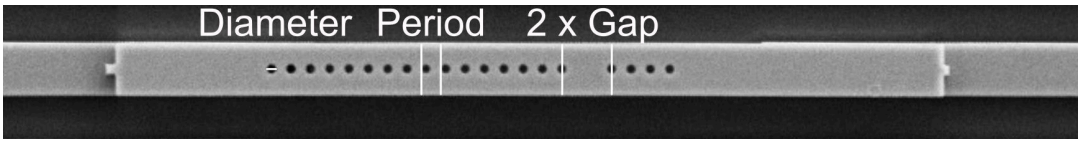

FIGURE 5.1: SEM of one of the fabricated nanobeams with highlighted varied design parameters: hole diameter, cavity gap, and period.

layer above the white layer in the mask structure - to support the membranization and transfer of a whole 50x50 μm^2 coupon. However, during the fabrication process, it was discovered that small InP tethers close to the nanobeam geometry were sufficient to ensure stability and precise pick-up and placement. This rendered the additional resist tether layer unnecessary, simplifying the fabrication steps without compromising any parameter.

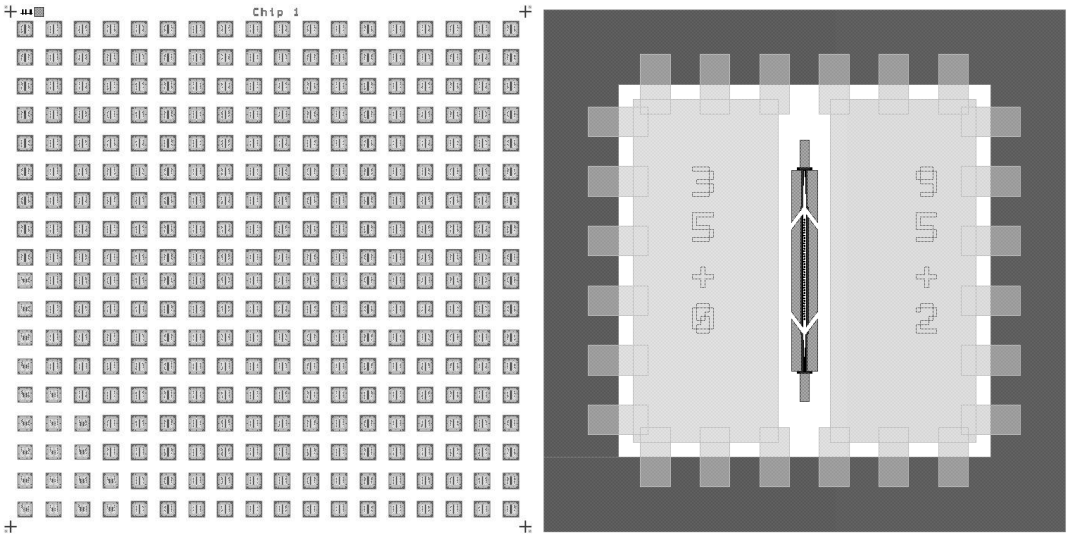

(a) Area of 18x18 unique waveguide patterns with varing parameters.

(b) Detailed mask design for an individual InP nanobeam device.

FIGURE 5.2: Large (a) and detailed (b) view of mask design. The elements in (b) are described in Fig. 5.3.

Source substrate

Similarly to the previous chips, fabrication of the source (structure and substrate) started by deposition of 500 nm of the InP buffer layer on the InP wafer by MOVPE. Then, the sacrificial layer of 100 nm InGaAs was deposited, followed by 125 nm of the InP top layer and 0.93 monolayer of InAs to form QDs in the Stranski-Krastanov growth mode. Subsequently, the QDs were annealed ($485^{\circ}C$) and covered by 125 nm of the InP cap layer. Afterwards, the 1000 nm of SiO_2 was deposited by PECVD and 120 nm of Al by the e-beam evaporator. This wafer was bonded with the Si wafer using adhesion bonding with BCB. The adhesion promoter was spun on the Si and InP wafer for 60 s at 2000 rpm and baked for 1 minute at $160^{\circ}C$ on a hotplate. Si

was coated with BCB at a spincoater for 60 s at 2000 rpm and baked for 10 minutes at 90°C to evaporate the solvent from BCB. The wafers were bonded at 250°C and 6 atmospheres of pressure at the wafer bonder. Residual BCB was later ashed with plasma asher with CF_4 plasma. InP substrate was removed in an HCl bath for about 70 minutes, and the InGaAs sacrificial layer with H_2SO_4 and H_2O_2. A hard mask for e-beam lithography was deposited using PECVD with a deposition of 95 nm of SiN (checked with ellipsometry).

The wafer was coated with 180 nm CSAR resist and exposed using an e-beam with two doses (low - for large parts of patterns not requiring precision, and high - for parts necessitating high resolution). Later, the chip was developed and inspected using optical microscopy. The transfer of the pattern from CSAR to InP was done using two steps; firstly, the pattern was transferred to the SiN hard mask in ICP dry etch (120 s, etch rate - 55$\frac{nm}{min}$) and secondly, InP was etched in HBr chemistry at 180°C. (140 s, etch rate 140 $-$ $\frac{nm}{min}$). After the etching, the chip requires immediate submersion in DI since HBr residues continue to etch InP in the atmosphere. At this step, 2D imaging and localization of the QDs could be performed on the sample if required. After the dry etching, the sample was ready for membranization. The buffered hydrofluoric acid batch was used where the chip was submerged for 180 s. Subsequently, it was rinsed in DI and dried with nitrogen gas, and the chip was optically inspected. The SEM of the fabricated structure before the membranization is visible in Fig. 5.3. The large outer opening in InP was defined using a high current in the e-beam lithography step and letters and the area close to a nanobeam with the low current to achieve high precision. The four tethers holding the nanobeam during the membranization are also visible. Numbers on the left and right describe the parameters of the 1D PhCC, its width, period, cavity tape, and inside the gap.

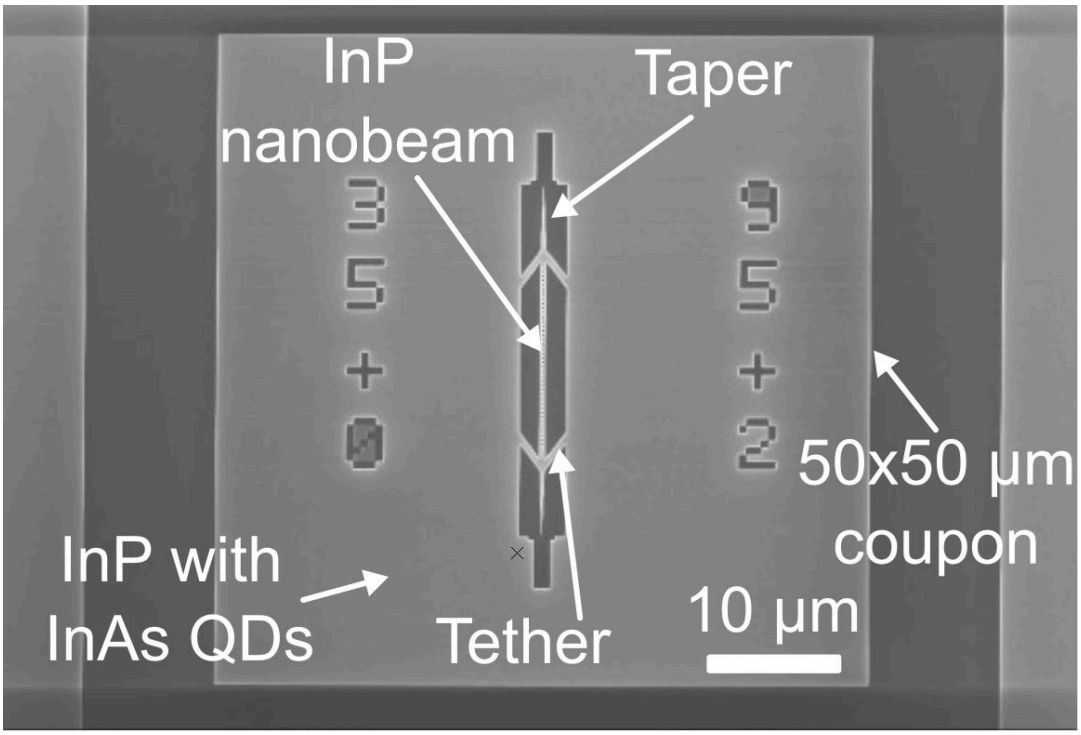

FIGURE 5.3: SEM image of an InP nanobeam with integrated InAs QDs in 1D PhCC. The nanobeam features tapered ends for increased coupling, and it is supported by tethers for stability during the membranization. The structure is positioned within a 50×50 μm coupon.

Target substrate

The target substrate was an SOI chip (220 nm of Si, 2 µm of BOX) with 500 nm wide waveguides and outcouplers visible in Fig. 5.4. The chip was coated with diluted (divinylsiloxane) BCB in a ratio of 1:5, and the chip was baked for 10 minutes at 160°C. To achieve a nanometer-range thickness of the BCB layer, it was spun at 5000 rpm for 60 s and baked for 10 minutes at 90°C. This process of spin coating BCB increases surface flatness and thus increases the van der Waals forces holding the InP nanobeam to the chip. Compared to the source substrate discussed in the previous chapters, there is no Al mirror on the target substrate.

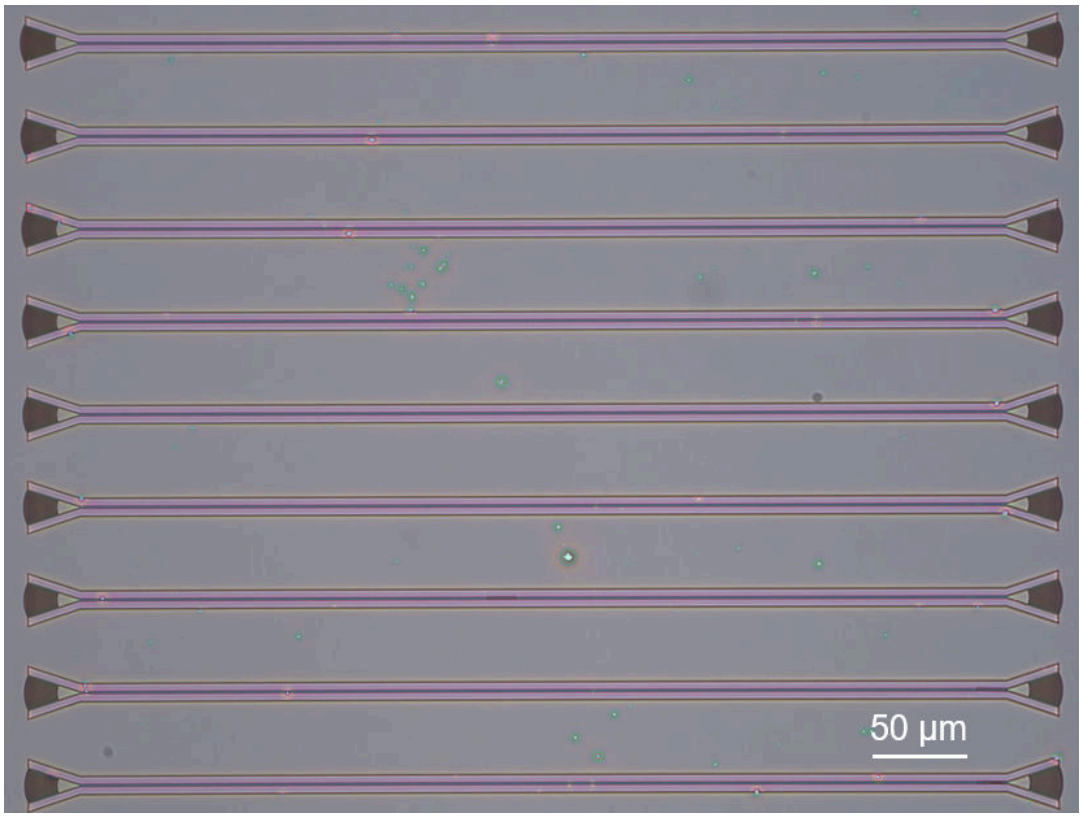

FIGURE 5.4: Optical microscope image of SOI chip with Si waveguides and outcouplers, before transfer of the InP nanobeams.

Micro-transfer printing

The chip was bonded to a 6-inch wafer using a crystalbonder for micro-transfer printing. For transfer, a 50x50 μm^2 stamp was used and the transfer parameters were: pick acceleration - 0.7 $\frac{\mu m}{s^2}$, pre-pick duration - 4s, overdrive distance in the range of $150 - 170$ μm, overdrive speed - 30 $\frac{\mu m}{s}$. The precision of the transfer was checked with an optical microscope. One of the nanobeams transferred to a device is presented in Fig. 5.5, where the 500 nm-wide Si waveguide is visible on which a 1 µm-wide InP nanobeam containing InAs QDs and 1D PhCC is placed. The transfer yield was near unity. For that discussed chip, 23 out of 24 nanobeams (1 failed to pick up a nanobeam) were successfully printed with micro-transfer.

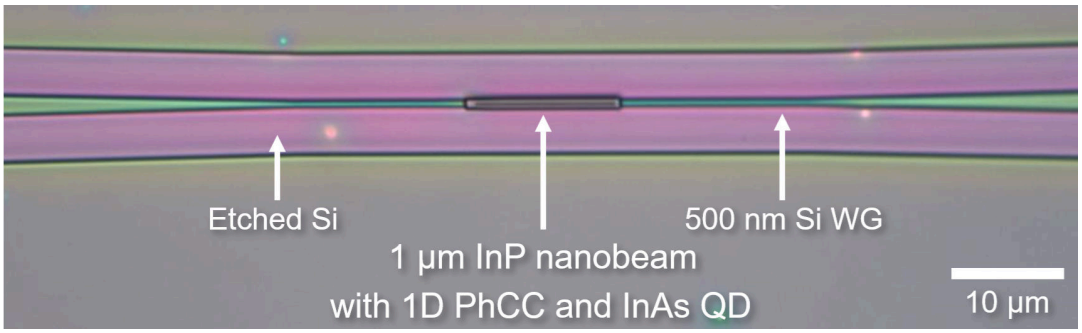

FIGURE 5.5: Microscope image of the InP nanobeam with InAs QD integrated with SOI using µTP.

After the transfer, the BCB was cured with a 40-minute mild bake on a hotplate set to 110°C. The short time and relatively low temperature were set to avoid movement of the micro-transferred structures. Longer times and higher temperatures may result in better adhesion due to the phase transition of BCB to the glass state, as seen in the diagram on the right.

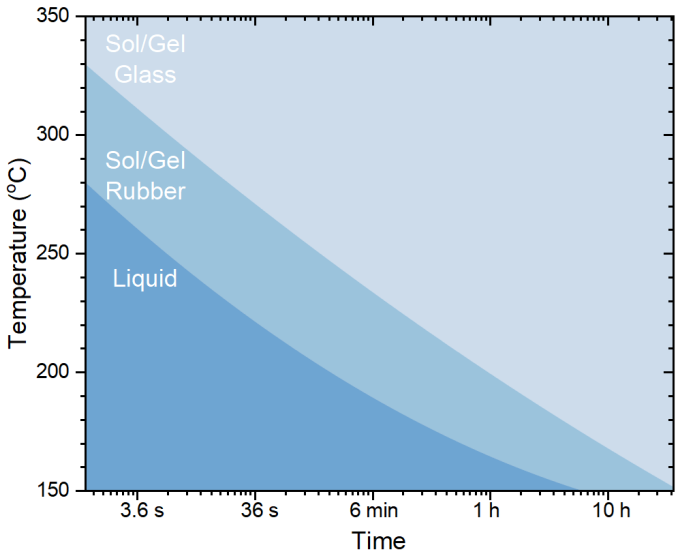

FIGURE 5.6: Phase diagram for DVS-bis-BCB after [217].

5.1.2 Optical spectroscopy

5.1.2.1 Room temperature microphotoluminescence

Firstly, for the optical characterization of one of the source structure shown in Fig. 5.2 was performed at room temperature with the microphotoluminescence experiment. The laser spot was focused at the center of the nanobeam, and the signal was resolved on a monochromator with an InGaAs camera detector. The exemplary emission spectrum of one of the structures excited with hundreds of µeV is shown in Fig. 5.7. Wide emission from the QDs ensemble can be identified, spanning the range of 1400 nm to 1600 nm. The cavity mode is clearly visible. A fit with the Gaussian function to the cavity mode yields an FWHM of 2.4 nm and a central wavelength of 1566.6 nm. Therefore, the Q factor for this cavity is established to 653 at room temperature.

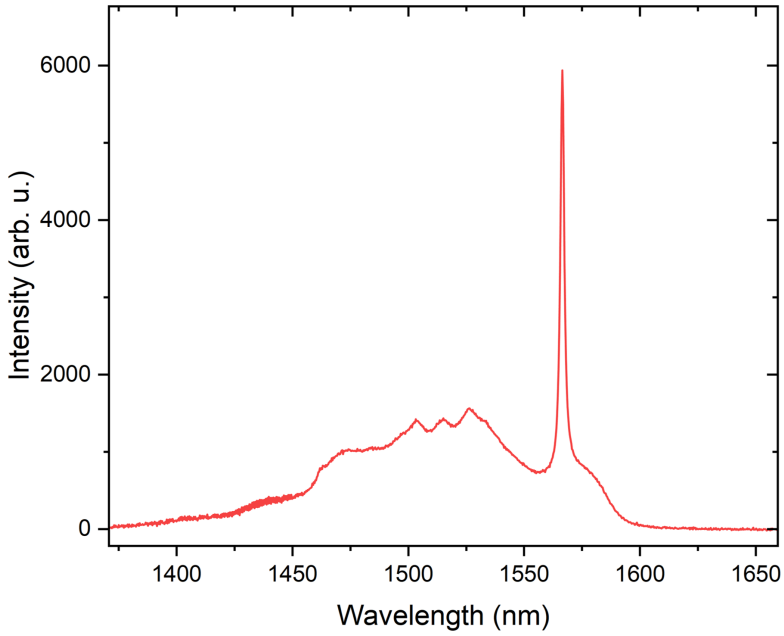

FIGURE 5.7: Room temperature emission spectrum of an InP-based nanobeam PhCC device with InAs QDs. A prominent peak around 1550 nm comes from a well-confined photonic mode of the cavity.

Similar studies, as described above, have been conducted on many nanbeam cavities considering the period- and gap-parameter space. The results of the µPL experiment are visualized in Fig. 5.8. It is shown that by varying the gap and period of the structure, the central wavelength can be precisely linearly tuned across tens of nanometers. The tuning coefficients are 1.93 ± 0.40 nm shift of the central wavelength per nm change of the period, and 1.01 ± 0.12 nm shift of the central wavelength per nm change of the gap. The region between 1563 nm and 1566 nm is highlighted by drawing two horizontal lines because there is an expected blueshift of a cavity mode of around 13-16 nm when cooling the sample down from 300 K to 5 K. The change in the refractive index of materials drives the blueshift. Including this shift ensures that cavities characterized at room temperature operating around 1565 nm would have a mode at 1550 nm at 5 K; including this shift is also important when designing a cavity for a preselected QD with a known wavelength of the most intense transition.

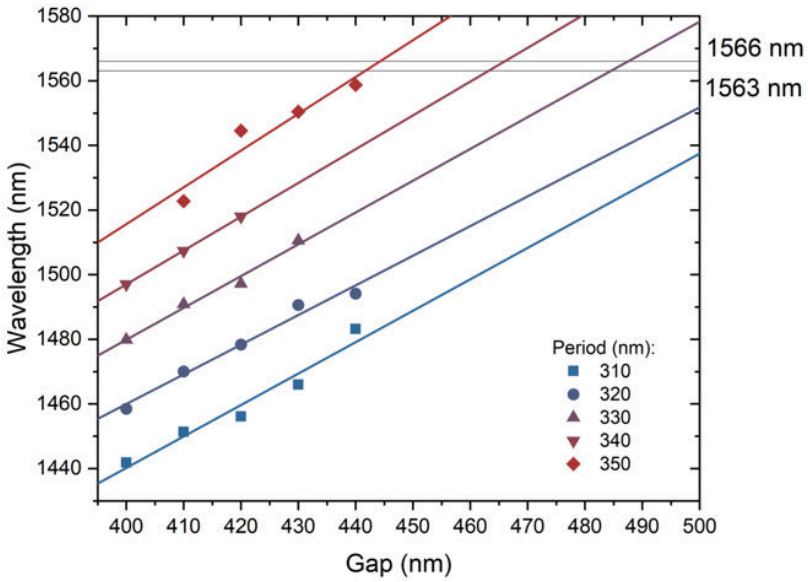

FIGURE 5.8: Experimental data of mode wavelength plot versus cavity gap for photonic structures grouped by different periodicity with color (ranging from 310 nm to 350 nm), showing the dependence of resonant wavelength on gap size for each period. This analysis aids in the design of photonic structures for precise cavity mode wavelength control.

Figure 5.5 presents the InP nanobeam transferred to the center of a structure. This part of the Si waveguide has width 500 nm. This configuration requires separation of the excitation and detection paths because of the long distance (250 µm) from a center (InP nanobeam) to an outcoupler. For the experiments with one microscope objective, the InP nanobeam was transferred to a close vicinity of the outcoupler to excite it with a laser at a nanobeam spot and collect the emission from the outcoupler.

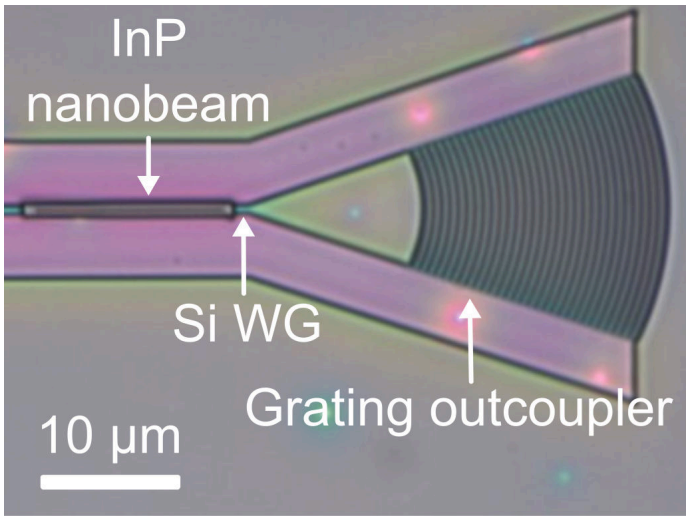

FIGURE 5.9: InP nanobeam placed near the outcoupler for a simultaneous excitation and detection through the same microscope objective.

5.1.2.2 2D Imaging

For the next experiment, the detection path of the experimental setup was guided into the imaging part of the setup on the 2D InGaAs camera detector. The structure with three transferred nanobeams near the outcouplers is visible on the left in

Fig. 5.10. The structure was illuminated with white light and the signal was collected using a 10x microscope objective. On the right in Fig. 5.10 the entire visible area was uniformly illuminated in the wide-field setup arrangement with a 660 nm laser. The collected signal was filtered on the detection path with a 1500 nm long-pass filter and a 1550 $\pm$ 25 nm bandpass filter. This allowed for filtering out the laser light, InP and wetting layer emission, and part of the QD ensemble emission. The collected image by the 2D InGaAs camera detector after background subtraction is presented on the right in Fig. 5.10. With this intensity scale, the black regions correspond to the QD ensemble emission from the whole InP nanobeam, including the cavity mode, so the emission must be filtered out from the image to recognize outcoupled light. Notably, the signal from the outcoupler is visible for these three outcouplers where the nanobeam is placed near the outcoupler, which is a clear confirmation of the light transfer from the InP nanobeam by the Si waveguide to the outcoupling system for free space propagation.

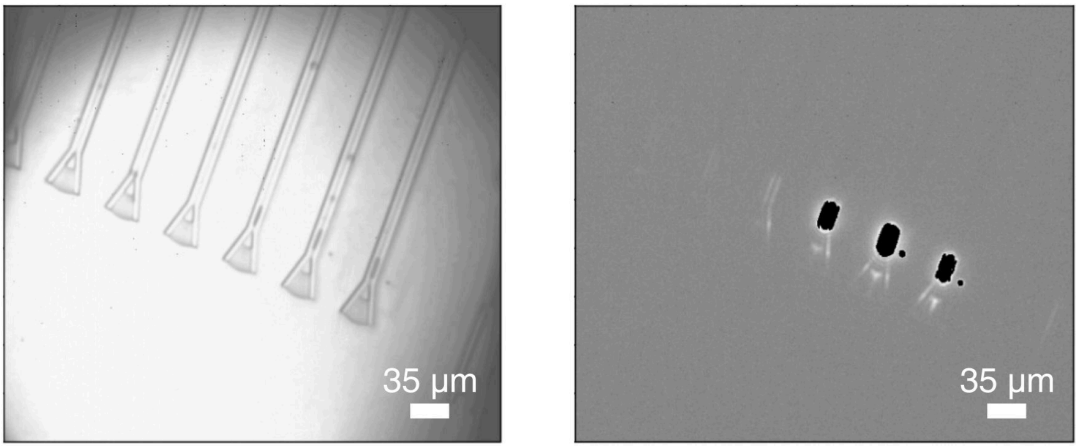

FIGURE 5.10: On the left is the structure view under white light illumination and 10x objective and on the right is the wide-field illumination with a 660 nm laser and detection also on the 2D InGaAs camera.

Additionally, using relatively low laser power (tens of µW), an optical bandpass filter of 1550 $\pm$ 15 nm, and a 50x magnification objective for 2D imaging, one can confirm the optical field distribution confined to the optical cavity (visible in the middle of the InP nanobeam).

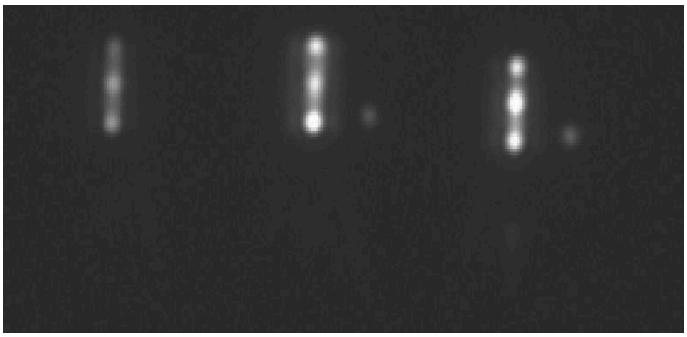

FIGURE 5.11: Three InP nanobeams with visible cavity mode emission in the middle.

In case of the InP nanobeam demonstrated on the far right in Fig. 5.9, a more detailed investigation was performed. To observe this emission transferred to Si and outcoupled towards the microscope objective, we used the 50x magnification microscope objective and additional spatial filtering in the confocal configuration with the mechanical aperture. The integration time was increased to 10 s, and the 1550 $\pm$ 25 nm bandpass filter was exchanged for the 1550 $\pm$ 15 nm one. The collected signal is visible in Fig. 5.12 (a); the fine pattern of electromagnetic interferences and scattering on the outcoupler leading to vertical outcoupling of the signal can be seen. This experimental result was imposed on the view of the structure from the microscope image and presented in Fig. 5.12 (b). This emission pattern matches the expected behaviour of such gratings (FDTD simulation of a grating is shown in Fig. 1.7), pointing to the maximum intensity in which the core of the single mode fibre could be applied for maximum coupling.

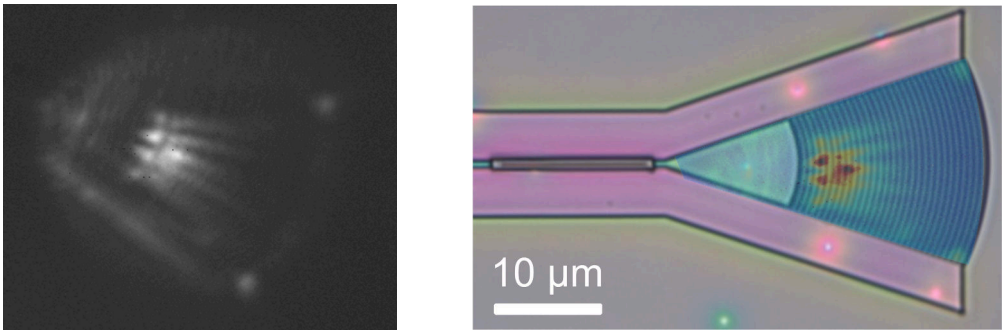

(a) Spatial distribution of the infrared light field from an outcoupler.

(b) Image (a) imposed on microscope image of a device.

FIGURE 5.12: Highly-magnified optical microscope images of the outcoupler under the contionus-wave excitation of an InP nanobeam operated at room temperature.

5.1.2.3 Microphotoluminescence experiment at cryogenic temperatures

This section presents the experimental results of the µPL measurements performed at cryogenic temperature (5 K). The examined structure corresponds to the one transferred to the SOI chip. The µPL spectrum is displayed in Fig. 5.13 (a). PL emission was collected with a 20x magnification microscope objective. The laser spot was focused at the center of the cavity. It resulted in observing multiple sharp transition lines originating from the excitonic recombination in multiple QDs. In addition, a pronounced cavity mode is visible at ~1557 nm . Regarding the emission lines on top of the cavity mode, their higher intensity is likely due to Purcell enhancement (see Sec. 1.5.6.1). To measure the lifetime of these transitions, the pulsed excitation was used with the 80 MHz repetition rate at the pulse central wavelength of 805 nm, and the collected photons were guided to the SNSPD. The photoluminescence decay traces are displayed in Fig. 5.13 (b). The decay curves were fitted with a parametrized exponential function $y(\tau) = y_0 + Ae^{-\frac{\tau}{\tau_1}}$. In this view, we can compare

the lifetimes of the emission lines out of the cavity mode, having τ in the range of 1.0 ns - 1.5 ns, and for the cavity-coupled emission, which is ~0.51 ns (at 5 K, line on the cavity). The result clearly indicates Purcell enhancement with a Purcell factor of about 2.5.

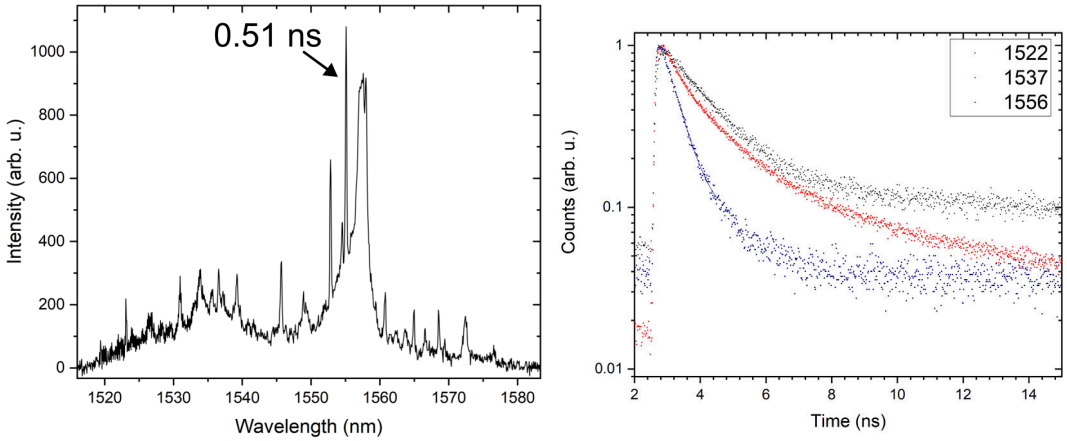

(a) µPL spectrum at 5 K.

(b) Time-resolved µPL traces measured for the emission lines with indicated emission wavelength.

FIGURE 5.13: Low-temperature emission properties for the similar structure as presented in Fig. 5.9. (a) The µPL spectrum after excitation and detection at the center of an InP cavity. Sharp emission lines are superimposed with a relatively broad cavity mode. (b) Time-resolved µPL. The decay traces are measured for emission lines presented in (a). The emission wavelength indicates selected emission lines.

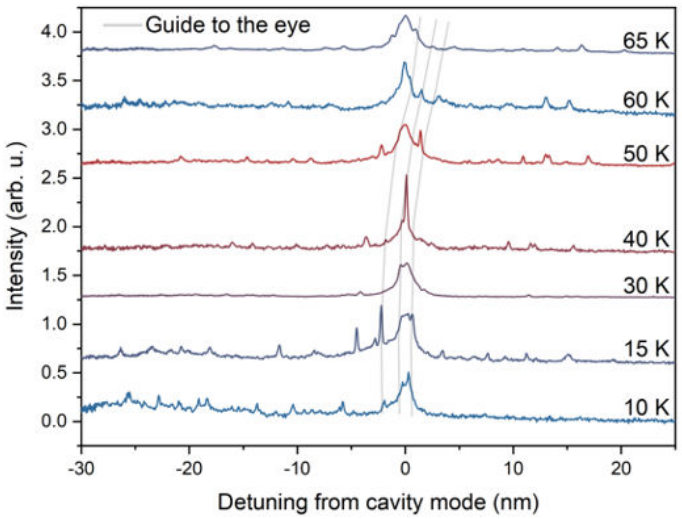

FIGURE 5.14: Temperature-driven tuning of the QD emission lines and the cavity mode. The cavity mode was fixed at the "zero" position, while some QD transitions shift over the cavity mode with temperature, showing an increase in the line intensity when hitting the cavity resonance. The structure was excited non-resonantly by a continuous-wave laser at 787 nm. The grey lines are a guide to the eye, indicating the path of emission lines are following.

The spectral QD-cavity coupling can be tuned by driving temperature of the chip. Figure 5.14 presents recorded µPL spectra at the chip temperature ranging from 10 K to 65 K. For clarity, the cavity mode was shifted to a "zero" position, a reference for QD spectral shift. Grey lines were added to guide the eye in tracking individual transition peaks. As seen, for the temperature of 40 K, the QD line matches its energy with a cavity mode, indicated by its intensity enhancement.

These low-temperature experiments were performed with the excitation and the collection from a center of a PhCC. There was an effort to collect the emission from the outcoupler while exciting an InP nanobeam with a laser while using the same microscope objective - all in cryogenic temperatures in the cryostat. These attempts allowed only observing a cavity mode from an outcoupler with lower intensity (-10 dB). Notably, these experiments at cryogenic temperatures (7 cooling cycles to this chip) did not damage the device. This could happen due to stress induced by different thermal expansion coefficients of the material used.

5.1.3 Conclusions

In this section, the design of a 1D photonic crystal cavity in InP was presented. The fabrication steps and the developed micro-transfer printing procedure allowed the precise transfer of InP nanobeams to the SOI chip with the high yield were described. Characterization of the device at room and cryogenic temperatures allowed to prove light transfer from a nanobeam to the Si chip and the outcoupler. The fundamental cavity mode of the designed 1D PhCCs fit the desired 1550 nm spectral window, and the cavity tuning parameters were determined regarding the gap and period of the cavity structure. The Purcell enhancement of QD emission was achieved at roughly 2.5.

5.2 Micro-transfer printing on SiN waveguides

The SiN platform is an alternative to Si for building a photonic integrated circuit. A general overview of different platforms used for PICs was given in Sect. 1.6.1.1. This chapter describes the heterogeneous integration of InAs/InP quantum dots with SiN waveguides using top- and side-integration approaches.

5.2.1 Sample fabrication and heterogeneous fabrication

Sec. 5.1.1 has already discussed the InP nanobeam fabrication process. Such a nanobeam is now integrated with the SiN platform. The target SiN chip is demonstrated in Fig. 5.15. The chip contains 11 waveguides of 2 µm width and spreads along the entire chip. In the scope of this work, the role of integrated resonators (visible circle-like structures in Fig. 5.15) is omitted, and the focus is put on the waveguides. The SiN waveguides are tapered near the edges and polished from both sides to facilitate efficient edge optical field coupling to the single-mode fibre. In contrast to the SOI chip in Chapt. 5, there was no BCB spin-coated on top, and the InP nanobeams were micro-transferred directly both on top of a SiN waveguide and on its side (see Sec. 5.22). This chip was also used to develop an automatized high-throughput process for the µTP, described in more detail in Sec. 5.5.

FIGURE 5.15: Microscope image of a chip with SiN waveguides spanning through the whole chip width (tapered towards the edges), enabling edge light coupling and detection.

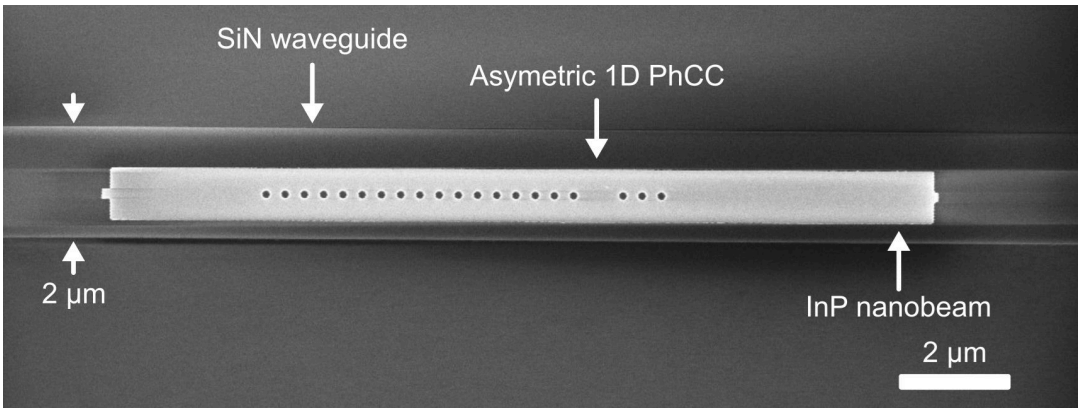

FIGURE 5.16: SEM micrograph of a micro-transfer printed 1 µm-wide InP nanobeam with an InAs/InP QDs. The nanobeam has an etched asymmetrical 1D Photonic crystal cavity to enhance directional coupling into the bottom, 2 µm-wide SiN waveguide.

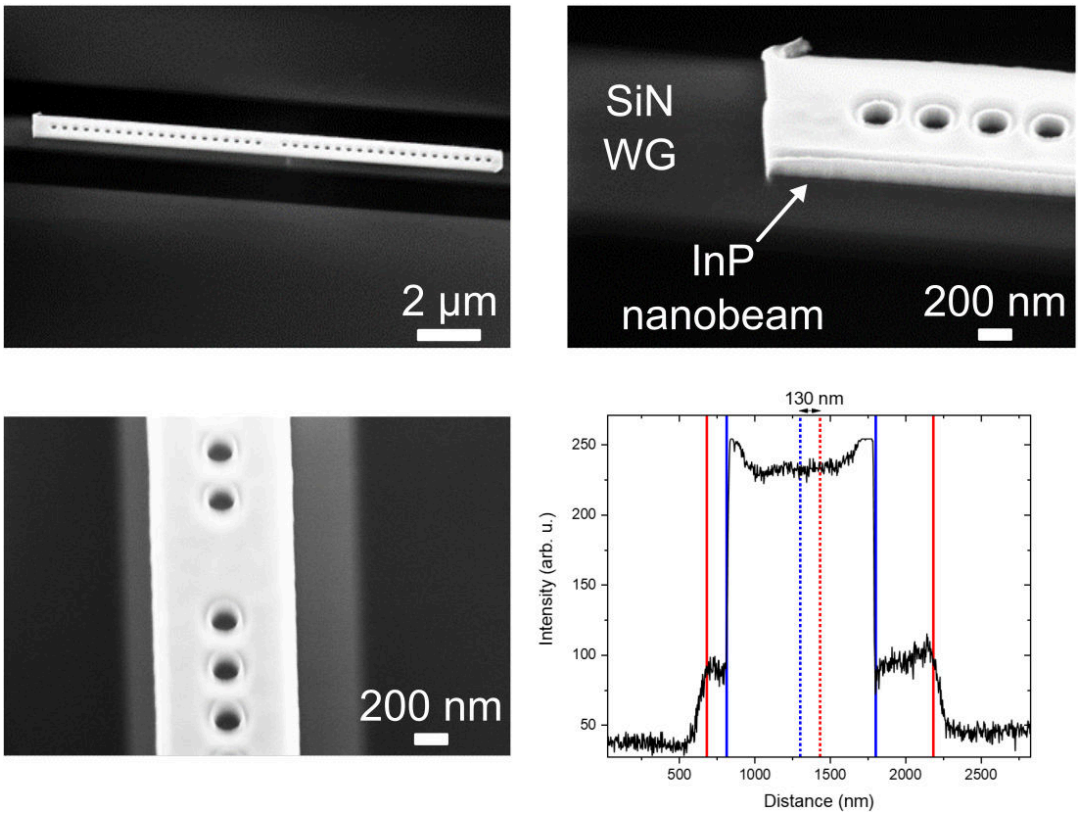

FIGURE 5.17: An exemplary SEM micrograph showing the accuracy of placing the manually transferred InP nanobeam. On the bottom right panel, with red lines, the edges of a SiN waveguide are highlighted, and with blue lines, the edges of the InP nanobeam are underlined. The dashed lines indicate the center position of the InP nanobeam and SiN waveguide. The shift between the central lines is estimated to be 130 nm. For more details on the accuracy of µTP, see Sect. 5.4.

5.2.1.1 Optical characterization

The optical characterization demonstrated in this section was performed with a standard µPL setup at room temperature. Figure 5.18 presents a µPL spectrum from an InP nanobeam printed on top of a SiN waveguide. The optical response is dominated by ensemble emission of InAs/InP QDs. In addition, a high-intensity spectral one is observed at 1567 nm, which is attributed to the cavity mode emission. For this cavity, the quality factor was estimated to 532.

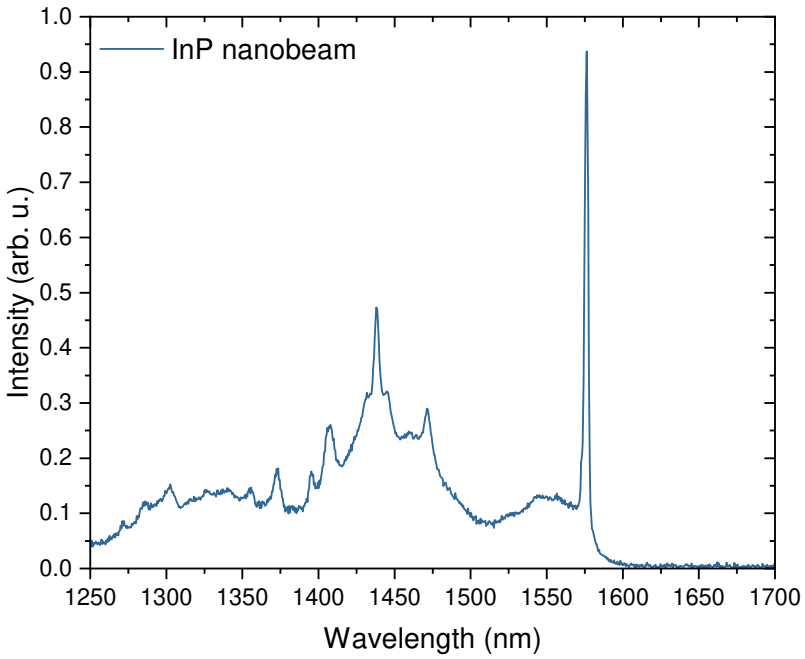

FIGURE 5.18: Room-temperature µPL spectrum measured at the center of the InP nanobeam cavity with visible broadband QDs emission and a cavity mode at 1575 nm.

One of the objectives of this thesis was to determine the shift of the fundamental cavity mode if the InP nanobeam were placed on top of the SiN WG compared to the cavity mode in membranized structure (suspended in air). In Fig. 5.19, a stack of µPL spectra for various nanobeam cavities is presented, varying the etched hole radius (80, 95, 100 nm), the gap size (from 390 to 450 nm), and the grating period (from 320 to 350 nm).

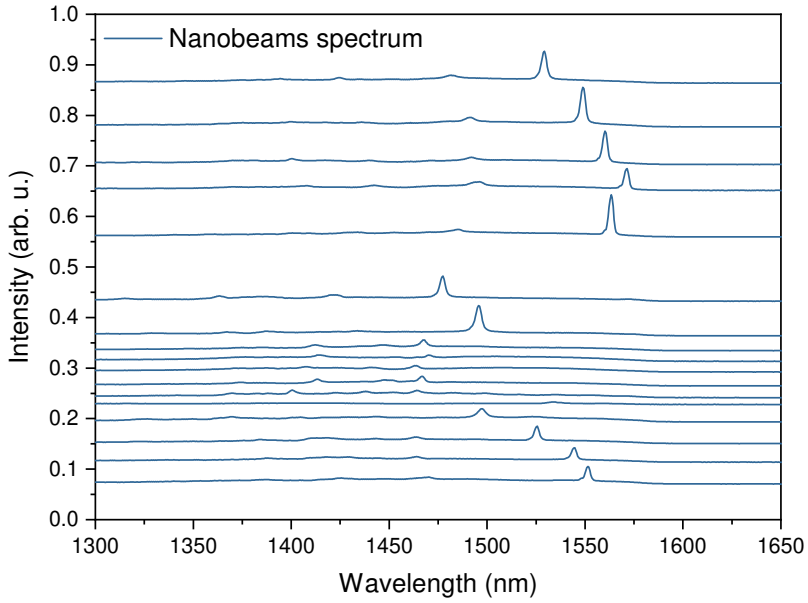

FIGURE 5.19: Spectra obtained from various InP cavities, showcasing distinct cavity mode positions.

Similarly as in Fig. 5.8 in Fig. 5.20 it can be seen that by varying the gap, radius, and period of the structure, the central wavelength can be precisely tuned across tens of nanometers.

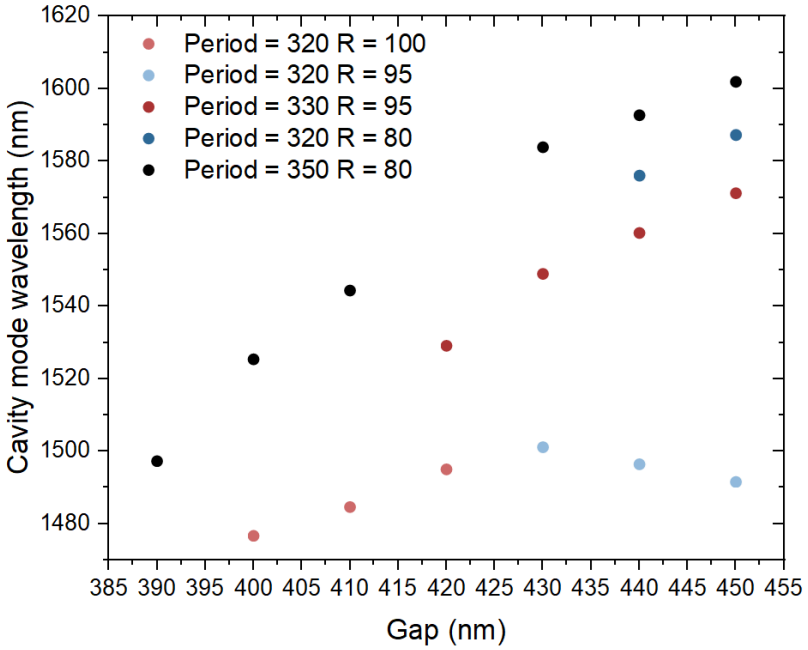

FIGURE 5.20: Measured fundamental cavity mode spectral position as a function of the gap size of the cavity, for different PhC periods and hole radius.

Refractive index of the medium surrounding the cavity has a significant impact on the cavity mode. Air typically has a refractive index of around 1, while SiN has a higher refractive index (typically around 2). When the cavity is transferred to

SiN, the local refractive index around the cavity changes, which alters the resonance condition for the cavity modes. Figure 5.21 presents an evolution of the fundamental cavity modes' wavelength for InP nanobeams with indicated grating parameters after transferring the nanobeam to the SiN WG. A nearly 23 nm redshift of a cavity mode for the heterogeneously integrated system with SiN and a redshift of the cavity mode with an increasing gap value for almost all parameter values can be observed. This parameters of this shift are important for preliminary characterization of the devices in InP membranes which could be deterministically transferred to the SiN.

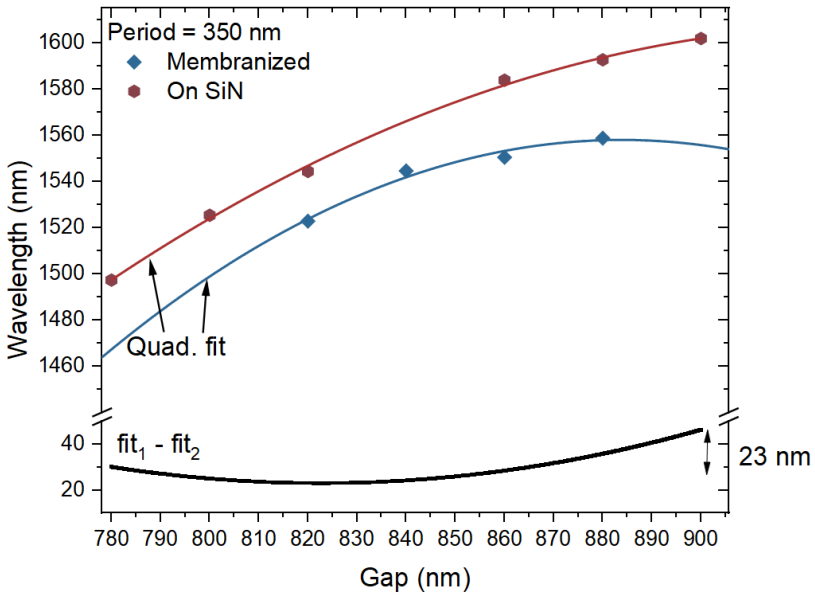

FIGURE 5.21: Compared the measured cavity mode spectral position for an InP nanobeam placed on top of a SiN waveguide and membranized (suspended in air) InP nanobeam. The trends were fit with a quadratic formula, and the black line shows the fit difference between both tested systems.

5.2.1.2 Docking of a nanobeam to SiN waveguide by µTP

Despite achieving a high µTP integration accuracy of an InP nanobeam with the SiN waveguide demonstrated through statistical analysis in Sec. 5.4, the coupling efficiency between the nanobeam and the waveguide can still be affected by slight misalignment. The aforementioned positioning with printing on top of the waveguide depends on visual inspection by an operator, and the optical microscope diffraction limit ultimately constrains further advancements in transfer printing precision. In this section, an integration method of precise in-plane docking of an InP nanobeam directly to the SiN waveguide by µTP is demonstrated, which overcomes the limitations of visual alignment and, as presented in the literature, provides a precise and reliable approach for integrating waveguide-based light sources into PICs, ensuring exceptional parameters in micro-transfer printing [218].

In this context, the micro-transfer printing process involves rough alignment of the InP nanobeam in close proximity to a SiN waveguide sitting on the sample's

plane, and moving it carefully to a desired position sticking to the side of a 50x50 μm^2 stamp. During this process, the nanobeam was moved around 30 µm through the chip. To avoid undesired accumulation of particles at the InP/SiN interface, the soft structure of PDMS, which prevents damage, is typically used. When the InP nanobeam sticks to the SiN waveguide and the process is over, the stamp is removed carefully. The coupled WG system is demonstrated in Fig. 5.22 (c).

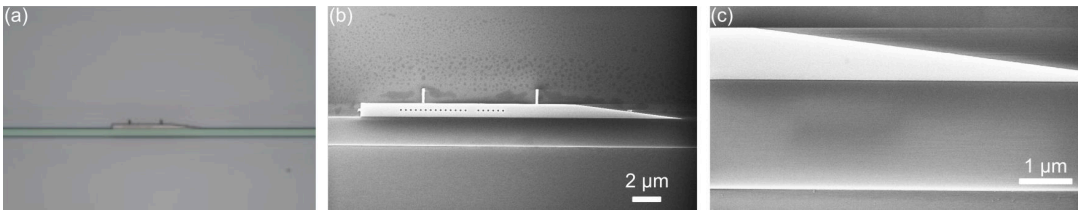

FIGURE 5.22: Top images of an InP nanobeam with InAs/InP QDs and asymmetric PhCC docked to SiN waveguide with µTP. (a) Optical microscope image. (b) SEM image. (c) Close-up on a SiN/InP interface.

Notably, the side-docking technique allows for a high-quality interface between the InP and SiN WGs. It thus suggests maximizing the coupling efficiency since, as seen in Fig. 5.22 c), the gap is not clearly visible under the SEM microscope (in a similar approach, the unidirectional coupling can reach 64% coupling efficiency [218]). Comparing this method to standard micro-transfer printing and placing the nanobeam on top of the SiN waveguide, the side-docking approach has the advantage of high placement precision. In the standard approach, the nanobeam is typically off-axis of the substrate waveguide.

5.2.2 Conclusions and outlook

This section presents the heterogeneous integration of InP nanobeam with InAs/InP QDs with a SiN waveguide. This integration was a basis for developing the precise automatized micro-transfer printing process presented in the next section. 5.4. To the author's knowledge, this is the first demonstration of an InP nanobeam with InAs QDs integration with SiN waveguides using micro-transfer printing, both for top and side integration. The accuracy of the integration method was assessed, as well as the role of the substrate in the cavity mode's spectral position. Side docking allowed for the proof-of-principle demonstration of the integration of the mentioned materials, which allowed for more precise and direct contact between source and substrate materials. This method of micro-transfer printing also does not need any alignment marks or ultrafine actuators and high magnification for increased precision. While this transfer-printing misalignment can be consistently minimized to within tens of nanometers, or even nearly eliminated, while maintaining uniformity across each transfer printing process, the prospects for automatized processes are limited as for transfer from the top, as characterized in the next chapter.

5.3 Micro-transfer printing on metal contacts

In all previous experiments, modifications to the QD environment were achieved through laser field power, temperature, and a modified photonic environment, while laser energy detunings for near-resonant or resonant excitations were not explored in this work.

In this section, applying an electric field via metal contacts which offers the advantage of deterministic control over the QD environment is discussed. By using separate contacts for each device, electrical connection allows for multiple individually tuned QDs on chip, where other external perturbations typically do not provide this flexibility. The electric field applied along the growth direction can shift the energy levels of the QD via the quantum confined Stark effect [219–221], allowing control over its optical and electronic properties. This tuning is particularly useful in aligning the QD emission wavelength with a cavity mode or a second emitter (a QD, an atom) to optimize (typically maximize) their interaction and wavefunction overlap. If natural band alignment, doping, and defect levels cause charge accumulation, the contacts can be used for charge state control by preventing or enhancing electron or hole capture rates [103]. If there are multiple QDs in device, it can be used for inter-quantum dot coupling by bending the energy levels [222]. Furthermore, this research is driven by the fact that even for the NV centers, where in principle every emitter has very similar properties, there has to be some tuning of an emitter (e.g. electrical) to achieve high indistinguishability between multiple emitters, which is called remote indistinguishability. Additionally, when the two states of the exciton have the same energy level (degeneracy), the resulting two photons emitted from the biexciton exciton cascade (typically different wavelengths of emission due to biexciton binding energy (see 1.5.4) will have their polarization state perfectly correlated (maximally entangled state). However, this ideal scenario is usually not achieved in QDs due to slight energy differences between these states due to electron-hole exchange interactions (fine structure splitting - FSS) caused by imperfections in the quantum dot's confining potential [223]. In this context, the excitonic FSS can be reduced by applying a forward bias voltage to a Schottky diode [224] enabling the generation of the on-chip entangled photon pairs.

5.3.1 Sample fabrication

5.3.2 Si chip with metal contacts

The fabrication of metal contacts started with the deposition of 500 nm of SiO_2 on a Si wafer to provide an insulating layer. Then, the pattern presented in Fig. 5.23 was exposed via the optical lithography process.

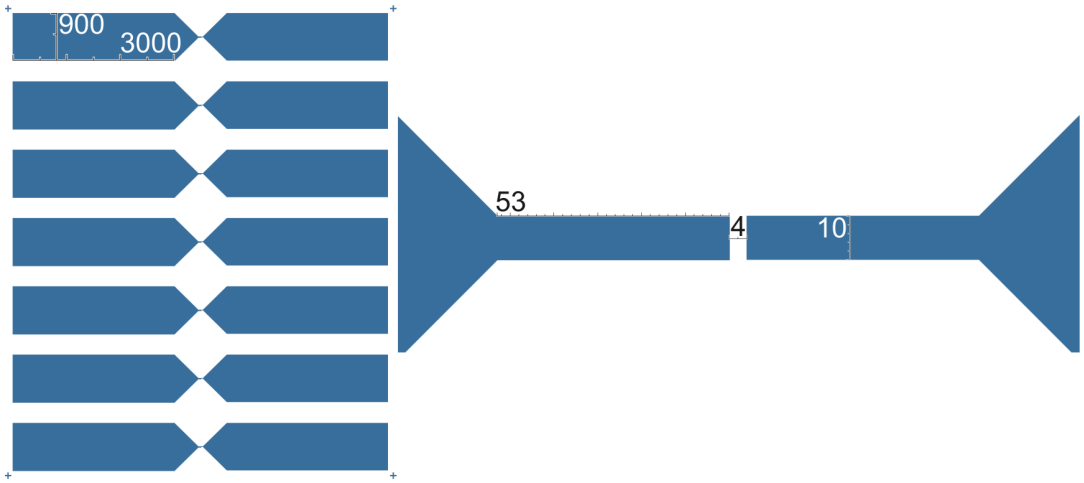

FIGURE 5.23: Mask for a sample with metal contacts, with dimensions in micrometres. The zoomed-in view of the structure's center is shown on the right, highlighting a gap of 4 µm between the two contacts.

After the development, the wafer was covered by 110 nm of Au and 5 nm of Ti using the e-beam evaporator. During the mask development, the contacts with only the Au layer were additionally fabricated but yielded worse results in electrical characterization (none of the characterized devices with only Au layer for contacts showed clear I-V dependence). The wafer was submerged in an acetone bath in the ultrasonic cleaner and left for 20 minutes to perform a lift-off of the resist. After this time, the sample was divided into multiple chips and bonded with a crystal bonder to a 6" wafer. One of the whole chips is presented in Fig. 5.24 a). Some over-stripped fragments are visible on the contacts, resulting from a non-optimized lift-off process.

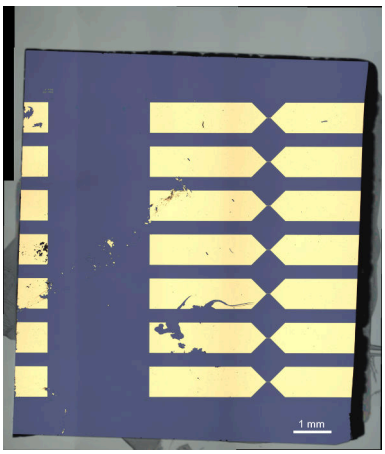

(a) One of the fabricated chips with metal contacts.

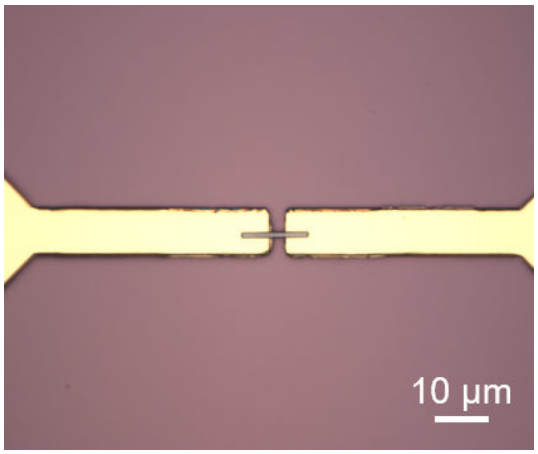

(b) Nanobeam printed on metal contacts

FIGURE 5.24: Optical microscope images of the a) fabricated chip with metal contacts and b) micro-transferred InP nanobeam with InAs/InP contacts.

Semiconductor-metal bonding

Micro-transfer printing was done with the same procedure as in Chapters 5. Transferred InP nanobeams were prepared based on either low-density or high-density QDs. After transfer printing, the chips were loaded into a wafer bonder for 5 minutes at 300 °C and 6 atmospheres of pressure to increase the bonding of InP to Ti. The yield of this procedure was 30%, where 70% of the nanobeams were also bonded but changed position after bonding. Before bonding, the structures were held by weak van der Waals forces. After the bonding, the adhesion was tested mechanically, where their position remained constant during the spin coating of a resist (high centrifugal forces), indicating good adhesion and suitability for potential further processing.

5.3.3 SEM characterization

The contact interface was characterized using SEM. Example images are presented in Fig. 5.25. The edge of the metal layer, where it contacts the semiconductor, appears relatively sharp, with a clear boundary. A well-defined metal-semiconductor interface is critical for minimizing defect states that could trap charge carriers and increase contact resistance. It is also seen that there is a significant surface texture on the metal layer, with a granular appearance. This roughness could impact the contact quality by increasing the surface area, which might affect the electrical characteristics, such as contact resistance or interface quality.

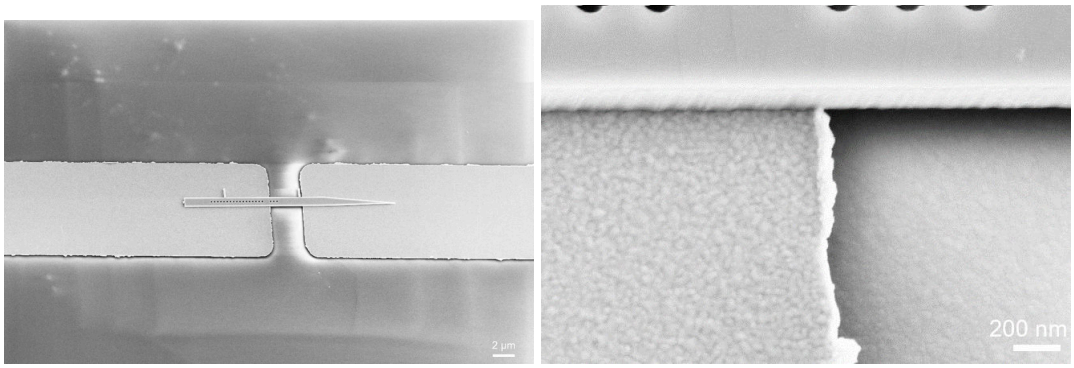

(a) (b)

FIGURE 5.25: SEM images of a metal-semiconductor contact.

5.3.4 Electrical characterization

One of the samples (nanobeam on contacts) was electrically characterized at the DTU cleanroom using a probe station (with the help of dr. K. Połczyńska), where two probes were connected to the chip. The created junction shows Schottky Diode curve characteristics with a threshold voltage of 2 V. Apparent asymmetry of the I-V curve shows rectifying behavior with the positive bias leading to a sharp increase in current compared to the negative bias. Multiple samples fabricated in the same manner showed similar characteristics. There was no current flow during the measurement for the contacts without nanobeam in the middle. The I-V measurement gave information that the metal-semiconductor-metal junction had been formed.

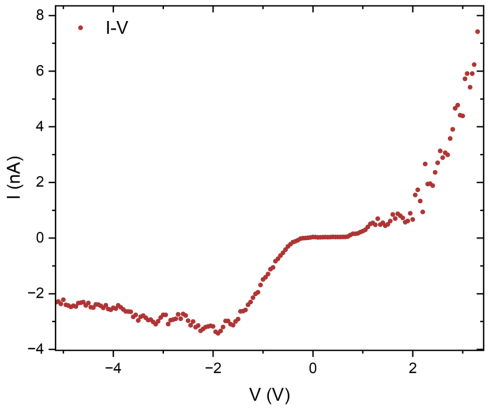

FIGURE 5.26: I-V curve of the fabricated device characterized in the DTU cleanroom.

5.3.5 Optical characterization

In Wroclaw, a custom probe station was built and added to the standard microphotoluminescence setup to allow the study of photoluminescence as a function of the applied voltage to the sample. Figure 5.27 shows the best I-V characteristics with the current flow in the range of µA, much larger than for other samples. This experiment used a precise Keysight (b2901b) measuring unit. The applied voltage was in the range of -6 V to +6 V (no current flow for voltages in the range of -6.0 V to 1.0 V for this sample), and the measured current was in the range from -1 µA to 30 µA.

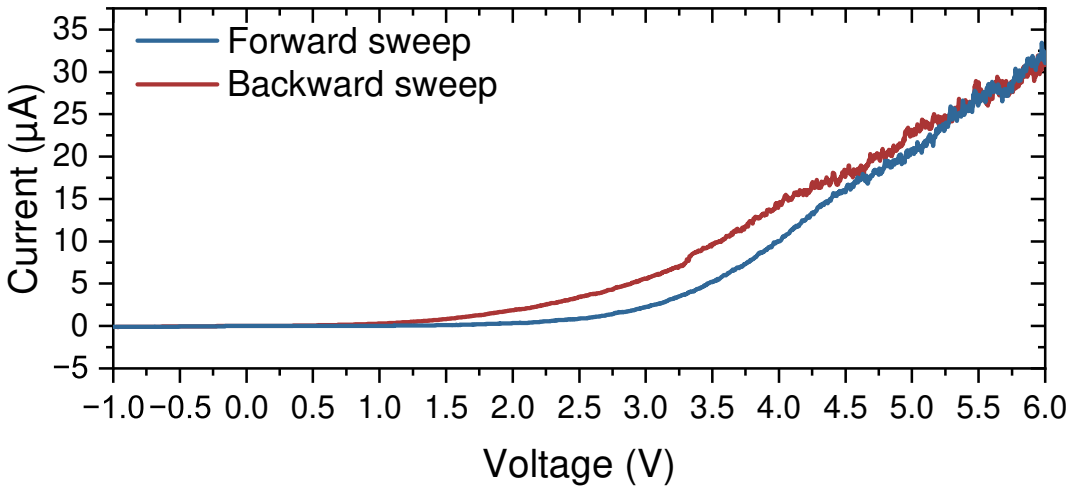

FIGURE 5.27: I-V characteristics of a device with the InP nanobeam on metal contacts, characterized at WUST.

Similarly to samples in previous chapters, these devices were characterized using micro-photoluminescence at room temperature. The result for a sample with a high density of QDs is shown in Fig. 5.28. This optical characterization confirmed that the emission from the QDs was not quenched after processing.

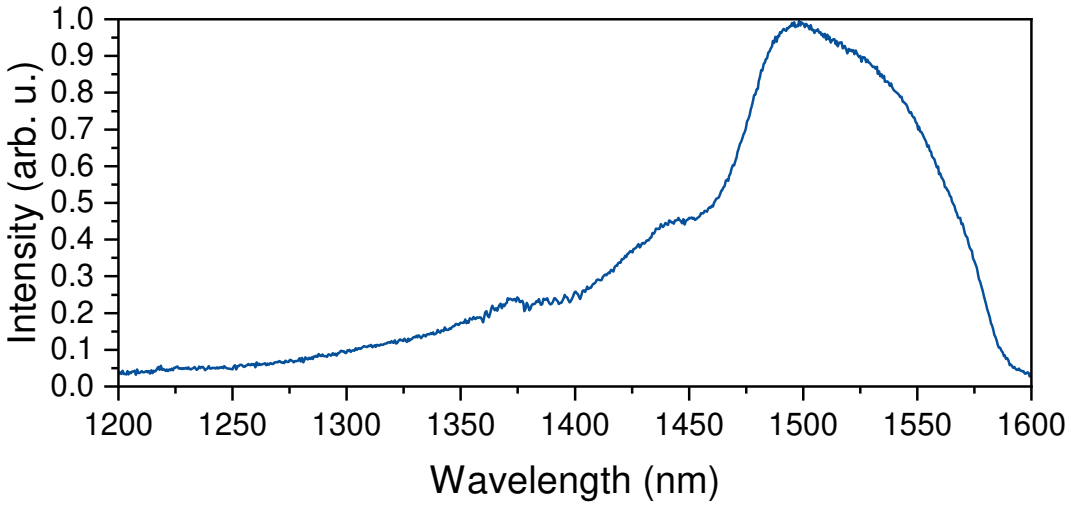

FIGURE 5.28: Microphotoluminescence spectra of high-density InAs/InP QDs on metal contacts without applied voltage to the contacts.

5.3.6 Conclusions and outlook

This chapter presented a fabrication process leading to a device consisting of InP nanobeam with InAs/InP QDs integrated with lateral metal contacts. Importantly, to the author's knowledge, there is no report of micro-transfer printing directly on the metal contact. Usually, the devices are fabricated with top and bottom contacts and then transferred [225, 226]. The latter approach is more mature and limits the density of available components by including macroscopic bonding wires. The approach presented here allows for conducting traces on a wafer, increasing scalability and paving the way for more complex chip architecture fabrication. Current flow of about 30 µA and no degradation to the photoluminescence makes this fabrication workflow an attractive approach for deterministically micro-transferred and electrically contacted devices. Since this approach was proven to be working, the next studies could focus on several aspects:

- Reduction of the device size - the large dimensions of a mask for one device of 7.0x0.9 mm^2 was introduced for easier characterization using a probe station. The size of pads and tapered region can be reduced to about 100x100 μm^2 or smaller footprint, enabling high component density.

- Fabrication of the p-n junction - the source InP wafer was already doped for a n- and p-type conductivity, with and intrinsic region in between (QD layer). Instead of two contacts at the bottom of a nanobeam, two additional fabrication

steps would allow to fabricate one of the contacts on the top of the structure which would allow to create p-n junction and for studies of electroluminescence.

5.4 Accuracy of µTP

In order to determine the accuracy of the µTP, a set of samples was fabricated. Since the estimation of the accuracy of InP nanobeam placement was well below the resolution of the optical microscopy, it imposed the use of SEM for the measurements of the nanobeams' positions. Additionally, to increase the precision of measurement, the InP waveguides were chosen as a platform due to reduced charging in SEM measurements and thus, increased resolution. In Fig. 5.29, there is an exemplary InP nanobeam with an asymmetric cavity transferred on top of the InP waveguide with a designed width of 1.0 µm. The design of this structure follows the approach used to fabricate printed nanolasers on silicon [227], which experimentally achieves high coupling efficiency, but the discussion in this thesis is limited to the accuracy of the µTP.

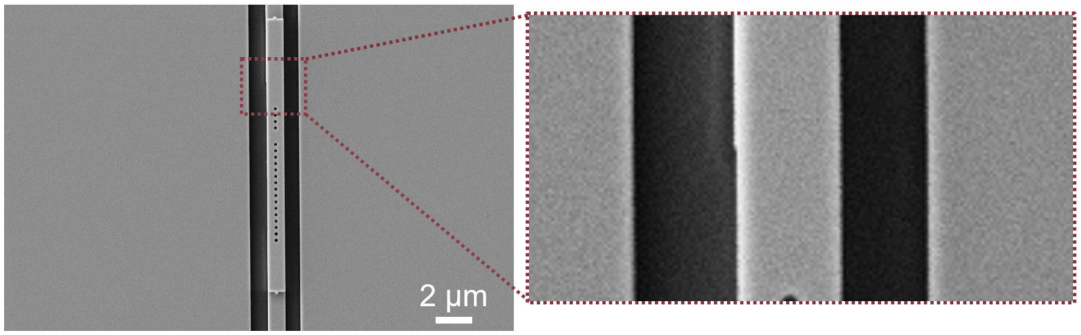

FIGURE 5.29: An exemplary SEM micrograph of 1 µm-wide InP nanobeam micro-transfer printed on top of InP waveguide with high precision. On the right is a closeup of the section where there is visible slight misalignment between these two waveguides.

The side view of one of the structures is presented in Fig. 5.30. It can be clearly seen that the nanobeam is precisely positioned on top of a waveguide gap beneath it.

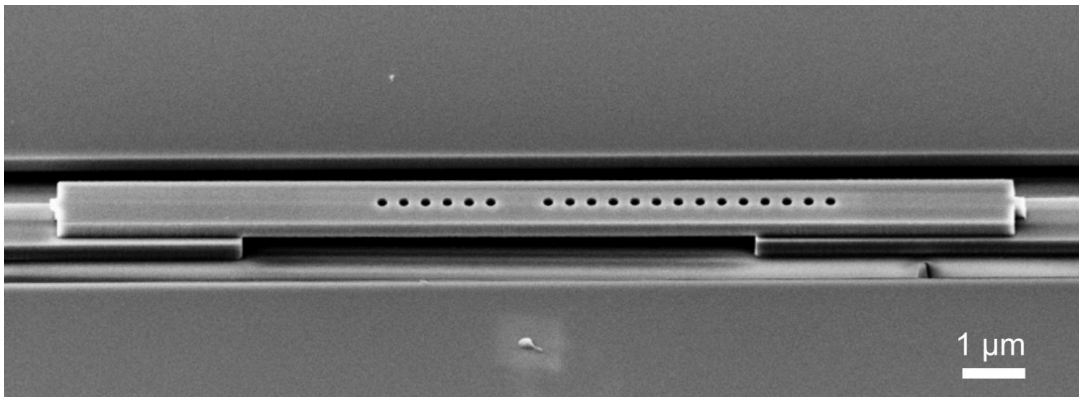

FIGURE 5.30: Side SEM view of the InP nanobeam with InAs/InP QDs transferred to the InP waveguide with a slot gap.

SEM pictures were taken in similar conditions to calculate the accuracy of µTP after transferring 14 InP nanobeams. This matrix of SEM images is shown in Fig. 5.31.

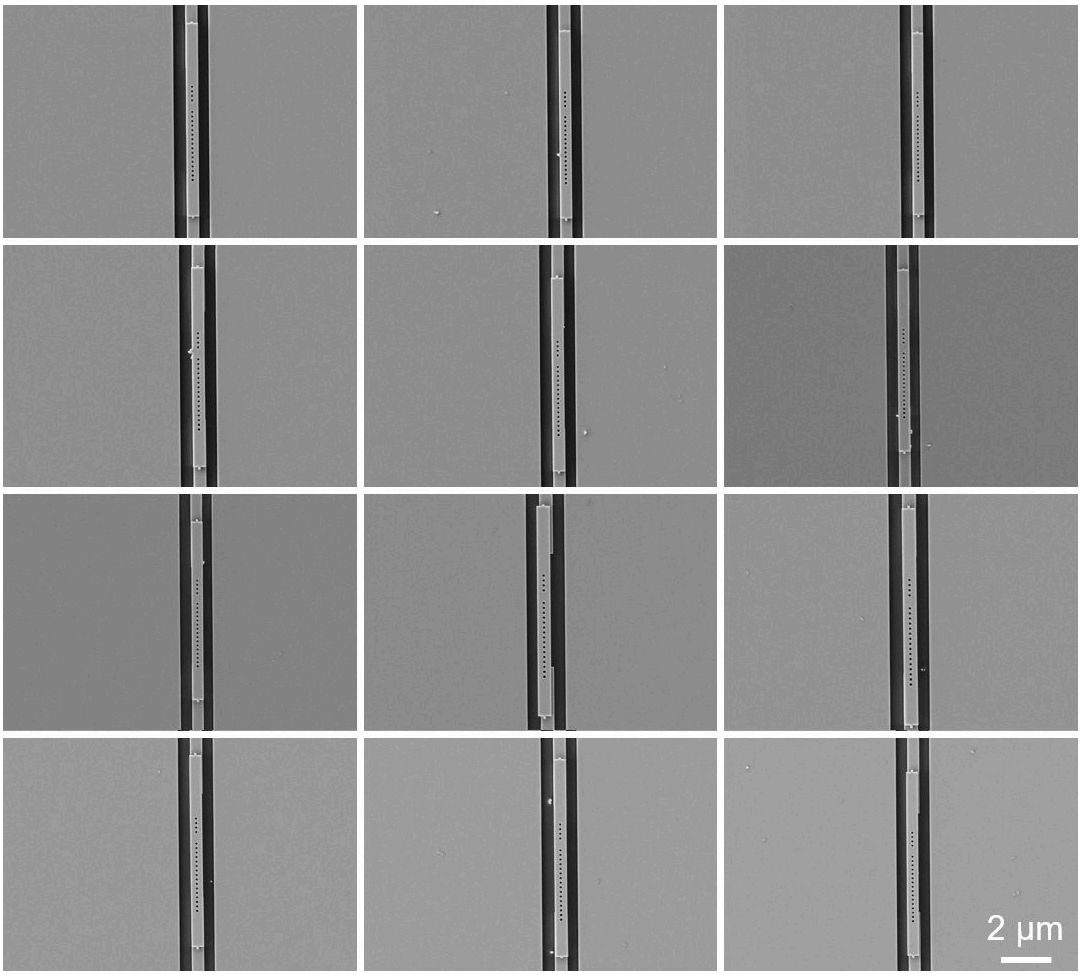

FIGURE 5.31: 12 out of 14 SEMs were used to determine the accuracy of the µTP.

In the ImageJ software, the Sobel edge detector was used to find edges and highlight sharp changes in intensity in the SEMs. The resulting images are shown in 5.32.

FIGURE 5.32: Images from Fig. 5.31 with edges detected using Sobels edge detector.

Next, using the OriginLab software, all the images were centered so that the left and right edges would lie on the same axis. The experimental data points of the edges are visible in Fig 5.33 (red diamonds).

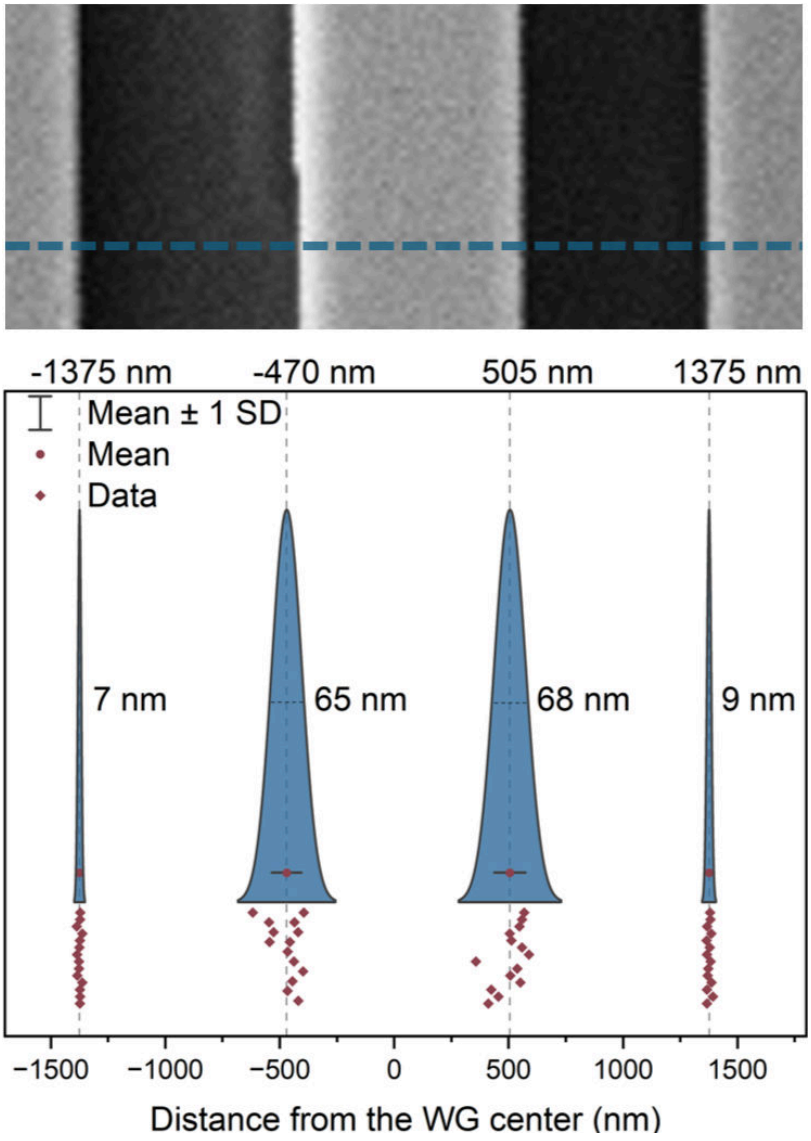

FIGURE 5.33: Distributions of the positions of the elements derived from the SEM image analysis. The micro-transfer printing process does not influence the far-left and far-right distributions and thus value gives the information of this calculation method accuracy. Middle distributions determined by the micro-transfer printing process give information about its precision and accuracy.

These edges' positions were fitted with a Gaussian function, and their 1 standard deviation is put next to the distribution. From this graph, the number of conclusions can be derived:

- Since outer edges positions are defined by mask design and fabrication processes: The left and right edges at -1375 nm and 1375 nm are unaffected by the µTP and rely solely on mask design and fabrication. This approach demonstrates that verifying fabricated structure dimensions (e.g., using SEM for edge detection and centering) achieves an uncertainty (1σ) below 10 nm.
- In the mask distance between these edges was defined as 2700 nm and it is measured to be 2750 nm. It means that over-etch in this process (defined with

a relatively high current in an e-beam) is about 50 nm. This parameter is important for the mask design.

- As seen from the two middle distributions, the uncertainty for the µTP nanobeam placement is below 70 nm (65 nm and 68 nm). Which is comparable to the custom-made µTP setups [228].
- Similarly, as for the edges, the width of nanobeams has changed and the over-etch parameter is 12.5 nm per side (nanobeam width of 1000 nm in design vs measured 975 nm). Decreased over-etch is expected since the nanobeam was etched with a relatively low current (for higher precision).

In Tab. 5.1, calculated precision and accuracy levels are presented based on data in Fig. 5.33. The precision gives information about the clustering (consistency) of placed nanobeams, while accuracy is about correctness (proximity to the true value) - the nanobeam, on average, is shifted 18 nm from the center to the right (in the presented planar view). The y-axis and angular precision were not studied methodologically since the y-position has a lower influence on the coupling efficiency than the x-position, and the angular twist of nanobeams is not easily detectable.

Threshold	Precision	Accuracy
Top 10%	< 10 nm	18(1) nm
1 σ	< 70 nm	18(9) nm
3 σ	< 200 nm	18(27) nm

TABLE 5.1: Precision and accuracy levels for different statistical thresholds: top 10%, 1 σ, and 3 σ.

5.5 High-throughput µTP

One of the biggest advantages of µTP over classical pick-and-place methods using, e.g. FIB, is that µTP can be highly automated and the transfer can happen automatically. The last part of the results is devoted to achieving the automatic transfer printing process.

As seen in the mask file in Fig. 5.2 a), the source nanobeams are fabricated in a regular quadratic grid with a spacing of 125 µm in the x- and 125 µm in the y-axes. This equal spacing allowed for an easy definition of a grid for an automatic transfer over which the stamp should automatically position itself.

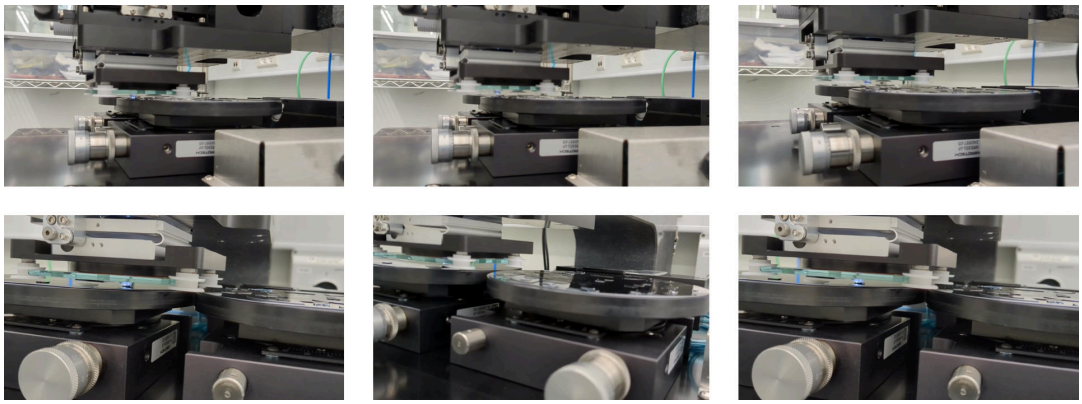

FIGURE 5.34: Process of the automatic transfer without any user input with a cycle time of 40 s. In the picture, there are visible two stages on which there are mounted source and target chips.

For the target, SiN waveguides were chosen from Chapt. 5.2 and the printing process was defined to be done along its length with 80 µm spacing. As seen in Fig. 5.35

FIGURE 5.35: InP nanobeams automatically transferred to the SiN waveguides. There is no visible misalignment under the optical microscope.

The one cycle of a device transfer was optimized to be 40 s, so the fabrication throughput is about 90 devices per hour. The yield of the transfer, defined as the ratio of transferred devices to the number of devices, was over 90% for a sample of over 100 transferred nanobeams.

Chapter 6

Summary and conclusions

Direct bonding and micro-transfer printing have been shown to be effective, robust, and flexible techniques for heterogeneous integration of semiconductor materials, especially of InP 1D PhCC with InAs/InP quantum dots with SOI, SiN platforms or metal-contacts. In the introductory chapters, the motivation behind the development and characterization of the structures for processing and transmission of a quantum state for quantum information technologies was outlined. Multiple fabrication and experimental techniques were presented, paired with the analysis that allowed deriving a number of characteristics and parameters of the fabricated devices.

Main findings

The main findings of the thesis can be outlined as follows:

- Direct bonding is a viable technique for the scalable integration of InAs/InP QD with the SOI platform, allowing for the highly integrated quantum photonic chips. Characterized selected devices provided the information on the excitonic complexes (trions, excitons, and biexcitons) and the on-chip directional coupling efficiency at the level of 5.1%. This emission from the devices was measured using custom built experimental setups allowing for the measurements from the chip edge and from the circular Bragg grating while exciting the QD inside a InP waveguide through second microscope objective, proving that it is viable approach to study qPIC in cryogenic temperatures Autocorrelation measurements allowed for the determination of the single-photon purity which was a the level of 98% (background corrected) which is a requirement for the efficient on-chip operations on single photons.

- There was presented the design and fabrication steps necessary to fabricate all-fiber plug-and-play triggered single-photon source emitting in the telecom C-Band. This source was optically characterized and maintained its single-photon purity at the level of 73% monitored for 42 hours in a alignment-free setup. Used closed-cycle cryocooler and transmission between two laboratory nodes through the open-field is prospective for more real-world applications. To the Author knowledge, this device is the first demonstration of all-fiber

plug-and-play single-photon source based on QDs emitting in the telecom C-band.

- The developed protocol for micro-transfer printing allowed for an accurate (< 70 nm) and precise (18(9) nm) deterministic transfer of the individual InP nanobeams with InAs/InP QDs inside 1D photonic crystal cavities to various material platforms such as SOI, SiN, single-mode fibers, InP, and metal contacts. Not only with top-down integration but also from a side allowing for a direct docking to the host waveguide.

- µTP integration of InP nanobeams with the SOI platform with Si waveguides and grating outcouplers allowed for the demonstration coupling of light to the PIC chip. This deterministic transfer allows for a preselection of a suitable device and its integration with PIC not only limited to the QD single-photon sources but also for e.g., nanolasers, especially paired with the proven possibility to form electrical contact after transferring the device onto a metal contacts.

These main findings support that the research presented in this thesis features direct bonding and, especially, micro-transfer printing as a universal integration technique for the development of quantum photonic integrated circuits.

Acknowledgements

I would like to express my deep gratitude to my supervisors Dr. Paweł Mrowiński and Assoc. Prof. Marcin Syperek, they professionally supervised my work with positive attitude for a few years, giving me a guidance and sharing their expertise. I greatly appreciate their dedication.

I would also like to greatly thank Dr. Paweł Holewa, Dr. Elizaveta Semenova and Prof. Kresten Yvind for their warm welcoming and support during the work at DTU. Their professionalism and expertise were instrumental for the work presented in this thesis.

My deepest gratitude goes towards my wife Monika, who is always there for me, with love.

Bibliography

1. Dietrich, C. P., Fiore, A., Thompson, M. G., Kamp, M. & Höfling, S. GaAs integrated quantum photonics: Towards compact and multi-functional quantum photonic integrated circuits. *Laser & Photonics Reviews* **10,** 870–894. ISSN: 1863-8899. http://dx.doi.org/10.1002/lpor.201500321 (Sept. 2016).
2. Hepp, S., Jetter, M., Portalupi, S. L. & Michler, P. Semiconductor Quantum Dots for Integrated Quantum Photonics. *Advanced Quantum Technologies* **2.** ISSN: 2511-9044. http://dx.doi.org/10.1002/qute.201900020 (July 2019).
3. Pelucchi, E. *et al.* The potential and global outlook of integrated photonics for quantum technologies. *Nature Reviews Physics* **4,** 194–208. https://doi.org/10.1038/s42254-021-00398-z (Dec. 2021).
4. Wang, J., Sciarrino, F., Laing, A. & Thompson, M. G. Integrated photonic quantum technologies. *Nature Photonics* **14,** 273–284. https://doi.org/10.1038/s41566-019-0532-1 (Oct. 2019).
5. Elshaari, A. W., Pernice, W., Srinivasan, K., Benson, O. & Zwiller, V. Hybrid integrated quantum photonic circuits. *Nature Photonics* **14,** 285–298. ISSN: 1749-4893. http://dx.doi.org/10.1038/s41566-020-0609-x (Apr. 2020).
6. Kim, J.-H., Aghaeimeibodi, S., Carolan, J., Englund, D. & Waks, E. Hybrid integration methods for on-chip quantum photonics. *Optica* **7,** 291. ISSN: 2334-2536. http://dx.doi.org/10.1364/OPTICA.384118 (Apr. 2020).
7. Uppu, R., Midolo, L., Zhou, X., Carolan, J. & Lodahl, P. Quantum-dot-based deterministic photon–emitter interfaces for scalable photonic quantum technology. *Nature Nanotechnology* **16,** 1308–1317. ISSN: 1748-3395. http://dx.doi.org/10.1038/s41565-021-00965-6 (Oct. 2021).
8. Awschalom, D. *et al.* Development of Quantum Interconnects (QuICs) for Next-Generation Information Technologies. *PRX Quantum* **2.** ISSN: 2691-3399. http://dx.doi.org/10.1103/PRXQuantum.2.017002 (Feb. 2021).
9. Dirac, P. *The Principles of Quantum Mechanics* ISBN: 9780198520115. https://books.google.pl/books?id=XehUpGiM6FIC (Clarendon Press, 1981).
10. Einstein, A., Podolsky, B. & Rosen, N. Can Quantum-Mechanical Description of Physical Reality Be Considered Complete? *Physical Review* **47,** 777–780. ISSN: 0031-899X. http://dx.doi.org/10.1103/PhysRev.47.777 (May 1935).

11. Georgescu, I. M., Ashhab, S. & Nori, F. Quantum simulation. *Reviews of Modern Physics* **86,** 153–185. ISSN: 1539-0756. http://dx.doi.org/10.1103/RevModPhys.86.153 (Mar. 2014).

12. Grover, L. K. Quantum Mechanics Helps in Searching for a Needle in a Haystack. *Physical Review Letters* **79,** 325–328. ISSN: 1079-7114. http://dx.doi.org/10.1103/PhysRevLett.79.325 (July 1997).

13. Somhorst, F. H. B. *et al.* Quantum simulation of thermodynamics in an integrated quantum photonic processor. *Nature Communications* **14.** ISSN: 2041-1723. http://dx.doi.org/10.1038/s41467-023-38413-9 (July 2023).

14. Zhong, H.-S. *et al.* Quantum computational advantage using photons. *Science* **370,** 1460–1463. ISSN: 1095-9203. http://dx.doi.org/10.1126/science.abe8770 (Dec. 2020).

15. Shekhar, S. *et al.* Roadmapping the next generation of silicon photonics. *Nature Communications* **15.** ISSN: 2041-1723. http://dx.doi.org/10.1038/s41467-024-44750-0 (Jan. 2024).

16. Kahl, O. *et al.* Waveguide integrated superconducting single-photon detectors with high internal quantum efficiency at telecom wavelengths. *Scientific Reports* **5,** 10941. ISSN: 2045-2322. https://doi.org/10.1038/srep10941 (June 2015).

17. Uppu, R. *et al.* Scalable integrated single-photon source. *Science Advances* **6.** ISSN: 2375-2548. http://dx.doi.org/10.1126/sciadv.abc8268 (Dec. 2020).

18. Soref, R. *Silicon photonics technology: past, present, and future* in *Optoelectronic Integration on Silicon II* (eds Kubby, J. A. & Jabbour, G. E.) (SPIE, Mar. 2005). http://dx.doi.org/10.1117/12.585284.

19. Li, R., Liu, F. & Lu, Q. Quantum Light Source Based on Semiconductor Quantum Dots: A Review. *Photonics* **10,** 639. ISSN: 2304-6732. http://dx.doi.org/10.3390/photonics10060639 (June 2023).

20. Schimpf, C. *et al.* Quantum dots as potential sources of strongly entangled photons: Perspectives and challenges for applications in quantum networks. *Applied Physics Letters* **118.** ISSN: 1077-3118. http://dx.doi.org/10.1063/5.0038729 (Mar. 2021).

21. Katsumi, R. *et al.* In situ wavelength tuning of quantum-dot single-photon sources integrated on a CMOS-processed silicon waveguide. *Applied Physics Letters* **116.** ISSN: 1077-3118. http://dx.doi.org/10.1063/1.5129325 (Jan. 2020).

22. Burakowski, M. *et al.* Heterogeneous integration of single InAs/InP quantum dots with the SOI chip using direct bonding. *Optics Express* **32,** 10874. ISSN: 1094-4087. http://dx.doi.org/10.1364/OE.515223 (Mar. 2024).

23. Mikulicz, M. G. *et al. InAs/InP quantum dot based C-Band all-fiber plug-and-play triggered single-photon source integrated using micro-transfer printing* 2024. arXiv: 2411.16490 [physics.optics]. https://arxiv.org/abs/2411.16490.

24. Arakawa, Y. & Sakaki, H. Multidimensional quantum well laser and temperature dependence of its threshold current. *Applied Physics Letters* **40,** 939–941. ISSN: 1077-3118. http://dx.doi.org/10.1063/1.92959 (June 1982).

25. Asada, M., Miyamoto, Y. & Suematsu, Y. Gain and the threshold of three-dimensional quantum-box lasers. *IEEE Journal of Quantum Electronics* **22,** 1915–1921. ISSN: 0018-9197. http://dx.doi.org/10.1109/JQE.1986.1073149 (Sept. 1986).

26. Chou, S.-T., Wu, M.-C., Lin, S.-Y. & Chi, J.-Y. Influence of doping density on the normal incident absorption of quantum-dot infrared photodetectors. *Applied Physics Letters* **88.** ISSN: 1077-3118. http://dx.doi.org/10.1063/1.2199589 (Apr. 2006).

27. Bhattacharya, P., Su, X. H., Chakrabarti, S., Ariyawansa, G. & Perera, A. G. U. Characteristics of a tunneling quantum-dot infrared photodetector operating at room temperature. *Applied Physics Letters* **86.** ISSN: 1077-3118. http://dx.doi.org/10.1063/1.1923766 (May 2005).

28. Balocco, C., Song, A. M. & Missous, M. Room-temperature operations of memory devices based on self-assembled InAs quantum dot structures. *Applied Physics Letters* **85,** 5911–5913. ISSN: 1077-3118. http://dx.doi.org/10.1063/1.1831558 (Dec. 2004).

29. Pelton, M. *et al.* Efficient Source of Single Photons: A Single Quantum Dot in a Micropost Microcavity. *Physical Review Letters* **89.** ISSN: 1079-7114. http://dx.doi.org/10.1103/physrevlett.89.233602 (Nov. 2002).

30. Fattal, D. *et al.* Entanglement Formation and Violation of Bell's Inequality with a Semiconductor Single Photon Source. *Physical Review Letters* **92.** ISSN: 1079-7114. http://dx.doi.org/10.1103/physrevlett.92.037903 (Jan. 2004).

31. Li, X. *et al.* An All-Optical Quantum Gate in a Semiconductor Quantum Dot. *Science* **301,** 809–811. ISSN: 1095-9203. http://dx.doi.org/10.1126/science.1083800 (Aug. 2003).

32. Zrenner, A. *et al.* Coherent properties of a two-level system based on a quantum-dot photodiode. *Nature* **418,** 612–614. ISSN: 1476-4687. http://dx.doi.org/10.1038/nature00912 (Aug. 2002).

33. Han, J. *et al.* Toward high-resolution, inkjet-printed, quantum dot light-emitting diodes for next-generation displays. *Journal of the Society for Information Display* **24,** 545–551. ISSN: 1938-3657. http://dx.doi.org/10.1002/jsid.467 (Sept. 2016).

34. Santaella, J. J., Critchley, K., Rodríguez-Bolívar, S. & Gómez-Campos, F. M. Design and fabrication of CuInS2/ZnS-based QLED for automotive lighting systems. *Nanotechnology* **32,** 105204. ISSN: 1361-6528. http://dx.doi.org/10.1088/1361-6528/abcced (Dec. 2020).

35. Kim, J.-H. *et al.* Hybrid Integration of Solid-State Quantum Emitters on a Silicon Photonic Chip. *Nano Letters* **17,** 7394–7400. https://doi.org/10.1021/acs.nanolett.7b03220 (Nov. 2017).

36. Reithmaier, J. P. *et al.* Strong coupling in a single quantum dot–semiconductor microcavity system. *Nature* **432,** 197–200. ISSN: 1476-4687. http://dx.doi.org/10.1038/nature02969 (Nov. 2004).

37. Hennessy, K. *et al.* Quantum nature of a strongly coupled single quantum dot–cavity system. *Nature* **445,** 896–899. ISSN: 1476-4687. http://dx.doi.org/10.1038/nature05586 (Jan. 2007).

38. Bechtold, A. *et al.* Three-stage decoherence dynamics of an electron spin qubit in an optically active quantum dot. *Nature Physics* **11,** 1005–1008. ISSN: 1745-2481. http://dx.doi.org/10.1038/nphys3470 (Sept. 2015).

39. Wüst, G. *et al.* Role of the electron spin in determining the coherence of the nuclear spins in a quantum dot. *Nature Nanotechnology* **11,** 885–889. ISSN: 1748-3395. http://dx.doi.org/10.1038/nnano.2016.114 (July 2016).

40. Stinaff, E. A. *et al.* Optical Signatures of Coupled Quantum Dots. *Science* **311,** 636–639. ISSN: 1095-9203. http://dx.doi.org/10.1126/science.1121189 (Feb. 2006).

41. Kim, D., Carter, S. G., Greilich, A., Bracker, A. S. & Gammon, D. Ultrafast optical control of entanglement between two quantum-dot spins. *Nature Physics* **7,** 223–229. ISSN: 1745-2481. http://dx.doi.org/10.1038/nphys1863 (Dec. 2010).

42. Chow, C. M. *et al.* Nonlocal Nuclear Spin Quieting in Quantum Dot Molecules: Optically Induced Extended Two-Electron Spin Coherence Time. *Physical Review Letters* **117.** ISSN: 1079-7114. http://dx.doi.org/10.1103/PhysRevLett.117.077403 (Aug. 2016).

43. Shchukin, V. A., Ledentsov, N. N. & Bimberg, D. *Epitaxy of Nanostructures* ISBN: 9783662070666. http://dx.doi.org/10.1007/978-3-662-07066-6 (Springer Berlin Heidelberg, 2004).

44. Tartakovskii, A. *Quantum Dots: Optics, Electron Transport and Future Applications* ISBN: 9781107012585. https://books.google.pl/books?id=HwZqX_RSp18C (Cambridge University Press, 2012).

45. Berdnikov, Y. *et al.* Near-critical Stranski-Krastanov growth of InAs/InP quantum dots. *Scientific Reports* **14.** ISSN: 2045-2322. http://dx.doi.org/10.1038/s41598-024-70451-1 (Oct. 2024).

46. Holewa, P. *et al.* Bright Quantum Dot Single-Photon Emitters at Telecom Bands Heterogeneously Integrated on Si. *ACS Photonics* **9,** 2273–2279. ISSN: 2330-4022. http://dx.doi.org/10.1021/acsphotonics.2c00027 (June 2022).

47. Mano, T. *et al.* Ultra-narrow emission from single GaAs self-assembled quantum dots grown by droplet epitaxy. *Nanotechnology* **20,** 395601. ISSN: 1361-6528. http://dx.doi.org/10.1088/0957-4484/20/39/395601 (Sept. 2009).

48. Sears, K., Tan, H. H., Wong-Leung, J. & Jagadish, C. The role of arsine in the self-assembled growth of InAs/GaAs quantum dots by metal organic chemical vapor deposition. *Journal of Applied Physics* **99.** ISSN: 1089-7550. http://dx.doi.org/10.1063/1.2173687 (Feb. 2006).

49. Heinrichsdorff, F., Krost, A., Bimberg, D., Kosogov, A. & Werner, P. Self organized defect free InAs/GaAs and InAs/InGaAs/GaAs quantum dots with high lateral density grown by MOCVD. *Applied Surface Science* **123–124,** 725–728. ISSN: 0169-4332. http://dx.doi.org/10.1016/s0169-4332(97)00476-5 (Jan. 1998).

50. El-Emawy, A. A. *et al.* Formation trends in quantum dot growth using metalorganic chemical vapor deposition. *Journal of Applied Physics* **93,** 3529–3534. ISSN: 1089-7550. http://dx.doi.org/10.1063/1.1543647 (Mar. 2003).

51. Ledentsov, N. *et al.* MBE-grown metamorphic lasers for applications at telecom wavelengths. *Journal of Crystal Growth* **301–302,** 914–922. ISSN: 0022-0248. http://dx.doi.org/10.1016/j.jcrysgro.2006.09.035 (Apr. 2007).

52. Semenova, E. S. *et al.* Metamorphic approach to single quantum dot emission at 1.55 μm on GaAs substrate. *Journal of Applied Physics* **103.** ISSN: 1089-7550. http://dx.doi.org/10.1063/1.2927496 (May 2008).

53. Wroński, P. A. *et al.* Metamorphic Buffer Layer Platform for 1550 nm Single-Photon Sources Grown by MBE on (100) GaAs Substrate. *Materials* **14,** 5221. ISSN: 1996-1944. http://dx.doi.org/10.3390/ma14185221 (Sept. 2021).

54. Dion, C., Poole, P. J., Raymond, S., Desjardins, P. & Schiettekatte, F. Tuning of the electronic properties of self-assembled InAs/InP(001) quantum dots using grown-in defect mediated intermixing. *Applied Physics Letters* **89.** ISSN: 1077-3118. http://dx.doi.org/10.1063/1.2357162 (Sept. 2006).

55. Tomlins, P. H. & Wang, R. K. Theory, developments and applications of optical coherence tomography. *Journal of Physics D: Applied Physics* **38,** 2519–2535. ISSN: 1361-6463. http://dx.doi.org/10.1088/0022-3727/38/15/002 (July 2005).

56. Pettersson, H., Bååth, L., Carlsson, N., Seifert, W. & Samuelson, L. Case study of an InAs quantum dot memory: Optical storing and deletion of charge. *Applied Physics Letters* **79,** 78–80. ISSN: 1077-3118. http://dx.doi.org/10.1063/1.1382628 (July 2001).

57. Peng, Q. *et al.* First-Principles Assessment of the Structure and Stability of 15 Intrinsic Point Defects in Zinc-Blende Indium Arsenide. *Crystals* **9,** 48. ISSN: 2073-4352. http://dx.doi.org/10.3390/cryst9010048 (Jan. 2019).

58. People, R. & Sputz, S. K. Band nonparabolicities in lattice-mismatch-strained bulk semiconductor layers. *Phys. Rev. B* **41,** 8431–8439. https://link.aps.org/doi/10.1103/PhysRevB.41.8431 (12 Apr. 1990).

59. Dusanowski, Ł. *et al.* Single-photon emission of InAs/InP quantum dashes at 1.55 μm and temperatures up to 80 K. *Applied Physics Letters* **108.** ISSN: 1077-3118. http://dx.doi.org/10.1063/1.4947448 (Apr. 2016).

60. Müller, T. *et al.* A quantum light-emitting diode for the standard telecom window around 1,550 nm. *Nature Communications* **9,** 862. ISSN: 2041-1723. https://doi.org/10.1038/s41467-018-03251-7 (Feb. 2018).

61. Gong, M., Zhang, W., Can Guo, G. & He, L. Atomistic pseudopotential theory of optical properties of exciton complexes in InAs/InP quantum dots. *Applied Physics Letters* **99.** ISSN: 1077-3118. http://dx.doi.org/10.1063/1.3669507 (Dec. 2011).

62. Siegert, J. *Carrier dynamics in semiconductor quantum dots* in (2006). https://api.semanticscholar.org/CorpusID:115806489.

63. Bayer, M. *et al.* Fine structure of neutral and charged excitons in self-assembled In(Ga)As/(Al)GaAs quantum dots. *Phys. Rev. B* **65,** 195315. https://link.aps.org/doi/10.1103/PhysRevB.65.195315 (19 May 2002).

64. Moody, G. *et al. Electronic Control of Exciton Coherence in a Charged Quantum Dot Photonic Waveguide* in *Conference on Lasers and Electro-Optics* (OSA, 2016), JW2A.36. http://dx.doi.org/10.1364/CLEO_AT.2016.JW2A.36.

65. Shah, J. *Ultrafast Spectroscopy of Semiconductors and Semiconductor Nanostructures* ISBN: 9783662037706. http://dx.doi.org/10.1007/978-3-662-03770-6 (Springer Berlin Heidelberg, 1999).

66. Contreras-Pulido, L. D., Splettstoesser, J., Governale, M., König, J. & Büttiker, M. Time scales in the dynamics of an interacting quantum dot. *Physical Review B* **85.** ISSN: 1550-235X. http://dx.doi.org/10.1103/PhysRevB.85.075301 (Feb. 2012).

67. Gong, Y.-X., Zou, X.-B., Ralph, T. C., Zhu, S.-N. & Guo, G.-C. Linear optical quantum computation with imperfect entangled photon-pair sources and inefficient non–photon-number-resolving detectors. *Physical Review A* **81.** ISSN: 1094-1622. http://dx.doi.org/10.1103/PhysRevA.81.052303 (May 2010).

68. Sanchez-Mondragon, J. J., Narozhny, N. B. & Eberly, J. H. Theory of Spontaneous-Emission Line Shape in an Ideal Cavity. *Physical Review Letters* **51,** 550–553. ISSN: 0031-9007. http://dx.doi.org/10.1103/PhysRevLett.51.550 (Aug. 1983).

69. Agarwal, G. S. Spectroscopy of strongly coupled atom-cavity systems: A topical review. *Journal of Modern Optics* **45,** 449–470. ISSN: 1362-3044. http://dx.doi.org/10.1080/09500349808231908 (Mar. 1998).

70. Abbarchi, M. *et al.* Fine structure splitting of quantum dot excitons: Role of geometry and environment. *Physica E: Low-dimensional Systems and Nanostructures* **42,** 881–883. ISSN: 1386-9477. http://dx.doi.org/10.1016/j.physe.2009.11.033 (Feb. 2010).

71. Holewa, P. *et al.* Thermal stability of emission from single InGaAs/GaAs quantum dots at the telecom O-band. *Scientific Reports* **10.** ISSN: 2045-2322. http://dx.doi.org/10.1038/s41598-020-78462-4 (Dec. 2020).

72. Baier, M. H., Malko, A., Pelucchi, E., Oberli, D. Y. & Kapon, E. Quantum-dot exciton dynamics probed by photon-correlation spectroscopy. *Physical Review B* **73.** https://doi.org/10.1103/physrevb.73.205321 (May 2006).

73. Abbarchi, M. *et al.* Poissonian statistics of excitonic complexes in quantum dots. *Journal of Applied Physics* **106.** https://doi.org/10.1063/1.3197848 (Sept. 2009).

74. Mrowiński, P. *et al.* Directional Emission of a Deterministically Fabricated Quantum Dot–Bragg Reflection Multimode Waveguide System. *ACS Photonics* **6,** 2231–2237. https://doi.org/10.1021/acsphotonics.9b00369 (July 2019).

75. Ediger, M. *et al.* Peculiar many-body effects revealed in the spectroscopy of highly charged quantum dots. *Nature Physics* **3,** 774–779. ISSN: 1745-2481. http://dx.doi.org/10.1038/nphys748 (Oct. 2007).

76. Bennett, A. J. *et al.* Electric-field-induced coherent coupling of the exciton states in a single quantum dot. *Nature Physics* **6,** 947–950. ISSN: 1745-2481. http://dx.doi.org/10.1038/nphys1780 (Oct. 2010).

77. Callsen, G. & Pahn, G. M. O. Identifying multi-excitons in quantum dots: the subtle connection between electric dipole moments and emission linewidths. *physica status solidi (RRL) - Rapid Research Letters* **9,** 521–525. ISSN: 1862-6254. http://dx.doi.org/10.1002/pssr.201510253 (Sept. 2015).

78. Hönig, G. *et al.* Identification of electric dipole moments of excitonic complexes in nitride-based quantum dots. *Physical Review B* **88.** ISSN: 1550-235X. http://dx.doi.org/10.1103/PhysRevB.88.045309 (July 2013).

79. Jansson, M., La, R., Tu, C. W., Chen, W. M. & Buyanova, I. A. Exciton generation and recombination dynamics of quantum dots embedded in GaNAsP nanowires. *Physical Review B* **103.** ISSN: 2469-9969. http://dx.doi.org/10.1103/PhysRevB.103.165425 (Apr. 2021).

80. Shirane, M. *et al.* Charged and neutral biexciton–exciton cascade in a single quantum dot within a photonic bandgap. *Physica E: Low-dimensional Systems and Nanostructures* **42,** 2563–2566. ISSN: 1386-9477. http://dx.doi.org/10.1016/j.physe.2010.02.031 (Sept. 2010).

81. Dalgarno, P. A. *et al.* Dark exciton decay dynamics of a semiconductor quantum dot. *physica status solidi (a)* **202,** 2591–2597. ISSN: 1862-6319. http://dx.doi.org/10.1002/pssa.200562029 (Nov. 2005).

82. Olbrich, F. *et al.* Temperature-dependent properties of single long-wavelength InGaAs quantum dots embedded in a strain reducing layer. *Journal of Applied Physics* **121.** https://doi.org/10.1063/1.4983362 (May 2017).

83. Ediger, M. *et al.* Controlled generation of neutral, negatively-charged and positively-charged excitons in the same single quantum dot. *Applied Physics Letters* **86.** ISSN: 1077-3118. http://dx.doi.org/10.1063/1.1937996 (May 2005).

84. Miyazawa, T. *et al.* Effect of electronic structure on single-photon emission in InAs/InP quantum dot with quasi-resonant excitation. *physica status solidi c* **8,** 417–419. ISSN: 1610-1642. http://dx.doi.org/10.1002/pssc.201000590 (Jan. 2011).

85. Diederichs, C. *The resonance fluorescence of single semiconductor quantum dots for the generation of indistinguishable photons.* Habilitation à diriger des recherches (Université Pierre et Marie Curie (UPMC), Dec. 2016). https://theses.hal.science/tel-01416901.

86. Burakowski, M. *et al.* Diamagnetic coefficients and g-factors of InAs/InGaAlAs quantum dashes emitting at telecom wavelengths. *Journal of Applied Physics* **132.** ISSN: 1089-7550. http://dx.doi.org/10.1063/5.0101345 (Oct. 2022).

87. Rudno-Rudziński, W., Burakowski, M., Reithmaier, J. P., Musiał, A. & Benyoucef, M. Magneto-Optical Characterization of Trions in Symmetric InP-Based Quantum Dots for Quantum Communication Applications. *Materials* **14,** 942. ISSN: 1996-1944. http://dx.doi.org/10.3390/ma14040942 (Feb. 2021).

88. Koudinov, A. V., Akimov, I. A., Kusrayev, Y. G. & Henneberger, F. Optical and magnetic anisotropies of the hole states in Stranski-Krastanov quantum dots. *Physical Review B* **70.** ISSN: 1550-235X. http://dx.doi.org/10.1103/PhysRevB.70.241305 (Dec. 2004).

89. Bennett, A. J. *et al.* Voltage tunability of single-spin states in a quantum dot. *Nature Communications* **4.** ISSN: 2041-1723. http://dx.doi.org/10.1038/ncomms2519 (Feb. 2013).

90. Brassard, G., Lütkenhaus, N., Mor, T. & Sanders, B. C. Limitations on Practical Quantum Cryptography. *Physical Review Letters* **85,** 1330–1333. ISSN: 1079-7114. http://dx.doi.org/10.1103/PhysRevLett.85.1330 (Aug. 2000).

91. Broome, M. A. *et al.* Photonic Boson Sampling in a Tunable Circuit. *Science* **339,** 794–798. ISSN: 1095-9203. http://dx.doi.org/10.1126/science.1231440 (Feb. 2013).

92. Spring, J. B. *et al.* Boson Sampling on a Photonic Chip. *Science* **339,** 798–801. ISSN: 1095-9203. http://dx.doi.org/10.1126/science.1231692 (Feb. 2013).

93. Spagnolo, N. *et al.* Experimental validation of photonic boson sampling. *Nature Photonics* **8,** 615–620. ISSN: 1749-4893. http://dx.doi.org/10.1038/nphoton.2014.135 (June 2014).

94. Tillmann, M. *et al.* Experimental boson sampling. *Nature Photonics* **7,** 540–544. ISSN: 1749-4893. http://dx.doi.org/10.1038/nphoton.2013.102 (May 2013).

95. Hong, C. K., Ou, Z. Y. & Mandel, L. Measurement of subpicosecond time intervals between two photons by interference. *Physical Review Letters* **59,** 2044–2046. ISSN: 0031-9007. http://dx.doi.org/10.1103/PhysRevLett.59.2044 (Nov. 1987).

96. Prilmüller, M. *et al.* Hyperentanglement of Photons Emitted by a Quantum Dot. *Physical Review Letters* **121.** ISSN: 1079-7114. http://dx.doi.org/10.1103/PhysRevLett.121.110503 (Sept. 2018).

97. Huber, D. *et al.* Strain-Tunable GaAs Quantum Dot: A Nearly Dephasing-Free Source of Entangled Photon Pairs on Demand. *Physical Review Letters* **121.** ISSN: 1079-7114. http://dx.doi.org/10.1103/PhysRevLett.121.033902 (July 2018).

98. Bartolucci, S. *et al.* Fusion-based quantum computation. en. *Nat. Commun.* **14,** 912 (Feb. 2023).

99. Dawson, C. M., Haselgrove, H. L. & Nielsen, M. A. Noise thresholds for optical quantum computers. en. *Phys. Rev. Lett.* **96,** 020501 (Jan. 2006).

100. Madigawa, A. A. *et al.* Assessing the Alignment Accuracy of State-of-the-Art Deterministic Fabrication Methods for Single Quantum Dot Devices. *ACS Photonics* **11,** 1012–1023. ISSN: 2330-4022. http://dx.doi.org/10.1021/acsphotonics.3c01368 (Feb. 2024).

101. Holewa, P. *et al.* High-throughput quantum photonic devices emitting indistinguishable photons in the telecom C-band. *Nature Communications* **15.** ISSN: 2041-1723. http://dx.doi.org/10.1038/s41467-024-47551-7 (Apr. 2024).

102. Schweickert, L. *et al.* On-demand generation of background-free single photons from a solid-state source. *Applied Physics Letters* **112,** 093106. ISSN: 0003-6951. https://doi.org/10.1063/1.5020038 (Feb. 2018).

103. Somaschi, N. *et al.* Near-optimal single-photon sources in the solid state. *Nature Photonics* **10,** 340–345. https://doi.org/10.1038/nphoton.2016.23 (Mar. 2016).

104. Rahaman, M. H. *et al.* Efficient, Indistinguishable Telecom C-Band Photons using a Tapered Nanobeam Waveguide. *ACS Photonics* **11,** 2738–2744. ISSN: 2330-4022. http://dx.doi.org/10.1021/acsphotonics.4c00625 (June 2024).

105. Pennacchietti, M. *et al.* Oscillating photonic Bell state from a semiconductor quantum dot for quantum key distribution. *Communications Physics* **7.** ISSN: 2399-3650. http://dx.doi.org/10.1038/s42005-024-01547-3 (Feb. 2024).

106. Tomm, N. *et al.* A bright and fast source of coherent single photons. *Nature Nanotechnology* **16,** 399–403. ISSN: 1748-3395. http://dx.doi.org/10.1038/s41565-020-00831-x (Jan. 2021).

107. Dusanowski, Ł., Köck, D., Schneider, C. & Höfling, S. On-Chip Hong–Ou–Mandel Interference from Separate Quantum Dot Emitters in an Integrated Circuit. *ACS Photonics* **10,** 2941–2947. ISSN: 2330-4022. http://dx.doi.org/10.1021/acsphotonics.3c00679 (June 2023).

108. Larocque, H. *et al.* Tunable quantum emitters on large-scale foundry silicon photonics. *Nature Communications* **15.** ISSN: 2041-1723. http://dx.doi.org/10.1038/s41467-024-50208-0 (July 2024).

109. Neergaard-Nielsen, J. S., Nielsen, B. M., Takahashi, H., Vistnes, A. I. & Polzik, E. S. High purity bright single photon source. *Optics Express* **15,** 7940. ISSN: 1094-4087. http://dx.doi.org/10.1364/OE.15.007940 (2007).

110. Ding, X. *et al.* On-Demand Single Photons with High Extraction Efficiency and Near-Unity Indistinguishability from a Resonantly Driven Quantum Dot in a Micropillar. *Physical Review Letters* **116.** https://doi.org/10.1103/physrevlett.116.020401 (Jan. 2016).

111. Liu, F. *et al.* High Purcell factor generation of indistinguishable on-chip single photons. *Nature Nanotechnology* **13,** 835–840. ISSN: 1748-3395. http://dx.doi.org/10.1038/s41565-018-0188-x (July 2018).

112. Claudon, J. *et al.* A highly efficient single-photon source based on a quantum dot in a photonic nanowire. *Nature Photonics* **4,** 174–177. https://doi.org/10.1038/nphoton.2009.287x (Jan. 2010).

113. Bounouar, S. *et al.* Ultrafast Room Temperature Single-Photon Source from Nanowire-Quantum Dots. *Nano Letters* **12,** 2977–2981. ISSN: 1530-6992. http://dx.doi.org/10.1021/nl300733f (May 2012).

114. Munsch, M. *et al.* Dielectric GaAs Antenna Ensuring an Efficient Broadband Coupling between an InAs Quantum Dot and a Gaussian Optical Beam. *Physical Review Letters* **110.** ISSN: 1079-7114. http://dx.doi.org/10.1103/PhysRevLett.110.177402 (Apr. 2013).

115. Jöns, K. D. *et al.* Bright nanoscale source of deterministic entangled photon pairs violating Bell's inequality. *Scientific Reports* **7.** ISSN: 2045-2322. http://dx.doi.org/10.1038/s41598-017-01509-6 (May 2017).

116. Bulgarini, G. *et al.* Nanowire Waveguides Launching Single Photons in a Gaussian Mode for Ideal Fiber Coupling. *Nano Letters* **14,** 4102–4106. ISSN: 1530-6992. http://dx.doi.org/10.1021/nl501648f (June 2014).

117. Holmes, M. J., Choi, K., Kako, S., Arita, M. & Arakawa, Y. Room-Temperature Triggered Single Photon Emission from a III-Nitride Site-Controlled Nanowire Quantum Dot. *Nano Letters* **14,** 982–986. ISSN: 1530-6992. http://dx.doi.org/10.1021/nl404400d (Jan. 2014).

118. Thomas, S. E. *et al.* Bright Polarized Single-Photon Source Based on a Linear Dipole. *Physical Review Letters* **126.** ISSN: 1079-7114. http://dx.doi.org/10.1103/PhysRevLett.126.233601 (June 2021).

119. Lodahl, P. *et al.* Controlling the dynamics of spontaneous emission from quantum dots by photonic crystals. *Nature* **430,** 654–657. ISSN: 1476-4687. http://dx.doi.org/10.1038/nature02772 (Aug. 2004).

120. Pernice, W. H. P., Xiong, C., Schuck, C. & Tang, H. X. High-Q aluminum nitride photonic crystal nanobeam cavities. *Applied Physics Letters* **100.** ISSN: 1077-3118. http://dx.doi.org/10.1063/1.3690888 (Feb. 2012).

121. Schröder, T. *et al.* Scalable fabrication of coupled NV center - photonic crystal cavity systems by self-aligned N ion implantation. *Optical Materials Express* **7,** 1514. ISSN: 2159-3930. http://dx.doi.org/10.1364/OME.7.001514 (Apr. 2017).

122. Ates, S., Sapienza, L., Davanco, M., Badolato, A. & Srinivasan, K. Bright Single-Photon Emission From a Quantum Dot in a Circular Bragg Grating Microcavity. *IEEE Journal of Selected Topics in Quantum Electronics* **18,** 1711–1721. ISSN: 1558-4542. http://dx.doi.org/10.1109/jstqe.2012.2193877 (Nov. 2012).

123. Liu, J. *et al.* A solid-state source of strongly entangled photon pairs with high brightness and indistinguishability. *Nature Nanotechnology* **14,** 586–593. ISSN: 1748-3395. http://dx.doi.org/10.1038/s41565-019-0435-9 (Apr. 2019).

124. Barbiero, A. *et al.* Design study for an efficient semiconductor quantum light source operating in the telecom C-band based on an electrically-driven circular Bragg grating. *Optics Express* **30,** 10919. ISSN: 1094-4087. http://dx.doi.org/10.1364/OE.452328 (Mar. 2022).

125. Najer, D. *et al.* A gated quantum dot strongly coupled to an optical microcavity. *Nature* **575,** 622–627. ISSN: 1476-4687. http://dx.doi.org/10.1038/s41586-019-1709-y (Oct. 2019).

126. Northeast, D. B. *et al.* Optical fibre-based single photon source using InAsP quantum dot nanowires and gradient-index lens collection. *Scientific Reports* **11.** ISSN: 2045-2322. http://dx.doi.org/10.1038/s41598-021-02287-y (Nov. 2021).

127. Abudayyeh, H. *et al.* Single photon sources with near unity collection efficiencies by deterministic placement of quantum dots in nanoantennas. *APL Photonics* **6.** ISSN: 2378-0967. http://dx.doi.org/10.1063/5.0034863 (Mar. 2021).

128. Wang, F., Christiansen, R. E., Yu, Y., Mørk, J. & Sigmund, O. Maximizing the quality factor to mode volume ratio for ultra-small photonic crystal cavities. *Applied Physics Letters* **113.** ISSN: 1077-3118. http://dx.doi.org/10.1063/1.5064468 (Dec. 2018).

129. Vajner, D. A., Rickert, L., Gao, T., Kaymazlar, K. & Heindel, T. Quantum Communication Using Semiconductor Quantum Dots. *Advanced Quantum Technologies* **5.** ISSN: 2511-9044. http://dx.doi.org/10.1002/qute.202100116 (Apr. 2022).

130. Flamini, F., Spagnolo, N. & Sciarrino, F. Photonic quantum information processing: a review. *Reports on Progress in Physics* **82,** 016001. ISSN: 1361-6633. http://dx.doi.org/10.1088/1361-6633/aad5b2 (Nov. 2018).

131. Northup, T. E. & Blatt, R. Quantum information transfer using photons. *Nature Photonics* **8,** 356–363. ISSN: 1749-4893. http://dx.doi.org/10.1038/nphoton.2014.53 (Apr. 2014).

132. Gisin, N. & Thew, R. Quantum communication. *Nature Photonics* **1,** 165–171. https://doi.org/10.1038/nphoton.2007.22 (Mar. 2007).

133. Basso Basset, F. *et al.* Quantum teleportation with imperfect quantum dots. *npj Quantum Information* **7.** ISSN: 2056-6387. http://dx.doi.org/10.1038/s41534-020-00356-0 (Jan. 2021).

134. Ladd, T. D. *et al.* Quantum computers. *Nature* **464,** 45–53. ISSN: 1476-4687. http://dx.doi.org/10.1038/nature08812 (Mar. 2010).

135. Knill, E., Laflamme, R. & Milburn, G. J. A scheme for efficient quantum computation with linear optics. *Nature* **409,** 46–52. ISSN: 1476-4687. http://dx.doi.org/10.1038/35051009 (Jan. 2001).

136. Smit, M. *et al.* An introduction to InP-based generic integration technology. *Semiconductor Science and Technology* **29,** 083001. ISSN: 1361-6641. http://dx.doi.org/10.1088/0268-1242/29/8/083001 (June 2014).

137. Komljenovic, T. *et al.* Heterogeneous Silicon Photonic Integrated Circuits. *Journal of Lightwave Technology* **34,** 20–35. ISSN: 1558-2213. http://dx.doi.org/10.1109/JLT.2015.2465382 (Jan. 2016).

138. Halder, M. *et al.* High coherence photon pair source for quantum communication. *New Journal of Physics* **10,** 023027. ISSN: 1367-2630. http://dx.doi.org/10.1088/1367-2630/10/2/023027 (Feb. 2008).

139. Li, Q., Davanço, M. & Srinivasan, K. Efficient and low-noise single-photon-level frequency conversion interfaces using silicon nanophotonics. *Nature Photonics* **10,** 406–414. ISSN: 1749-4893. http://dx.doi.org/10.1038/nphoton.2016.64 (Apr. 2016).

140. Qiang, X. *et al.* Large-scale silicon quantum photonics implementing arbitrary two-qubit processing. *Nature Photonics* **12,** 534–539. ISSN: 1749-4893. http://dx.doi.org/10.1038/s41566-018-0236-y (Aug. 2018).

141. Schwartz, M. *et al.* Fully On-Chip Single-Photon Hanbury-Brown and Twiss Experiment on a Monolithic Semiconductor–Superconductor Platform. *Nano Letters* **18,** 6892–6897. ISSN: 1530-6992. http://dx.doi.org/10.1021/acs.nanolett.8b02794 (Oct. 2018).

142. MacQuarrie, E. R., Simon, C., Simmons, S. & Maine, E. The emerging commercial landscape of quantum computing. *Nature Reviews Physics* **2,** 596–598. ISSN: 2522-5820. http://dx.doi.org/10.1038/s42254-020-00247-5 (Oct. 2020).

143. *Handbook of optical constants of solids* (ed Palik, E. D.) https://bib-pubdb1.desy.de/record/449296 (Academic Press, Boston, 1985).

144. Vlasov, Y. A. & McNab, S. J. Losses in single-mode silicon-on-insulator strip waveguides and bends. *Optics Express* **12,** 1622. ISSN: 1094-4087. http://dx.doi.org/10.1364/OPEX.12.001622 (2004).

145. Bauters, J. F. *et al.* Ultra-low-loss high-aspect-ratio Si_3N_4 waveguides. *Optics Express* **19,** 3163. ISSN: 1094-4087. http://dx.doi.org/10.1364/OE.19.003163 (Feb. 2011).

146. Bera, A., Marin, Y., Harjanne, M., Cherchi, M. & Aalto, T. *Ultra-low loss waveguide platform in silicon photonics* in *Silicon Photonics XVII* (eds Reed, G. T. & Knights, A. P.) (SPIE, Mar. 2022), 4. http://dx.doi.org/10.1117/12.2610022.

147. Sia, J. X. B. *et al.* Wafer-Scale Demonstration of Low-Loss (0.43 dB/cm), High-Bandwidth (&38 GHz), Silicon Photonics Platform Operating at the C-Band. *IEEE Photonics Journal* **14,** 1–9. ISSN: 1943-0647. http://dx.doi.org/10.1109/JPHOT.2022.3170366 (June 2022).

148. Johnson, M., Thompson, M. G. & Sahin, D. Low-loss, low-crosstalk waveguide crossing for scalable integrated silicon photonics applications. *Optics Express* **28,** 12498. ISSN: 1094-4087. http://dx.doi.org/10.1364/OE.381304 (Apr. 2020).

149. Ye, C. & Dai, D. Ultra-Compact Broadband 2 x 2 3 dB Power Splitter Using a Subwavelength-Grating-Assisted Asymmetric Directional Coupler. *Journal of Lightwave Technology* **38,** 2370–2375. ISSN: 1558-2213. http://dx.doi.org/10.1109/JLT.2020.2973663 (Apr. 2020).

150. Liu, X. & Zhao, Y. *Ultra-broadband, compact, low-loss 3-dB power splitter using adiabatic subwavelength grating in silicon-on-insulator* in *3rd International Conference on Laser, Optics, and Optoelectronic Technology (LOPET 2023)* (eds Li, X. & Costa, M. F.) (SPIE, Aug. 2023), 51. http://dx.doi.org/10.1117/12.2690210.

151. Nguyen, V. H., Kim, I. K. & Seok, T. J. Low-Loss and Broadband Silicon Photonic 3-dB Power Splitter with Enhanced Coupling of Shallow-Etched Rib Waveguides. *Applied Sciences* **10,** 4507. ISSN: 2076-3417. http://dx.doi.org/10.3390/app10134507 (June 2020).

152. Wang, Z. *et al.* 93-THz ultra-broadband and ultra-low loss Y-junction photonic power splitter with phased inverse design. *Optics Express* **31,** 15904. ISSN: 1094-4087. http://dx.doi.org/10.1364/oe.489550 (Apr. 2023).

153. Amin, R. *et al.* Heterogeneously integrated ITO plasmonic Mach–Zehnder interferometric modulator on SOI. *Scientific Reports* **11.** ISSN: 2045-2322. http://dx.doi.org/10.1038/s41598-020-80381-3 (Jan. 2021).

154. Michaels, A. & Yablonovitch, E. Inverse design of near unity efficiency perfectly vertical grating couplers. *Optics Express* **26,** 4766. ISSN: 1094-4087. http://dx.doi.org/10.1364/OE.26.004766 (Feb. 2018).

155. Png, J. C. E. *et al. Optimized optical devices for edge-coupling-enabled silicon photonics platform* in *Silicon Photonics XIII* (eds Reed, G. T. & Knights, A. P.) (SPIE, Feb. 2018), 57. http://dx.doi.org/10.1117/12.2290313.

156. Tsuchizawa, T. *et al.* Microphotonics devices based on silicon microfabrication technology. *IEEE Journal of Selected Topics in Quantum Electronics* **11,** 232–240. ISSN: 1077-260X. http://dx.doi.org/10.1109/JSTQE.2004.841479 (Jan. 2005).

157. Wang, J. *et al.* Optimization and Demonstration of a Large-bandwidth Carrier-depletion Silicon Optical Modulator. *Journal of Lightwave Technology* **31,** 4119–4125. ISSN: 1558-2213. http://dx.doi.org/10.1109/JLT.2013.2287671 (Dec. 2013).

158. Png, C. E., Lim, S. T., Ang, T. Y. L. & Ong, J. R. *Silicon modulators for 25 Gb/s photonics platform* in *2017 Conference on Lasers and Electro-Optics Pacific Rim (CLEO-PR)* (IEEE, July 2017), 1–2. http://dx.doi.org/10.1109/CLEOPR.2017.8118905.

159. Xiao, S., Khan, M. H., Shen, H. & Qi, M. Compact silicon microring resonators with ultra-low propagation loss in the C-band. *Optics Express* **15,** 14467. ISSN: 1094-4087. http://dx.doi.org/10.1364/OE.15.014467 (2007).

160. Gür, U. M. *et al.* Design and fabrication of ridge waveguide-based nanobeam cavities for on-chip single-photon sources. *Optics Express* **30,** 11973. https://doi.org/10.1364/oe.453164 (Mar. 2022).

161. Van Laere, F. *et al.* Compact Focusing Grating Couplers for Silicon-on-Insulator Integrated Circuits. *IEEE Photonics Technology Letters* **19,** 1919–1921. ISSN: 1041-1135. http://dx.doi.org/10.1109/LPT.2007.908762 (Dec. 2007).

162. Roelkens, G. *et al.* Grating-Based Optical Fiber Interfaces for Silicon-on-Insulator Photonic Integrated Circuits. *IEEE Journal of Selected Topics in Quantum Electronics* **17,** 571–580. ISSN: 1558-4542. http://dx.doi.org/10.1109/JSTQE.2010.2069087 (May 2011).

163. Shor, P. *Algorithms for quantum computation: discrete logarithms and factoring* in *Proceedings 35th Annual Symposium on Foundations of Computer Science* (1994), 124–134.

164. Lo, H.-K., Ma, X. & Chen, K. Decoy State Quantum Key Distribution. *Physical Review Letters* **94.** ISSN: 1079-7114. http://dx.doi.org/10.1103/PhysRevLett.94.230504 (June 2005).

165. Rosenberg, D. *et al.* Long-Distance Decoy-State Quantum Key Distribution in Optical Fiber. *Physical Review Letters* **98.** ISSN: 1079-7114. http://dx.doi.org/10.1103/PhysRevLett.98.010503 (Jan. 2007).

166. Scarani, V. *et al.* The security of practical quantum key distribution. *Reviews of Modern Physics* **81,** 1301–1350. ISSN: 1539-0756. http://dx.doi.org/10.1103/RevModPhys.81.1301 (Sept. 2009).

167. Diamanti, E., Lo, H.-K., Qi, B. & Yuan, Z. Practical challenges in quantum key distribution. *npj Quantum Information* **2.** ISSN: 2056-6387. http://dx.doi.org/10.1038/npjqi.2016.25 (Nov. 2016).

168. Yin, H.-L. *et al.* Measurement-Device-Independent Quantum Key Distribution Over a 404 km Optical Fiber. *Physical Review Letters* **117.** ISSN: 1079-7114. http://dx.doi.org/10.1103/PhysRevLett.117.190501 (Nov. 2016).

169. Lucamarini, M., Yuan, Z. L., Dynes, J. F. & Shields, A. J. Overcoming the rate–distance limit of quantum key distribution without quantum repeaters. *Nature* **557,** 400–403. ISSN: 1476-4687. http://dx.doi.org/10.1038/s41586-018-0066-6 (May 2018).

170. Chen, T.-Y. *et al.* Implementation of a 46-node quantum metropolitan area network. *npj Quantum Information* **7.** ISSN: 2056-6387. http://dx.doi.org/10.1038/s41534-021-00474-3 (Sept. 2021).

171. Aleksic, S. *et al.* Perspectives and limitations of QKD integration in metropolitan area networks. *Optics Express* **23,** 10359. ISSN: 1094-4087. http://dx.doi.org/10.1364/OE.23.010359 (Apr. 2015).

172. Bunandar, D. *et al.* Metropolitan Quantum Key Distribution with Silicon Photonics. *Physical Review X* **8.** ISSN: 2160-3308. http://dx.doi.org/10.1103/PhysRevX.8.021009 (Apr. 2018).

173. Yang, Y.-H. *et al.* All optical metropolitan quantum key distribution network with post-quantum cryptography authentication. *Optics Express* **29,** 25859. ISSN: 1094-4087. http://dx.doi.org/10.1364/OE.432944 (July 2021).

174. Liao, S.-K. *et al.* Satellite-to-ground quantum key distribution. *Nature* **549,** 43–47. ISSN: 1476-4687. http://dx.doi.org/10.1038/nature23655 (Aug. 2017).

175. Boaron, A. *et al.* Secure Quantum Key Distribution over 421 km of Optical Fiber. *Physical Review Letters* **121.** ISSN: 1079-7114. http://dx.doi.org/10.1103/PhysRevLett.121.190502 (Nov. 2018).

176. Kok, P., Williams, C. P. & Dowling, J. P. Construction of a quantum repeater with linear optics. *Physical Review A* **68.** ISSN: 1094-1622. http://dx.doi.org/10.1103/PhysRevA.68.022301 (Aug. 2003).

177. Azuma, K., Tamaki, K. & Lo, H.-K. All-photonic quantum repeaters. *Nature Communications* **6.** ISSN: 2041-1723. http://dx.doi.org/10.1038/ncomms7787 (Apr. 2015).

178. Munro, W. J., Azuma, K., Tamaki, K. & Nemoto, K. Inside Quantum Repeaters. *IEEE Journal of Selected Topics in Quantum Electronics* **21,** 78–90. ISSN: 1558-4542. http://dx.doi.org/10.1109/JSTQE.2015.2392076 (May 2015).

179. Sasaki, M. *et al.* Field test of quantum key distribution in the Tokyo QKD Network. *Optics Express* **19,** 10387. ISSN: 1094-4087. http://dx.doi.org/10.1364/OE.19.010387 (May 2011).

180. Elliott, C. Building the quantum network*. *New Journal of Physics* **4,** 46–46. ISSN: 1367-2630. http://dx.doi.org/10.1088/1367-2630/4/1/346 (July 2002).

181. Mikulicz, M. G. microStabilize: In-plane microstructure stabilization in optical microscopy via normalized correlation coefficient matching method. *SoftwareX* **29,** 102065. ISSN: 2352-7110. http://dx.doi.org/10.1016/j.softx.2025.102065 (Feb. 2025).

182. Bienfang, J. *et al. Single-photon sources and detectors dictionary* http://dx.doi.org/10.6028/NIST.IR.8486 (National Institute of Standards and Technology, Sept. 2023).

183. Foroosh, H., Zerubia, J. & Berthod, M. Extension of phase correlation to subpixel registration. *IEEE Transactions on Image Processing* **11,** 188–200. ISSN: 1057-7149. http://dx.doi.org/10.1109/83.988953 (Mar. 2002).

184. Haisma, J. & Spierings, G. Contact bonding, including direct-bonding in a historical and recent context of materials science and technology, physics and chemistry. *Materials Science and Engineering: R: Reports* **37,** 1–60. ISSN: 0927-796X. http://dx.doi.org/10.1016/S0927-796X(02)00003-7 (Apr. 2002).

185. Moriceau, H. *et al.* Low temperature direct bonding: An attractive technique for heterostructures build-up. *Microelectronics Reliability* **52,** 331–341. ISSN: 0026-2714. http://dx.doi.org/10.1016/j.microrel.2011.08.004 (Feb. 2012).

186. Namatsu, H. Supercritical Drying for Nanostructure Fabrication. *Journal of Photopolymer Science and Technology* **15,** 381–388. ISSN: 1349-6336. http://dx.doi.org/10.2494/photopolymer.15.381 (2002).

187. Hajj-Hassan, M., Cheung, M. & Chodavarapu, V. Ultra-thin porous silicon membranes fabricated using dry etching. *Micro & Nano Letters* **6,** 226. ISSN: 1750-0443. http://dx.doi.org/10.1049/mnl.2010.0233 (2011).

188. Henrie, J., Kellis, S., Schultz, S. M. & Hawkins, A. Electronic color charts for dielectric films on silicon. *Optics Express* **12,** 1464. ISSN: 1094-4087. http://dx.doi.org/10.1364/OPEX.12.001464 (Apr. 2004).

189. Mrowiński, P. *et al.* Optimization of heterogeneously integrated InP-Si on-chip photonic components. *Optics Express* **31,** 1541. ISSN: 1094-4087. http://dx.doi.org/10.1364/OE.474259 (Jan. 2023).

190. Liang, D. & Bowers, J. E. Highly efficient vertical outgassing channels for low-temperature InP-to-silicon direct wafer bonding on the silicon-on-insulator substrate. *Journal of Vacuum Science & Technology B: Microelectronics and Nanometer Structures Processing, Measurement, and Phenomena* **26,** 1560–1568. https://doi.org/10.1116/1.2943667 (July 2008).

191. Plößl, A. & Kräuter, G. Wafer direct bonding: tailoring adhesion between brittle materials. *Materials Science and Engineering: R: Reports* **25,** 1–88. ISSN: 0927-796X. https://www.sciencedirect.com/science/article/pii/S0927796X98000175 (1999).

192. Tong, Q.-Y. & Gösele, U. A Model of Low-Temperature Wafer Bonding And Its Applications. *Journal of The Electrochemical Society* **143,** 1773–1779. https://doi.org/10.1149/1.1836715 (May 1996).

193. Sakanas, A., Semenova, E., Ottaviano, L., Mørk, J. & Yvind, K. Comparison of processing-induced deformations of InP bonded to Si determined by e-beam metrology: Direct vs. adhesive bonding. *Microelectronic Engineering* **214,** 93–99. https://doi.org/10.1016/j.mee.2019.05.001 (June 2019).

194. Holewa, P. *et al.* Optical and electronic properties of low-density InAs/InP quantum-dot-like structures designed for single-photon emitters at telecom wavelengths. *Phys. Rev. B* **101,** 195304. https://link.aps.org/doi/10.1103/PhysRevB.101.195304 (19 May 2020).

195. Zieliński, M. Valence band offset, strain and shape effects on confined states in self-assembled InAs/InP and InAs/GaAs quantum dots. *Journal of Physics: Condensed Matter* **25,** 465301. https://dx.doi.org/10.1088/0953-8984/25/46/465301 (Oct. 2013).

196. Lodahl, P. & Stobbe, S. Solid-state quantum optics with quantum dots in photonic nanostructures. *Nanophotonics* **2,** 39–55. https://doi.org/10.1515/nanoph-2012-0039 (2013).

197. Große, J., Mrowiński, P., Srocka, N. & Reitzenstein, S. Quantum efficiency and oscillator strength of InGaAs quantum dots for single-photon sources emitting in the telecommunication O-band. *Applied Physics Letters* **119,** 061103. ISSN: 0003-6951. https://doi.org/10.1063/5.0059458 (Aug. 2021).

198. Johansen, J. *et al.* Size dependence of the wavefunction of self-assembled InAs quantum dots from time-resolved optical measurements. *Phys. Rev. B* **77,** 073303. https://link.aps.org/doi/10.1103/PhysRevB.77.073303 (7 Feb. 2008).

199. Suffczyński, J. *et al.* Excitation mechanisms of individual *CdTe*/*ZnTe* quantum dots studied by photon correlation spectroscopy. *Phys. Rev. B* **74,** 085319. https://link.aps.org/doi/10.1103/PhysRevB.74.085319 (8 Aug. 2006).

200. Reimer, M. E. *et al.* Overcoming power broadening of the quantum dot emission in a pure wurtzite nanowire. *Phys. Rev. B* **93,** 195316. https://link.aps.org/doi/10.1103/PhysRevB.93.195316 (19 May 2016).

201. Rosa Brouri and Alexios Beveratos and Jean-Philippe Poizat and Philippe Grangier. Photon antibunching in the fluorescence of individual color centers in diamond. *Opt. Lett.* **25,** 1294–1296. https://opg.optica.org/ol/abstract.cfm?URI=ol-25-17-1294 (Sept. 2000).

202. Mikulicz, M. *et al.* Temperature dependence of refractive indices of InP, GaAs, AlAs, and $In_{0.53}Ga_{0.47}As$ in the midinfrared spectral range determined by combined ellipsometry and Fourier-transform spectroscopy. *Phys. Rev. Appl.* **21,** 044001. https://link.aps.org/doi/10.1103/PhysRevApplied.21.044001 (4 Apr. 2024).

203. Winger, M. *et al.* Explanation of Photon Correlations in the Far-Off-Resonance Optical Emission from a Quantum-Dot–Cavity System. *Physical Review Letters* **103.** ISSN: 1079-7114. http://dx.doi.org/10.1103/PhysRevLett.103.207403 (Nov. 2009).

204. Wong, W. H., Pun, E. Y. B. & Chan, K. S. Er3+ – Yb3+ codoped polymeric optical waveguide amplifiers. *Applied Physics Letters* **84,** 176–178. ISSN: 1077-3118. http://dx.doi.org/10.1063/1.1640469 (Jan. 2004).

205. Rakov, N. & Maciel, G. S. Exploring the 4I13/2 → 4I15/2 radiative transition from Er3+ in Y2O3 for temperature sensing. *Journal of Luminescence* **199,** 293–297. ISSN: 0022-2313. http://dx.doi.org/10.1016/j.jlumin.2018.03.020 (July 2018).

206. Phillips, C. L. *et al.* Purcell-enhanced single photons at telecom wavelengths from a quantum dot in a photonic crystal cavity. *Scientific Reports* **14.** ISSN: 2045-2322. http://dx.doi.org/10.1038/s41598-024-55024-6 (Feb. 2024).

207. Miyazawa, T. *et al.* Single-photon emission at 1.5 μm from an InAs/InP quantum dot with highly suppressed multi-photon emission probabilities. *Applied Physics Letters* **109,** 132106. ISSN: 0003-6951. https://doi.org/10.1063/1.4961888 (Sept. 2016).

208. Musiał, A. *et al.* Plug&Play Fiber-Coupled 73 kHz Single-Photon Source Operating in the Telecom O-Band. *Advanced Quantum Technologies* **3.** ISSN: 2511-9044. http://dx.doi.org/10.1002/qute.202000018 (May 2020).

209. Winger, M. *et al.* Explanation of Photon Correlations in the Far-Off-Resonance Optical Emission from a Quantum-Dot-Cavity System. *Phys. Rev. Lett.* **103,** 207403. https://link.aps.org/doi/10.1103/PhysRevLett.103.207403 (20 Nov. 2009).

210. Gao, T. *et al.* A quantum key distribution testbed using a plug&play telecom-wavelength single-photon source. *Applied Physics Reviews* **9.** ISSN: 1931-9401. http://dx.doi.org/10.1063/5.0070966 (Jan. 2022).

211. Gharbia, Y. A., Milton, G. & Katupitiya, J. *The effect of optical fiber endface surface roughness on light coupling* in *Optical Fabrication, Testing, and Metrology* (eds Geyl, R., Rimmer, D. & Wang, L.) (SPIE, Feb. 2004). http://dx.doi.org/10.1117/12.516522.

212. Picelli, L. *et al.* Scalable wafer-to-fiber transfer method for lab-on-fiber sensing. *Applied Physics Letters* **117.** ISSN: 1077-3118. http://dx.doi.org/10.1063/5.0021701 (Oct. 2020).

213. Vaiano, P. *et al.* Lab on Fiber Technology for biological sensing applications. *Laser& Photonics Reviews* **10,** 922–961. ISSN: 1863-8899. http://dx.doi.org/10.1002/lpor.201600111 (Nov. 2016).

214. Jung, I. W., Park, B., Provine, J., Howe, R. T. & Solgaard, O. Highly Sensitive Monolithic Silicon Photonic Crystal Fiber Tip Sensor for Simultaneous Measurement of Refractive Index and Temperature. *Journal of Lightwave Technology* **29,** 1367–1374. ISSN: 1558-2213. http://dx.doi.org/10.1109/JLT.2011.2126018 (May 2011).

215. Park, B. *et al.* Double-Layer Silicon Photonic Crystal Fiber-Tip Temperature Sensors. *IEEE Photonics Technology Letters* **26,** 900–903. ISSN: 1941-0174. http://dx.doi.org/10.1109/LPT.2014.2309345 (May 2014).

216. Smythe, E. J., Dickey, M. D., Bao, J., Whitesides, G. M. & Capasso, F. Optical Antenna Arrays on a Fiber Facet for in Situ Surface-Enhanced Raman Scattering Detection. *Nano Letters* **9,** 1132–1138. ISSN: 1530-6992. http://dx.doi.org/10.1021/nl803668u (Feb. 2009).

217. Roelkens, G. *et al.* Adhesive Bonding of III-V Dies to Processed SOI Using BCB for Photonic Applications. *ECS Transactions* **3,** 321–326. ISSN: 1938-6737. http://dx.doi.org/10.1149/1.2357082 (Oct. 2006).

218. Lu, T.-W., Lin, Y.-C. & Lee, P.-T. Highly Accurate Docking of a Photonic Crystal Nanolaser to a SiNx Waveguide by Transfer Printing. *ACS Photonics* **10,** 2679–2687. ISSN: 2330-4022. http://dx.doi.org/10.1021/acsphotonics.3c00411 (June 2023).

219. Chen, Y. *et al.* Wavelength-tunable entangled photons from silicon-integrated III–V quantum dots. *Nature Communications* **7.** ISSN: 2041-1723. http://dx.doi.org/10.1038/ncomms10387 (Jan. 2016).

220. Chen, C. *et al.* Wavelength-tunable high-fidelity entangled photon sources enabled by dual Stark effects. *Nature Communications* **15.** ISSN: 2041-1723. http://dx.doi.org/10.1038/s41467-024-50062-0 (July 2024).

221. Ollivier, H. *et al.* Three-Dimensional Electrical Control of the Excitonic Fine Structure for a Quantum Dot in a Cavity. *Physical Review Letters* **129.** ISSN: 1079-7114. http://dx.doi.org/10.1103/PhysRevLett.129.057401 (July 2022).

222. Usman, M. Understanding the electric field control of the electronic and optical properties of strongly-coupled multi-layered quantum dot molecules. *Nanoscale* **7,** 16516–16529. ISSN: 2040-3372. http://dx.doi.org/10.1039/C5NR04710B (2015).

223. Gammon, D., Snow, E. S., Shanabrook, B. V., Katzer, D. S. & Park, D. Fine structure splitting in the optical spectra of single GaAs quantum dots. en. *Phys. Rev. Lett.* **76,** 3005–3008 (Apr. 1996).

224. Ghali, M., Ohtani, K., Ohno, Y. & Ohno, H. Generation and control of polarization-entangled photons from GaAs island quantum dots by an electric field. *Nature Communications* **3.** ISSN: 2041-1723. http://dx.doi.org/10.1038/ncomms1657 (Feb. 2012).

225. Zhang, J. *et al.* Micro-transfer printing InP C-band SOAs on advanced silicon photonics platform for lossless MZI switch fabrics and high-speed integrated transmitters. *Optics Express* **31,** 42807. ISSN: 1094-4087. http://dx.doi.org/10.1364/OE.505112 (Dec. 2023).

226. Uzun, A. *et al.* Integration of Edge-Emitting Quantum Dot Lasers with Different Waveguide Platforms using Micro-Transfer Printing. *IEEE Journal of Selected Topics in Quantum Electronics*, 1–11. ISSN: 1558-4542. http://dx.doi.org/10.1109/JSTQE.2023.3243943 (2023).

227. Lee, J., Karnadi, I., Kim, J. T., Lee, Y.-H. & Kim, M.-K. Printed Nanolaser on Silicon. *ACS Photonics* **4,** 2117–2123. ISSN: 2330-4022. http://dx.doi.org/10.1021/acsphotonics.7b00488 (Aug. 2017).

228. Katsumi, R., Ota, Y., Kakuda, M., Iwamoto, S. & Arakawa, Y. Transfer-printed single-photon sources coupled to wire waveguides. *Optica* **5,** 691. ISSN: 2334-2536. http://dx.doi.org/10.1364/OPTICA.5.000691 (May 2018).